THE EFFECTS OF CONFINING PRESSURE AND FLUID SATURATION ON ULTRASONIC VELOCITIES IN ROCKS

by

Karl B. Coyner and C.H. Cheng

Earth Resources Laboratory
Department of Earth, Atmospheric, and Planetary Sciences
Massachusetts Institute of Technology
Cambridge, MA 02139

ABSTRACT

Laboratory measurements of ultrasonic P- and S-wave velocities were made as a function of confining pressure for vacuum dry, benzene-, and water-saturated samples of Westerly granite, Bedford limestone, and Weber, Navajo, Berea, and Kayenta sandstones. The measurements indicate: 1) water-saturated bulk moduli are higher than benzene-saturated values, 2) fluid-saturated shear moduli are always greater than or equal to dry values, and 3) water-saturated shear moduli for the sandstones are higher than benzene values at low pressure while lower than both benzene and dry values at higher pressure, indicating that an apparent water-softening effect is concentrated in the shear modulus. Modelling of the velocity measurements with the Biot (1956a) and Gassmann (1951) equations for static effective bulk modulus indicates that it underestimates the increase in bulk modulus and velocities caused by fluid saturation. Inertial effects of the pore fluid as treated by Biot (1956a, 1956b) are also shown to give minimal improvement to predicted velocities, which are underestimated. Velocity measurements are modelled with the Cheng-Kuster-Toksöz ellipsoidal pore and crack model using the inversion technique developed by Cheng (1978). Fits of dry and benzene-saturated velocities are shown along with pore aspect ratio distributions at zero pressure. Water-saturated velocity data and measured porosity reductions with pressure are compared with predictions of the model.

INTRODUCTION

Compressional and shear wave seismic velocities and attenuations in a rock depend on properties of both the rock and the seismic wave. For the rock these include mineralogy of the solid phase, porosity, and pore fluid type. Particularly important is the distribution of porosity, or pore shapes, as this influences how pressure and fluid saturation affect seismic propagation. Important properties of the seismic wave include its frequency, strain amplitude, and whether it is compressional or shear.

Many details of these factors have been identified and isolated with laboratory measurements. Two valuable techniques include measurements as a function of stress, thereby changing the distribution of pore shapes while keeping mineralogy constant, and as a function of pore fluid saturation, changing overall acoustic response by introducing fluid with readily defined compressibility, viscosity, and density. A number of experimental studies have documented these effects (Hughes

and Cross, 1951; Wyllie et al., 1956, 1958; Birch, 1960, 1961; Simmons, 1964; King, 1966; Nur and Simmons, 1969; Gregory, 1976; Winkler and Nur, 1979; Spencer, 1981; Jones and Nur, 1983; Murphy, 1984). There are several general conclusions from these studies. The effect of confining pressure is to increase velocities, an effect which has been interpreted in terms of the closure of small cracks (Birch, 1960; Simmons, 1964; Nur and Simmons, 1969; Toksöz et al., 1976). In all cases, the introduction of full saturation into dry rocks results in higher P-wave velocities while the S-wave velocities behave less regular. Differences between dry and saturated velocities are more pronounced at lower pressure. Measurements at ultrasonic frequencies which have shown higher S-wave velocities in fluid-saturated rock samples over the corresponding dry samples have been reported by Wyllie et al., 1958; Gregory, 1963; King, 1966; Nur and Simmons, 1969; Murphy, 1984). In addition, Wyllie et al. (1958) and King (1966) have reported on the effects of different types of pore fluids. King (1966) interpreted the results at low pressures as due to "relaxation effects" and also noted several instances where water saturated S-wave velocities were lower than the kerosene saturated velocities, indicating an effect of water on softening the quartz grain contacts.

In this paper we present some new measurements of ultrasonic velocities in a suite of dry and saturated rocks and interpret and model the data with various theoretical models. The experimental data presented in the first part of this paper focuses on the effects of confining pressure and saturation on P- and S-wave ultrasonic velocities for dry, benzene- and water-saturated rock samples. The definition of "dry" is a 20 μm Hg vacuum continuously applied to the sample for at least 24 hours before and as measurements were taken. The definition of "saturated" is benzene at 100 bars introduced through the pore pressure system into the sample under vacuum. Additional measurements with distilled water at 100 bars are also shown for most of the samples. In the second part, the measured seismic velocities are compared with three theoretical models: 1) simplified Biot (1956a) or Gassmann (1951), hereafter referred to as Biot-Gassmann, 2) the high-frequency approximations for inertial effects of the pore fluid as treated by Biot (1956b), and 3) the Cheng-Kuster-Toksöz elliptical pore model.

Benzene in addition to water was chosen as the pore fluid in these measurements in order to compare the effects of water, particularly in the higher porosity rocks at high confining pressures. An example of what happens when water versus benzene is added at these high pressures is shown in Fig. 1. Plotted is a set of stress-strain relations for a vacuum dry, water saturated, and benzene saturated sample of Berea sandstone. The introduction of water into the sample under pressure "softens" the rock so that linear strain increases, owing to fluid interaction with the quartz grains or interstitial cements. Note that the three curves are pretty much parallel after a few hundred bars, so that the nature of porosity at low pressures are at least partially modified in the rock over the whole pressure range. This effect of water on static strain is contrasted with the presence of benzene as the pore fluid, which has little effect on strain except for a slight increase. Wyllie et al. (1958) also report similar effects for a sample of Berea sandstone saturated alternately with dry air, oil, silicone fluid, and water. Maximum strain was measured with water as the pore fluid; minimum strain was measured for the dry sample. Significantly, the silicone measurements were nearly as high as those with water, indicating that perhaps the solubility or wetting properties are not as important as the lubricating properties of the pore fluid. Similar strain measurements of dry and water saturated samples were made by Mann and Fatt (1960) for a number of sandstones. They too observed the large increase of water-saturated strain.

The effect of water is not simply static but is translated into dynamic measurements of velocities also. For many of the samples measurements of dry, benzene and water saturated velocities were made, and comparison of the different saturants will be made. King (1966) also compared dry, kerosene, and water saturations as a function of pressure for a number of sandstones. The most obvious effect of water saturation in his measurements and in the present measurements was to severly reduce saturated S-wave velocities at high pressure. The softening mainly results in a lowering of the dry shear modulus.

LABORATORY APPARATUS AND PROCEDURE

The high pressure experimental apparatus is shown schematically in Fig. 2 and a block diagram of the electronic equipment used to collect the ultrasonic data is shown in Fig. 3. Briefly, the principle features of the apparatus and equipment are: 1) large 7.5 cm diameter by 5 cm long samples are measured, 2) hydrostatic confining pressure and pore fluid pressure or vacuum are independently controlled, 3) the ultrasonic ceramic transducers are isolated from the pressure media, 4) any one of the P and two mutually perpendicular S waves can be selected at any given time for velocity and Q measurement, and 5) the entire experiment is under computer control. The center frequencies of the waveforms are between approximately 500 and 800 kHz depending on the sample and pressures. Temperatures were laboratory ambient, about 18 to 23 °C.

Acoustic measurements were made on cylindrical cores 7.5 cm in diameter by 5 cm long. Samples were located between 2 titanium platens and jacketed with a multiple layered jacket of teflon (for benzene measurements), polyurethane sheet, and air-drying polyurethane liquid (Devcon Flexane). Two ports on each titanium transducer allow for the introduction of pore fluid pressure independent of confining pressure. Hydrostatic confining pressure is applied with kerosene pressurized by an air-driven Haskell pump. Pore fluid pressure is generated via a pressure generator or a positive displacement pump in the case of liquid or straight from a regulated high pressure nitrogen gas cylinder in the tests with nitrogen. Pressures are measured by pressure transducers wired to the HP3497A data acquisition and control unit. Solenoid air valves actuated by the HP3497A unit control air lines to the Haskell pump and to a metering pressure relief valve for the control of confining pressure.

Each titanium endpiece houses a multiply stacked ceramic composite transducer. In each stack are two shear discs oriented 90 degrees to each other along with a compressional disc. The overall pair of titanium endpieces are oriented for the shear wave polarization and the three sets of signals, two shear and one compressional, are sequentially generated and measured at any given time. Approximately 1.8 cm of titanium alloy is between the ceramic transducer and the end of the sample. The face of each titanium endpiece is coupled to the sample ends with a 0.00254 cm thick silver sheet. A steel cap with pressure-excluding electrical feedthroughs seals the ceramic transducer from confining pressure fluid for the titanium endpiece located internally within the pressure vessel. The other titanium endpiece is the end plug for the pressure vessel and consequently the ceramic crystals are located externally. Neither pair of ceramic crystals is therefore subjected to the pressure media. Zero travel time, or time of flight with no sample present, was determined by measuring travel times through aluminum standards of thicknesses 1.27, 2.54, 3.81, 5.08, and 6.35 cm, and extrapolating back to zero thickness. There is a slight dependence of the zero travel time on pressure which was included in the data

reduction. The zero travel time for the P-wave is approximately 7.54 μs, for the first S-wave 13.65 μs, and for the second S-wave 12.45 μs.

The electronics used to generate and receive the acoustic signals are shown in Fig. 3. A Panametrics 5055PR generates the excitation pulse to the source transducer and receives the transmitted wave from the receiver transducer. It amplifies (usually 0 or +10dB) and filters (0.3 MHz high pass) the received signal. Electronic circuits and coaxial switches direct excitation pulses and signals of compressional and both shear waves to appropriate transducers. These circuits are controlled by the HP3497A unit. Output from the Panametrics unit is fed directly into the HP1980B oscilloscope which digitizes the signal at 100 MHz, 10 bits, and sends it to the HP1000 computer for travel time pick, attenuation analysis, and a permanent record. Travel time was determined by a threshold voltage 2.5% of the overall peak-to-peak voltage of the amplified and filtered digitized signal. The picking algorithm resulted in travel-time measurements precise to $\pm$ 15 nanoseconds for both P and S waves. This translates into an overall repeatability of $\pm$0.2% at worst for the calculated velocities. Sample lengths were initially measured and monitored with strain gages. This level of precision was verified by the duplication of measured travel times in repetitive cycles of confining pressure as well as by separate experiments where the same rock sample was removed from the vessel and the jacketing procedure and measurements repeated.

An examples of waveforms collected from a sample of Navajo sandstone at 1000 bars confining pressure and 100 bars benzene pore pressure is shown in Fig. 4. The signals are very clear. The excitation pulse is 180 volts into 50 Ohms, amplification is -10 dB, and there is a 0.3 MHz high pass filter on these signals. The top trace is the P wave, the lower two traces the two S waves. The time offset in the shear wave arrivals is due to transducer design. Note that two shear wave signals allow for direct measurement of shear wave anisotropy in two perpendicular directions in addition to the P wave.

The samples in this study are tabulated in Table 1. The sample suite includes holocrystalline granitic rocks, sandstones, a metamorphic dolomite, and a limestone. Also included in Table 1 are dry bulk densities and porosities for each of the samples calculated from dry and water- or benzene-saturated weighings. Appendix A contains a description of these rocks from hand specimen and thin section analysis. Stress-strain measurements and static moduli calculations for these samples can be found in a previous report or in Coyner (1984).

Samples were extracted from larger blocks using a water-cooled diamond drill and ground with diamond wheel cylindrical and surface grinders to a nominal 7.5 cm diameter and 5 cm length with a parallelism tolerance of 0.0005 cm. During the experiments the end flatness of these large samples was discovered to be very important for coupling. Samples were washed and flushed with water and acetone and then saturated in acetone under a vacuum several times for periods of 24 hours with vacuum drying at 20 μm Hg and 80 °C for periods up to 48 hours. Sample ends were lightly sanded prior to jacketing. A benchtop jig held the sample between the two titanium endpieces for jacketing and orientation of sample directions with shear wave polarizations. Accuracy of shear wave polarization was approximately 0.1 degree.

The sample assembly was located within the pressure vessel, a vacuum was applied to the sample through the pore pressure tubing, and the confining pressure

was initially cycled to the highest pressure expected in the course of the experiment. After initial cycling the confining pressure was held at 20 bars for about 12 hours with constant 20 μm Hg vacuum applied to the pore pressure system and sample before acoustic data was collected. Vacuum dry measurements were made first as a function of confining pressure. After completing the cycle the system was allowed to rest at a pressure of about 10 bars for no less than 12 hours. Confining pressure and then pore pressure were raised to 100 bars pressure and the confining pressure cycled to the highest pressure while pore pressure was maintained at 100 bars.

Benzene-saturated measurements always preceded water-saturated measurements. After the benzene measurements samples were removed from the pressure vessel and thoroughly dried under vacuum at 80 °C. Samples for which measurements with water were carried out were then rejacketed and the entire procedure repeated with water instead of benzene as the pore fluid.

EXPERIMENTAL RESULTS

Figs. 5 through 15 are plots of the vacuum dry (open squares), benzene-saturated (solid squares), and water-saturated (solid squares, as labelled) P- and S-wave velocities versus differential pressure for the rocks listed in Table 1. These include samples of Westerly granite, Bedford limestone, and four sandstones: Weber, Navajo, Berea, and Kayenta. One of the plots, Fig. 8, records the measured anisotropy of S-wave velocities for the sample of Bedford limestone. The saturated data was collected with benzene or water at a constant pore pressure of 100 bars to ensure complete saturation. The difference between confining and pore pressures was taken as the "effective" confining pressure and velocities are reported as a function of this difference. All of the velocities are calculated from data collected as the confining pressure was increased.

For four of the samples which were measured dry, benzene-, and water-saturated, dynamic bulk and shear moduli have been calculated as a function of differential confining pressure. These are plotted in Figs. 16 through 23 for the Bedford limestone, Weber, Berea, and Kayenta sandstones. Isotropy has been assumed in these calculations and the effects of attenuation on making the moduli complex have been ignored. Bulk and shear moduli for each of these samples are shown in successive plots.

The general features to be observed and discussed are the effects of pressure, saturation, and different types of pore fluids. Confining pressure increases both P- and S-wave velocities. This is interpreted to be a result of crack and pore closure. Pressure may completely close a crack or, probably more often the case, simply force rough surfaces into contact. Either process results in a more efficient transmission of stress through the rock and higher velocities. The rate of change in velocity with pressure is more rapid at low pressure as the more compliant cracks close. For most of the rocks the most dramatic increases in velocities have occurred by about 500 bars.

Saturation of rock porosity with liquids may either decrease or increase P- and S-wave velocities depending on the pressure and fluid type. In every instance P-wave velocities increase upon fluid saturation. For the low porosity crack-dominated rocks S-wave velocities also increase, and for the higher porosity sandstones S-

wave velocities increase at low pressures but fall below dry velocities at high pressures.

The pore fluid saturants, benzene and water, show significant differences in their effect on velocities which are not interpretable based on fluid bulk modulus and density alone. The water saturant decreases the overall shear modulus, particularly at high pressures, so that S-wave velocities, in particular, are reduced. In the following paragraphs the effects of saturation, pore fluid type, and confining pressure are discussed for the low porosity granite, the limestone, and the sandstones.

Velocity data for the Westerly granite sample (Fig. 5) can be discussed in terms of saturation, the effect of different pore fluids, and compared with the data of Simmons and Nur (1969). Compared with the other low porosity rocks the effects of saturation and confining pressure are the smallest for this rock. Both P- and S-wave velocities increase upon saturation with benzene and water, S-wave velocities only slightly, P-wave velocities much more. Compared with the data of Nur (1969), the dry velocities are nearly the same. The water saturated P-wave velocities of Nur (1969) at confining pressures below about 500 bars are systematically lower. This may be due to incomplete saturation. As pore pressure was not controlled at a level above atmospheric a slight concentration of undissolved gas in the water would reduce fluid bulk modulus and lead to lower P-wave velocities. Velocities increase with pressure quite dramatically over the first 500 bars as small cracks close with pressure and transmit the acoustic stress wave more efficiently. Upon saturation the relatively incompressible pore fluids greatly diminish the compressibilities of cracks and the bulk modulus increases.

The S-wave velocities for Westerly granite indicate the increase due to saturation and also a possible effect of the water similar to that which will be noted in the sandstones. Nur's (1969) data showed that water saturated S-wave velocities fell below dry at pressures between 100 and 150 bars and systematically stayed there at higher pressures. This observation cannot be explained in terms of fluid bulk modulus or density; the porosity is not high enough for density to decrease velocities, as will be shown in the modelling section with Gassmann's equation. The benzene data in shows that shear modulus and velocities are consistently higher than dry, and comparison of the different data sets for low porosity rocks indicates that the larger the crack porosity, the larger the increase in S-wave velocities above dry. It might also be concluded that the higher the bulk modulus of the saturating fluid, the higher the saturated S-wave velocities should be.

Nur and Simmons (1969) measured dry and water-saturated velocities for Westerly granite. Their major conclusion was that P-velocities increase greatly upon water-saturation because of the large increase in effective bulk modulus with water in the cracks. For shear wave velocities they measured a less regular behavior. Generally for confining pressures less than about 200 bars they found that water saturated S-wave velocities were higher than dry, but that at higher confining pressures saturated velocities fell below their dry measurements. They concluded that saturation had a nil effect on shear modulus. In the present data set clearly and consistently the saturated shear velocities are higher than the dry. Since the density increase for this rock is negligible the saturated shear modulus in addition to the bulk modulus are both higher than in the dry case.

The Bedford limestone velocities (Figs. 6, 7, and 8) are quite unique. In the pressure vessel the sample was never subjected to confining pressures higher than 600 bars in order to minimize the severe matrix damage noted by Johnston (1978) and seen in the data of Nur (1969). The stress-strain relation for this rock is nearly linear and consequently there is little or no natural crack porosity. The effect of benzene and water saturation is to uniformly lower the shear velocities (Fig. 7). In Fig. 17 the shear modulus versus pressure is nearly the same for dry, benzene- and water saturations, and the saturated velocities are therefore predicted on the basis of bulk density alone. In other words, this is the only rock measured where the dry and saturated shear moduli are apparently equal. There must be a few lower aspect ratio pores however, because the P-wave velocities show some pressure dependence and saturated P-velocities are higher then dry, the water saturated values being the highest (Fig. 6). The bulk moduli in Fig. 16 indicate a uniform increase in water-saturated moduli over the benzene-saturated values. A small but consistent anisotropy in the S-wave velocities is recorded in Fig. 8 for dry and benzene saturations. The lower velocities are perpendicular to bedding which is probably a result of ground water dissolution/reprecipitation of the calcite. Nur (1969) measured velocities of Bedford limestone at much higher pressures and over many more cycles, a procedure which introduces irreversible grain crushing and hysteresis in velocities and attenuation (Johnston, 1978). In the present measurements confining pressure was kept low, less than 600 bars, to avoid these effects. Interestingly, the grain crushing in the data of Nur (1969) and Johnston (1978) introduces a population of cracks which are measurable in the dry data but undetectable in the saturated P-wave velocity measurements. The dry P-wave velocity data of Nur (1969) shows tremendous increases with confining pressure, from under 3 km/s at pressures near 0 up to nearly 4.4 km/s at 1 kbar, while the present data shows only slight pressure sensitivity. Saturated velocities, however, are nearly the same in the two sets of data, indicating that the presence of fluid in the pore space essentially removes the effects of the introduced cracks. The same, however, cannot be said for the S-wave velocities because in the data set of Nur (1969) there is the same pressure sensitivity and little difference between dry and saturated values.

The four sandstones, Weber, Navajo, Berea, and Kayenta, in order of increasing porosity, present an interesting spectrum of dry versus saturated velocities which contrast the effects of cracks and pores versus bulk density. Dry, benzene-, and water-saturated velocities are plotted in Figs. 9 through 15 for these four sandstones. Water-saturated data for the Navajo sandstone are not shown. The important points to be made concern the effects of saturation versus the different saturants. To varying degrees the water-saturated velocities, particularly the shear, indicate that water has a softening effect, especially at high pressure, relative to the benzene. This is clearly indicated in the calculated bulk and shear moduli plotted in Figs. 16 through 23. Bulk moduli for the different sandstones are higher for the water saturations because of the higher fluid bulk modulus for water, and the interpretation is consistent for all samples. Shear moduli, on the other hand, indicate that at low pressure water-saturated shear moduli are higher than dry and the benzene-saturated ones. As pressure is increased the water-saturated shear moduli fall below the benzene-saturated shear moduli and then the dry moduli at high pressures. The effect of water is to reduce the shear moduli, particularly at high pressure, in a manner which is not readily explained on the basis of fluid modulus and density. Similar behavior for a number of sandstones can be found in the data of King (1966), who compared dry, kerosene, and water saturated P- and S-wave velocities for a number of sandstones.

For the benzene-saturated S-wave velocities the Navajo, Berea, and Kayenta samples all show a crossing-over of dry and saturated at confining pressures between 200-500 bars. This is interpreted as a transition between crack-dominated velocities at low pressure, where saturated S-wave velocities are higher than dry, to more spherical pore-dominated velocities at higher pressures, where the larger saturated bulk density finally pulls the S-wave velocities below the dry. This same effect is seen in the sandstone data of King (1966) for the dry and kerosene-saturated velocities. When the saturant is water the shear modulus drops and saturated S-wave velocities fall well below the dry and inert fluid-saturated values. Water saturated P-wave velocities for the Weber and Kayenta sandstones show a similar effect of crossing below the benzene saturated values at high pressure. According to the fluid bulk moduli, water being nearly twice that of benzene (Table 2), the water saturated P-wave velocities should always be higher than the benzene saturated velocities in the absence of the small density contrast.

The Weber sandstone benzene saturated S-wave velocities (Fig. 18) are well above dry at all pressures. This is an extremely fine-grained sandstone. The stress-strain relation (Chapter 2) is very non-linear and if a crack porosity is assigned to this rock it would be about 0.5% at zero pressure. The saturated velocities show the largest increase of all sandstones measured. All of these observations point to the fact that this rock has substantial quantities of cracks. If cracks were to be assigned to each grain boundary this rock would probably have the highest concentration of the four sandstones. Weber is also sensitive to water as the pore fluid. Water-saturated S-wave velocities are initially higher than benzene-saturated values at confining pressures less than about 350 bars. At higher pressures the effects of water on the silicate frame shear modulus become important and the velocities drop below the dry measurements above 700 bars differential pressure. The P-wave velocities are not as sensitive, and at pressures above 600 bars the water-saturated measurements fall below the benzene-saturated values.

The Navajo sandstone has the highest velocities of the four sandstones and the least dependence on pressure (Fig. 11). This rock also has the stiffest stress-strain relation and lowest crack porosity ($\approx$0.08%). This is an extremely well-silicified rock and is from the White member of the Navajo formation as contrasted with the Red member, which was studied by Johnston (1978). In comparison, the P- and S-wave velocities in the present data set are both higher. The water-saturated S-wave velocities of Johnston (1978) are lower than dry at all pressures while in the present data set the benzene-saturated velocities are higher below about 500 bars and lower at higher pressures. Presumably, water-saturated velocities for the particular sample studied here would be lower than those with benzene at the higher pressures.

The Berea sandstone velocity data (Figs. 12 and 13) and Kayenta sandstone data (Figs. 14 and 15) show similar pressure and saturation dependence with the Kayenta sample having slightly lower velocities and more sensitivity to the water saturant. Both rocks, and particularly the Kayenta, show a very rapid falloff in velocities below about 200 bars. The Kayenta sandstone is a very friable rock, coarser grained than the Berea, higher in porosity, and not as well cemented. Therefore to minimize cracks induced by the cycling of pressure the Kayenta sample was not subjected to pressures above 700 bars.

King (1966) and Johnston (1978) both measured velocities in samples of Berea sandstone. King's data included the dry, kerosene-, and water-saturated conditions

for a sample of Berea with somewhat higher porosity, 20.5%, and lower density, 2.14 g/cc, as contrasted with the 17.8% porosity and 2.194 g/cc density measured for the sample used in this study. The reported porosity for the sample studied by Johnston (1978) is approximately 16%. All of the dry data sets agree to within 5-10%, with Johnston's data slightly faster, particularly at low confining pressures. King's data for kerosene-saturated Berea agrees quite well with the present benzene-saturated data. Benzene-saturated P-wave velocities are higher than dry and S-wave velocities are higher than dry at low pressures (less than 300 bars for King's data; 250 bars for the present data), crossing over to being lower at higher pressures. The water-saturated P-wave velocities also agree, with the values only slightly dropping below the benzene or kerosene values at the highest pressures (700 bars for King's data; 1000 bars for the present data). In the water-saturated S-wave velocity data of both King and Johnston, however, the values are well below the dry and kerosene-saturated values. In the present data set, at pressures below about 250 bars, the water-saturated velocities are higher than both the dry and benzene-saturated values; above 250 bars the water-saturated values fall below the benzene values. Part of this may be due to cycling. In the present data set the procedure did not include any cycles of confining pressure after the water was introduced. There is a tendency for velocities, particularly shear, to drop with successive cycles when water is the pore fluid.

The Kayenta sandstone velocity measurements with water as a pore fluid show a fair degree of sensitivity relative to the benzene measurements. At pressures below about 75 bars the water-saturated S-wave velocities are higher than those with benzene. Above that pressure the water-saturated measurements do not increase as fast as either the benzene or dry measurements, and above 150 bars fall well below the dry and benzene-saturated measurements. For the P-wave velocities water-saturated values fall below the benzene values above 200 bars and almost drop to the dry measurements at the maximum differential pressure of 700 bars.

In the following sections various models of acoustic propagation are examined. The emphasis is on the effect of fluid saturation and, particularly, the observed increases of S-wave velocities. The benzene measurements are emphasized in the modelling procedures because of the apparent difficulties in rationalizing water saturated measurements on the basis of only fluid bulk modulus and density properties.

BIOT-GASSMANN EQUATION

The Biot-Gassmann equation is a static calculation of the effective bulk modulus for a fluid-saturated porous solid considered as a closed system. The volumetric stress-strain response of a sample element is calculated with the condition that no fluid mass is allowed to cross the sample boundary as it is strained by a uniform external stress. For a compressive stress the pore pressure builds up and the response is stiffer than if the system were open and pore fluid were allowed to freely flow out of the strained, interconnected pore volume. The stress-strain behavior for the closed system may be associated with the "undrained" condition in reference to soil mechanics. Calculation of the undrained bulk modulus proceeds directly from the consolidation equations of Biot (1941), and Biot called the modulus the "instantaneous compressibility". The contribution of Gassmann (1951) was to specialize the linear static description to the case of a fully homogeneous and isotropic porous solid, consider the open and closed system response, and to apply

the result to acoustic wave propagation. With the assumption of complete homogeneity and isotropy of the solid matrix in addition to the overall porous medium the Biot material parameters can be replaced with the following four: the intrinsic bulk modulus K_s of the matrix, the overall frame bulk modulus K, the fluid bulk modulus K_f of the fluid filling the pores, and the porosity φ. Pore pressure causes no bulk shear in linear elasticity and therefore the shear modulus is unaffected by whether the system is open or closed. Consequently the dry and saturated shear moduli are equal. Pore pressure is assumed to equilibrate throughout the interconnected porosity.

The constitutive equations for a linear, isotropic, and homogeneous fluid-saturated porous solid are

$$\sigma_{ij} = (K - \frac{2}{3}G)\delta_{ij}\varepsilon_{kk} + 2G\varepsilon_{ij} - \zeta p\,\delta_{ij}, \tag{1}$$

$$\zeta = 1 - \frac{K}{K_s}, \tag{2}$$

$$\Delta m_f = \rho_f \frac{v_f}{K_f} p + \rho_f \left(\frac{1}{K} - \frac{1}{K_s}\right)\left(\frac{\sigma_{kk}}{3} + p\right) - \rho_f \frac{v_f}{K_s} p. \tag{3}$$

where σ_{ij} is stress, p pore pressure, G shear modulus, ε_{kk} volumetric strain, ε_{ij} strain, m_f fluid mass, ρ_f pore fluid density, v_f pore fluid volume, and the other constants are as described in the previous paragraph. For the calculation of undrained bulk modulus Δm_f=0 and Eq. 3 gives a relation between hydrostatic confining stress and pore pressure. Pore fluid volume is associated with porosity and fluid density drops out. This relation is substituted into the first equation for pore fluid pressure. Stress is assumed hydrostatic so the shear modulus and shear strains drop out. The result is an expression relating hydrostatic stress and volumetric strain. The modulus in this relation is the undrained or effective bulk modulus K^* which, after algebraic manipulation, is related to the three bulk moduli and porosity in the expression

$$K^* = K + \frac{(K_s - K)^2}{K_s - K + \varphi(K_s / K_f)(K_s - K_f)} \tag{4}$$

This is the Gassmann equation for effective static bulk modulus of a sealed porous solid. A refinement by Brown and Korringa (1975) removed the requirement for microhomogeneity and microisotropy by defining an additional modulus, but the above expression is used in the absence of experimental evidence indicating that this additional modulus differs from K_s.

The shear modulus is unaffected by the pore fluid so the effective shear modulus G^* for the closed system is unchanged from the open system and

$$G^* = G \tag{5}$$

The application of these static results to dynamic acoustic velocities comes from the identification of the effective bulk and shear moduli with the moduli in the solutions to the wave equation for plane waves in a linear isotropic media. For P- and S-wave velocities these are

$$V_p = \left(\frac{K^* + \frac{4}{3}G^*}{\rho} \right)^{\frac{1}{2}} \tag{6}$$

$$V_s = \left(\frac{G^*}{\rho} \right)^{\frac{1}{2}} \tag{7}$$

where ρ is bulk density. From dry velocities and measured density the "drained" bulk modulus K and shear modulus G are calculated. Although the model is based on a static calculation the static moduli cannot be used because of the larger dynamic versus static moduli found for rocks with cracks (Zisman, 1933; Simmons and Brace, 1965; Cheng and Johnston, 1981). In the present context the Gassmann equation is limited simply to predicting saturated velocities from dry by calculating the effective bulk moduli together with a new bulk density computed from porosity and fluid density. Computation of the effective bulk modulus K^* requires the fluid bulk modulus K_f, the measured porosity φ, and the intrinsic bulk modulus K_s. The intrinsic bulk modulus can be estimated from mineralogy or else measured in an unjacketed stress-strain test.

Benzene- and water-saturated P- and S-wave velocities have been predicted with Gassmann's equation from the dry velocities for the data on samples of Westerly granite, Navajo, Berea, and Kayenta sandstones, and Bedford limestone. The intrinsic bulk moduli K_s, densities, and initial porosities are compiled in Table 1. In addition, the changes in porosity and density with confining pressure were accounted for in the present calculations from strain measurements. Pore fluid properties of the benzene and water are given in Table 2.

The results are shown in Figs. 24 through 33. Each figure is either the P- or S-wave dry and benzene- or water-saturated (solid squares) velocities versus confining pressure. For the plots with P-wave velocities the dashed line is the predicted saturated P-wave velocity from the dry velocity moduli using Gassmann's equation for the effective bulk modulus, the dry shear modulus, and the saturated density computed from dry density and fluid density. Two separate plots of predicted and measured P-wave velocities have been prepared for water- and benzene-saturated velocities of the Berea and Kayenta sandstones. In addition, in the plots for these two sandstones the P-wave velocities predicted from the dry shear moduli (curve A) are distinguished from those predicted from the saturated shear moduli (curve B). For the plots with S-wave velocities the dashed line is the predicted saturated velocity from the dry shear modulus and the saturated density. In the following paragraphs this data is discussed and references to the Gassmann equation predictions are intended to apply to both saturated P- and S- wave velocities

although in a strict sense the Gassmann equation is only the calculation of the closed system effective bulk modulus.

In Figs. 24 and 25 the P- and S-wave velocities for Westerly granite are shown. Since bulk density increases almost negligibly upon saturation in these low porosity (≈1%) rocks the predicted saturated shear velocity is nearly unchanged from the dry case. As shown in Fig. 25 the saturated S-wave velocities are higher than the dry for Westerly granite, and this is the case for all of the low porosity rocks. The saturated shear modulus is consistently larger than the dry for all of the low porosity rocks. Therefore the predicted benzene-saturated S-wave velocity for Westerly granite is severely underestimated.

In Fig. 24 the P-wave velocities for Westerly granite show that the predicted saturated velocities make up little more than half of the difference between measured dry and saturated velocities. If instead of the dry shear modulus the saturated shear modulus is used in predicting P-wave velocity the dashed line moves up, but not substantially.

In Figs. 26 through 35 are shown the P- and S-wave velocities for Navajo, Berea, Kayenta, and Weber sandstones with the dashed Gassmann equation predictions. For these sandstones, with porosities ranging from 9.6-22.3%, the saturated densities become important in the predicted velocities. Since at low pressure for all three sandstones the saturated shear velocities as measured are higher than dry the prediction based on saturated density is in the wrong direction. At high pressure, when the effects of cracks are reduced, the predicted and measured saturated velocities are lower than dry and tend to converge. At 1 kbar pressure the Berea predicted S-wave velocity is the nearest to the measured although still slightly lower.

The water- and benzene-saturated P-wave velocities predicted for the 4 sandstones always underestimate those which are measured. In Fig. 26 are shown the dry and benzene-saturated P-wave velocities for Navajo sandstone. The lowest dashed curve is the predicted velocities based on an intrinsic bulk modulus K_s of 0.36 Mb, which was measured in the unjacketed stress-strain experiment in Coyner (1984). Predicted P-wave velocities are much lower than those measured, and at high pressures the saturated bulk density actually pulls the predicted velocities below the measured dry ones. The two other curves are for higher intrinsic bulk moduli, 0.5 and 0.6 Mb, and are included here to indicate the sensitivity of the Gassmann prediction to the value used for K_s. There may be some confusion between static and dynamic moduli and and what value to use for K_s. For single crystals, or materials without cracks, such as metals, static and dynamic moduli are essentially equivalent relative to rocks. In the Gassmann equation it is the intrinsic crack-free bulk modulus which is desired, and that measured in the unjacketed stress-strain test is just that. For Navajo sandstone the measured K_s is 0.36 Mb, slightly lower than pure quartz because of the extensive secondary silica cementation, and this is also what the dynamic value should be.

In Fig. 28 the dry and benzene-saturated saturated P-wave velocities and predictions are plotted for Berea sandstone. An equivalent plot for water-saturated velocities is Fig. 29. In these plots there are two dashed curves representing different possibilities for applying Gassmann's equation to predict the saturated velocities. Curve A uses the dry bulk and shear moduli. For the benzene-saturated velocities curve A is far below those measured. For the water-saturated velocities it

does better, and at high pressure actually reaches the measurements, but this is probably because the P-wave velocities with water are lower than expected because of the effect of water on lowering the shear modulus. Curve B uses the dry bulk moduli but the saturated shear moduli. This modified application of Gassmann's equation simply accepts the fact that saturated shear moduli are much higher than dry and will be used in predicting the P-wave velocities. Curve B does somewhat better at predicting saturated velocities, particularly those with water, but still underestimates the measured values.

In Figs. 31 through 33 are equivalent plots for the Kayenta sandstone, and in Figs. 34 and 35 are equivalent plots for the Weber sandstone. As can be seen in all of these plots the Gassmann equation predicts velocities which are consistently low. Using the saturated shear moduli improves the predicted P-wave velocities, particularly for the Weber sandstone, but there are still large underestimations. For the water-saturated Kayenta sandstone (Fig. 32) and Weber sandstone (Fig. 35), as was the case for Berea sandstone (Fig. 29), the B curves tend to fall below the A curves at high pressure. This is because the water saturated shear moduli are lower than the benzene saturated ones.

The only success of Gassmann's equation in predicting saturated velocities is for the S-wave velocities of Bedford limestone as shown in Fig. 37. Really this is only the prediction of saturated shear velocity on the basis of increased saturated density. The Gassmann equation for effective bulk modulus and hence saturated P-wave velocity underestimates the measured difference by more than half as shown in Fig. 36. Accurate prediction of saturated shear velocity for the Bedford limestone is actually a significant result as will be discussed in the next section on Biot inertial effects.

In conclusion, however, the Gassmann equation for effective saturated bulk modulus and the equating of dry and saturated shear modulus severely underestimates the effect of saturation. Saturated P- and S-wave velocities predicted from dry are consequently lower than measured in all rocks studied except for S-wave velocity in the Bedford limestone.

BIOT INERTIAL EFFECTS

One objection to the Gassmann equation for calculating saturated velocities with static deformation relations is the neglect of pore fluid inertia. Since the pore fluid mass in higher porosity materials may be appreciable, and since the pore fluid is a viscous phase in a permeable medium, dynamic oscillation of the bulk material may cause inertial forces within the pore fluid to phase lag overall stress. The earlier work of Biot (1956a,b) on acoustic wave propagation is a formulation of the static consolidation equations for dynamic oscillation with the inclusion of inertial terms. The displacements of bulk frame and pore fluid relative to the bulk frame are separately described by dynamic equations. Application is limited to solids of uniform porosity, and interaction of stress waves with what Biot (1962) would come to call "hidden coordinates", such as cracks, is neglected.

As a function of frequency the treatment contrasts viscosity of the fluid phase versus inertia of the fluid phase. At low frequency (1956a) the viscosity of the pore fluid maintains Poiseulle flow in response to pressure gradients due to stress waves. At high frequency (1956b) the inertia of pore fluid exceeds consideration of fluid

viscosity and viscous shear across a narrow zone at the pore space boundary decouples pore fluid mass from the bulk frame. The two frequency ranges are separated by a critical frequency. The breakdown of Poiseuille flow above the critical frequency is determined by friction at pore boundaries and so pore shape is a factor in addition to fluid viscosity, density, and frequency. For the present measurements of ultrasonic velocities centered around 1 MHz the range of application is the high frequency analysis. This maximizes the effect of pore fluid inertia on velocities.

Above the critical frequency but below the frequency at which scattering becomes important the solutions to the dynamic equations for group velocities are

$$V_s = \left[\frac{G}{(1-\varphi)\rho_s + \varphi\rho_f - (1/\alpha)\varphi\rho_f}\right]^{\frac{1}{2}}, \tag{8}$$

$$V_p = \left\{\frac{P\rho_{22}+R\rho_{11}-2Q\rho_{12}+\left[(P\rho_{22}+R\rho_{11}-2Q\rho_{12})^2-4(\rho_{11}\rho_{22}-\rho_{12}^2)(PR-Q^2)\right]^{\frac{1}{2}}}{2(\rho_{11}\rho_{22}-\rho_{12}^2)}\right\}^{\frac{1}{2}}, \tag{9}$$

where

$$P=\frac{(1-\varphi)(1-\varphi-K/K_s)K_s+\varphi K_s K/K_f}{1-\varphi-(K/K_s)+\varphi(K_s/K_f)}+\frac{4}{3}G, \tag{10a}$$

$$Q=\frac{(1-\varphi-K/K_s)\varphi K_s}{1-\varphi-(K/K_s)+\varphi(K_s/K_f)}, \tag{10b}$$

$$R=\frac{\varphi^2 K_s}{1-\varphi-(K/K_s)+\varphi(K_s/K_f)}. \tag{10c}$$

The symbols for the moduli are as previously defined and the bulk modulus K and shear modulus G are for the drained or dry porous solid. The density terms ρ_{11}, ρ_{12}, and ρ_{22} are defined as

$$\rho_{11}+\rho_{12}=(1-\varphi)\rho_s \tag{11a}$$

$$\rho_{22}+\rho_{12}=\varphi\rho_f \tag{11b}$$

$$\rho_{12}=(1-\alpha)\varphi\rho_f. \tag{11c}$$

The density of the solid matrix is ρ_s and that of the fluid ρ_f. The density or mass coefficient ρ_{12} measures the inertial coupling or force on the pore fluid as the solid

frame is accelerated. A nondimensional coefficient α of value greater than 1 represents an average geometry of the pore space as it affects inertial coupling. If $\alpha=\infty$, such as for a very tortuous and narrow pore geometry, the solid and fluid mover together and the equations for velocities reduce to Gassmann's equations. This is most clearly evident in the expression for shear velocity as the first two terms in the denominator are saturated bulk density. As coupling decreases the effect of pore fluid mass on bulk density is reduced and wave velocities increase.

Application of the inertial effects to the present measurements is best seen in the expression for shear velocity and by consideration of the requirement for uniform porosity. Shear modulus is unaffected by the presence of pore fluid. Apparent mass of the porous solid is reduced by pore fluid inertia as the surrounding frame oscillates and is determined by the geometrical factor α. If coupling is negligible, such that $\alpha\approx1$, the density term in the denominator is the bulk density of the saturated and drained or dry porous solid. The shear velocity in this case is the drained or dry shear velocity. At best the inertial effect can raise the saturated shear velocity up to the dry velocity, but not above.

Clearly the consideration of pore fluid inertia in the low porosity rocks (granitic rocks) has a negligible effect on velocity. Aside from the small fluid mass in the saturated condition, these rocks fail the requirement for uniform porosity. Since at all pressures the saturated shear velocities are higher than dry the fluid inertia is not determining the difference between dry and saturated velocities.

A significant indication of whether pore fluid inertia is important in the higher porosity rocks is given by the shear wave velocities for Bedford limestone (φ = 11.9 %). As shown in the previous section the uniformly lower saturated shear wave velocities for this rock are accurately predicted from the increase in bulk density. Of the rocks studied Bedford limestone is unique because it is a nearly perfect linear elastic solid as indicated by the nearly linear stress-strain relation. The interpretation is that this rock has little or no crack porosity and that the dry and saturated shear moduli are almost equal. In terms of the ellipsoidal crack models to be discussed in later sections the porosity of Bedford limestone is modelled as nearly spherical. The geometrical coupling value of α is 3 and quite likely is somewhat larger. The strong indication in the S-wave velocity data is that inertial effects are small and that the pore fluid and matrix oscillate in phase.

For the sandstones a comparison of dry and saturated velocities at high pressure ($\approx$ 1 kbar) is a reasonable method for estimating the importance for saturated velocities. This procedure predicts a minimum value of α. The assumption is that at high pressure the contribution of cracks and narrow pore spaces to increasing saturated velocities are negated. Since porosity does not decrease substantially with pressure the inertial effects over the entire pressure range may be estimated. This also assumes that those pore features which change with pressure do not affect the α parameter. At high pressures three of the four sandstones (Berea, Navajo, and Kayenta) have saturated S-wave velocities which drop below the dry velocities. For the Weber sandstone this does not occur and the following technique does not apply. When saturated and dry shear velocities are increasing uniformly and by a small amount at high pressure the implication of assuming minimal crack effects means the difference represents the effect of density only. To the extent that measured S-velocities fall above those predicted by saturated bulk density (Gassmann's equation) is an indication of inertial effects. The geometrical parameter α is adjusted in the expression for saturated S-wave velocity (Eq. 8) to

agree with measured velocities at high pressure.

Berea sandstone saturated velocities can be used to evaluate inertial coupling and the geometrical parameter α. In Fig. 38 the vacuum-dry and benzene-saturated S-wave velocities are plotted from 0 to 1 kbar differential confining pressure. The dashed line is the Gassmann prediction if the saturated shear modulus were the same as dry and if coupling of fluid to solid matrix were perfect ($\alpha=\infty$). If at high confining pressures (700 - 1000 bars) the difference between the dashed line and measured saturated S-wave velocities is interpreted to represent inertial coupling the parameter α is calculated to be about 4.4 from the shear velocity expression. This is an absolute minimum because the measured and predicted S-wave velocities tend to converge at higher pressures.

In Figs. 38 and 39 are plotted the predicted saturated P- and S-wave velocities for Berea sandstone with a coupling factor of 4.4. The predicted and measured S-wave velocities at the highest pressures are essentially pinned together and the effects propagated over the whole pressure range for P- and S-waves. Johnston (1978) did the same thing in evaluating the contribution of inertial effects to the attenuation. The results are not striking in terms of predicting saturated P- and S-wave velocities. Obviously the higher saturated S-wave velocities at low pressures are not predicted. The only benefit to the predicted P-wave velocities is to at least raise them slightly above the dry velocities at high pressure.

Similarly, in Figs. 40 and 41 the predicted velocities for Navajo sandstone are plotted based on a coupling of α = 2.1. Because this α is smaller the effects on predicted velocities are more substantial over the Gassmann predictions relative to the Berea sandstone. Even when the inertial effects are overestimated, as is probably the case here, the only benefit for the predicted P-wave velocities is to raise them almost to the measured dry velocities at high pressure.

The conclusion is that inertial effects of the pore fluid on velocities are probably quite small based on the Biot analysis. The coupling parameters calculated for Berea and Navajo sandstones are absolute minimums. Saturated S-wave velocities for the Bedford limestone indicate that inertial effects are perhaps almost nonexistent in these measurements. Gassmann's equations do not underestimate saturated ultrasonic velocities because of inertial effects.

CHENG-KUSTER-TOKSOZ MODEL AND INVERSION

The final model to be examined in light of the experimental velocity data is the Cheng-Kuster-Toksöz crack and pore model. The dry and saturated velocity data and porosity data can be inverted using a technique developed by Cheng (1978). Here we look at the results of inversion of the dry and benzene-saturated velocities for pore spectra. Interesting checks or tests of the inversion results are enabled by using the water-saturated velocities in addition to the experimentally measured porosities as a function of confining pressure. Data for three of the sandstones, the Weber, Berea, and Kayenta, are used to cover a wide range of porosity. Data from the Bedford limestone are examined and compared with previous results. Westerly granite data is examined and contrasted with the sedimentary rocks.

Kuster and Toksöz (1974) obtained formula for the dynamic effective moduli of a two-phase medium with ellipsoidal inclusions by evaluating the scattered

displacements of long wavelength plane waves from single inclusions embedded in an infinite matrix. Concentration, shapes (aspect ratio of the ellipsoids), and properties of the inclusions (bulk modulus, shear modulus, density) determine the displacements and summation over all inclusions leads to a description of effective moduli for the bulk material. The experimental dry and saturated P- and S-wave are consistent with several aspects of this model, first and foremost with regards to the larger saturated shear moduli in the low porosity rocks. Secondly, since the model allows for a spectrum of pore shapes from very thin cracks up to spherical pores, the measured velocities of higher porosity rocks can be interpreted. Thirdly, the increases in the velocities with pressure can be explained in terms of successive closing of small aspect ratio cracks. At higher pressures, the population of these small aspect ratio cracks are reduced and the increases in the velocities with pressure diminishes.

A quite useful demonstration of the effects pore shape and fluid saturation have on measured velocities as predicted by this model was given by a calculation of an idealized porous solid in Toksöz et al. (1976) and reproduced in Fig. 40. This plot is of P- and S-wave velocities normalized to the velocity of the solid matrix as a function of porosity. For various singular sets of aspect ratios the theoretically derived effective moduli can be used to calculate velocities at different concentrations, which can be equated with porosity. There are three main observations to be made from this plot, all of which correlate with various observations in the measured velocities which will follow. First, lower aspect ratio pores or cracks have a greater influence in decreasing velocities than the more spherical pores. Secondly, saturating fluids affect P-wave velocities more than the S-wave velocities relative to dry because of the higher sensitivity of bulk modulus to saturation. Third, saturation has the greatest effect on the lower aspect ratio pores, increasing both velocities except for the more spherical pores.

What has been lacking for this model is clear experimental data supporting the predicted effect of saturation on S-wave velocities. The present data tends to resolve this need. For example, consider the velocities for the Westerly granite (Fig. 4). According to Walsh (1965) if the compliant porosity in these rocks is modelled as penny-shaped cracks the closure pressure is approximately αE_0, where α is aspect ratio and E_0 the Young's modulus of the solid. As a rule of thumb for silicate rocks this means that at 1 kbar confining pressure cracks of aspect ratio 0.001 are closing. For most of the rocks measured in this study the differences between dry and saturated velocities are substantially reduced by 1 kbar, and the conclusion therefore is that cracks of this aspect ratio or lower are dominating the observed pressure and saturation dependence. In Fig. 40 the model predicts that for aspect ratios of 0.1 and less the saturated S-wave velocities should be higher than dry. All of the saturated S-wave velocities in the low porosity rocks are higher than dry, and the difference between dry and saturated is greater at low pressure where the lower aspect ratio pores are present.

For the three sandstones studied the surprising result is the extent to which fine cracks dominate the velocities at low pressure as indicated by the higher saturated S-wave velocities. The increase in shear modulus more than cancels out the increase in density upon saturation. The comparison of dry and saturated velocities in these rocks is, as was pointed out in the introduction, benefited greatly by the use of benzene as a pore fluid. In the modelling of sandstone data by Cheng (1978) the saturated matrix shear modulus invariably had to be lowered to fit both the saturated P- and S-wave velocities in the sandstones studied. The explanation

that matrix clays are softening with the introduction of water is not entirely correct because quartz or amorphous silica will become more deformable with water. The challenge with this present data set is to model the benzene-saturated velocities for these higher porosity rocks with ellipsoidal shapes such that the saturated matrix shear modulus does not have to be changed from the dry. In addition, the unjacketed strain measurements from Coyner (1984) provide the intrinsic matrix bulk modulus so that it does not have to be estimated from mineral averages or else from high pressure jacketed strain measurements.

In this section we take the dry and benzene saturated P- and S-wave velocity data and invert them using the technique of Cheng and Toksöz (1979) to obtain the pore-aspect ratio spectra of the rocks. The rocks studied are Westerly granite, Bedford limestone and Weber, Berea and Kayenta sandstones. We have also incorporated the static bulk moduli measured on the same rock samples into the calculation of the rate of closing of small aspect ratio cracks. Since the process of pressure application in the laboratory is essentially a static one, we feel that the use of the static moduli is more justified than the dynamic moduli obtained from velocity measurements.

The pore-aspect ratio spectra obtained from the inversion are checked three ways. First, the predicted and observed dry and benzene saturated velocities are compared. Then the pore-aspect ratio spectra are used to predict the water saturated P- and S-wave velocities and the results are compared with laboratory measured velocities. Since the water saturated velocities were not used in the inversion for the pore-aspect ratio spectra, this step acts as an independent check of the ability of the model to predict velocities of porous rocks. Finally, the changes in porosities as a function of pressure calculated form the pore-aspect ratio spectra are compared to the porosity changes derived from static strain measurements.

In Figures 41-43 we have plotted the results for the Westerly granite. Since the model of Cheng-Kuster-Toksöz is based on the assumption of small concentrations of ellipsoidal or penny-shaped cracks, one would expect that the model should fit the Westerly granite data reasonably well. In Figure 41, we can see that the fits to the dry and benzene saturated P- and S-wave velocity data are very good. There is very little difference between the predicted and measured velocities except for slight discrepancies in the dry P-wave velocities. In Figure 42 is the resulting pore-aspect ratio spectrum at zero pressure. As we can see, there is a large fraction of crack porosity compared to the equidimensional (aspect ratio = 1) pores. Figure 43 shows that predicted versus measured changes in porosity as a function of pressure. As may be expected from the velocity fits, there is no difference between the two. This is a good test of applicability of the model.

In Figures 44 to 55 we showed the results for the three sandstones: Weber, Berea and Kayenta. These sandstones are arranged in increasing order of porosity. For the Weber sandstone, the fits to the velocity-pressure data (Figure 44) are very good, especially the higher benzene-saturated S-wave velocities. The model slightly overestimates the P-wave velocities at low pressures. This is partly an artifact of the inversion algorithm which puts more weight on the fit to the shear moduli than the bulk moduli. The justification for that is that the bulk moduli are derived from the P- and S-wave velocities together, and hence contains more error than the shear moduli, which are derived from just the S-wave velocities. The pore-aspect ratio spectrum shows a much larger concentration of small aspect ratio cracks than the Westerly granite, up to an aspect ratio of 0.001. As expected, most of the porosity is

concentrated in the spherical and near spherical (aspect ratio 1 and 0.1) pores. The model predicts a slightly smaller decrease in porosity with pressure (Figure 46) than observed. This is perhaps a result of underestimating the crack porosity. If this is true, it can also explain the overestimate of the P-wave velocities at low pressures. The predicted water saturated velocities agree quite well with the measured velocities (Figure 47). In general, for the Weber sandstone, the model fits all the observations quite well.

For the higher porosity sandstones, the Berea and and Kayenta, the model does not do as good a job in fitting the data. For the Berea sandstone (Figures 48) the model overestimates the benzene saturated P-wave velocities at low pressures. The pore-aspect ratio spectrum (Figure 49) shows a lower concentration of smaller aspect ratio cracks than the Weber sandstone. The predicted porosity decrease with pressure (Figure 50) is a little lower than the measured decrease. The predicted water saturated P- and S-wave velocities (Figure 51) are higher than the data. This last point is significant in terms of the proposed water weakening of the silicates in the matrix. In contrast to Cheng (1978), the predicted water saturated velocities are calculated using the same matrix moduli as for the dry and benzene saturated cases. Thus the overestimate of the velocities by the model is consistent with the hypothesis of the water softening of the silicate matrix.

For the Kayenta sandstone the fit to the dry and benzene saturated velocities (Figure 52) are reasonable, although once again the model fit the dry velocities better than the benzene saturated ones. The pore-aspect ratio spectrum (Figure 53) shows a larger concentration of small aspect ratio cracks than the Berea sandstone. This is reflected in the large decrease in porosity with pressure predicted by the model (Figure 54). However, the observed porosity change do not show nearly as much decrease with pressure. Looking back at the velocity data, we can see that the large porosity change predicted by the model is the result of the large changes in velocity with pressure, especially below 250 bars. The inconsistency between the porosity change and the velocity data may be due to anisotropy in the sample and will have to be investigated further. The predicted water saturated velocities (Figure 55) are once again higher than the measured velocities. As in the Berea sandstone, this may be attributed to the water-softening of the matrix.

For the Bedford limestone there is very little change of velocities with pressure. The fit to the dry and benzene saturated velocities (Figure 56) are in general very good, especially for the S-wave velocities. However, the observed P-wave velocities at low pressures are significantly lower than the predicted velocities. The pore-aspect ratio spectrum obtained from the velocity inversion (Figure 57) shows very little small aspect ratio cracks, as expected. Almost all the porosity is concentrated in the spherical and near spherical pores. The predicted porosity change with pressure (Figure 58) shows a small decrease with pressure and is in excellent agreement with data. The predicted water-saturated P-wave velocities are higher than the measured velocities, while the predicted and measured S-wave velocities agree very well (Figure 59).

We should point out that in the inversion, we started with the "intrinsic" matrix bulk modulus from unjacketed strain measurements as our matrix bulk modulus. For the matrix shear modulus we started with a value which would give a Poisson's ratio similar to that of the dominant mineral in the matrix. We then systematically varied the matrix moduli in the inversion until we minimized the variance between the predicted and observed velocities. Thus the matrix moduli actually used in the

inversion are slightly different from the "intrinsic" moduli measured from unjacketed strain data. The moduli used in the inversion are usually lower, by 5 to 10 percent, than the measured moduli, especially in more porous rocks. In our examples shown here, only in the Westerly granite was the bulk modulus used equal to the observed one. One explanation of the need to use smaller intrinsic moduli is that we are limited by the highest pressure in the experiment. In effect, we are fitting spherical and almost spherical cracks to the data at the highest pressure point. However, at 1 kbar, there are still significant amounts of smaller cracks in the rock. This has an effect of lowering the observed moduli. The inversion compensates for this by lowering the matrix moduli. This is just a limit of the resolution of the inversion given the data as a function of a limited range of pressure.

CONCLUSIONS

Laboratory P- and S-wave velocity measurements of dry, benzene-, and water-saturated rock samples have been made at ultrasonic frequencies as a function of confining pressure. The measurements corroborate previous observations on the effect of saturation on P-wave velocities, emphasize the effect of saturation on increasing S-wave velocities, especially at low pressures, and demonstrate differences between benzene- and water-saturated velocities. Modelling of the measurements indicates the importance of pore shape on the velocities.

From the experimental measurements the following conclusions can be made. Similar to previous studies, the introduction of a fluid saturant into a dry rock increases P-wave velocities. The difference between dry and saturated velocities decreases with increasing confining pressure. For rocks where the porosity is dominated by cracks, such as for the granite, the increase in velocity with saturation is large. For rocks where the porosity is dominated by more spherical pores, such as the Bedford limestone, the increase is much less. For the sandstones the increase is as large or larger, as a percentage, as for the granite.

The effects of saturation on the S-wave velocities are less regular. For the crack-dominated rocks, such as the granite, saturation increases S-wave velocities. For the Bedford limestone the saturated S-wave velocities are uniformly lower than dry. The sandstones are intermediate in behavior. At low pressures saturated S-wave velocities are higher while at higher pressures they are lower. For one sandstone, the Weber, saturated S-wave velocities were higher than dry at all pressures.

If the measured P- and S-wave velocities are converted into bulk and shear moduli as a function of pressure the effects of fluid saturation are more clearly defined. Fluid-saturation has a proportionately larger effect on increasing the bulk moduli than the shear moduli. It is important, however, that in this study the benzene-saturated shear modulus is always larger than or, in the case of Bedford limestone, equal to, the dry shear modulus at all pressures. As a function of confining pressure the difference between dry and saturated moduli decrease with higher pressures.

Several effects of benzene versus water as a pore fluid saturant can be interpreted but these are best discussed in terms of the modulus calculations. First, the water-saturated bulk moduli are higher than benzene-saturated values for the sandstones and limestone in accordance with the higher bulk modulus of water. The differences between the two saturated bulk moduli tend to converge with pressure. Second, for the sandstones the water-saturated shear moduli are higher than benzene-saturated and dry values at low pressures (less than about 400 bars) but fall below them at high pressures. For the Bedford limestone water- and benzene-saturated shear moduli are the same at any pressure.

For all of the rocks studied, granite, sandstones, and limestone, the Biot-Gassmann for the calculation of effective bulk modulus of the saturated rock from dry moduli and the pore fluid bulk modulus underestimates saturated P-wave velocities. This is true even if the saturated shear modulus is used in place of the dry shear modulus is calculating P-wave velocities. The equating of dry and saturated shear modulus and the predictior. of saturated S-wave velocities on the basis of saturated density also underestimates S-wave velocities except for the Bedford limestone.

The Bedford limestone approximates a linear elastic solid and the saturated S-wave velocities are accurately predicted on the basis of density change.

The inertial effects of pore fluid at high frequency as treated by Biot (1956a,b) appear to have a negligible influence on saturated velocities. Strong evidence for this is given by the prediction of saturated S-wave velocities in the Bedford limestone solely on the basis of saturated versus dry density. Inertial effects will not increase saturated shear moduli above dry and therefore do not explain high saturated shear moduli in either the granite or sandstones. In the sandstones at high confining pressures, when the effects of cracks are minimized, the inertial effects can be approximated and maximized by using the high frequency analysis. In the measurements confining pressure was probably never high enough to fully meet this criteria but carrying through the analysis indicated that minimum values of the geometrical parameter α would be 4.4 for the Berea sandstone and 2.1 for the Navajo sandstone.

Seismic velocities have been modelled using the Cheng-Kuster-Toksöz model of pore shapes. Dry and benzene-saturated P- and S-wave velocities have been inverted using this model to calculate a spectrum of pore shapes. Static stress-strain measurements were used to determine the rate of pore closure with pressure. The model has been used to predict higher saturated shear moduli upon saturation. The model predicts pores with aspect ratios on the order of 10^{-3} to 10^{-4} are responsible for the increase of saturated moduli over dry and the increase of velocities with pressure. The measured benzene-saturated P- and S-wave velocities for Westerly granite agree very well with the model predictions. Independent checks of the model include porosity decrease with pressure and the prediction of water-saturated velocities as compared with the measured.

Table 1: Rock Samples in this Study

Rock	Density (g/cc)	Grain Size (mm)	Porosity (%)	K_s (Mbar)
Westerly Granite (blue)	2.641	0.75	0.8	0.56
Bedford Limestone	2.360	0.75	11.9	0.65
Weber Sandstone	2.392	0.05	9.5	0.385
Navajo Sandstone	2.316	0.15	11.8	0.36
Berea Sandstone	2.197	0.1	17.8	0.39
Kayenta Sandstone	2.017	0.15	22.2	0.33

Table 2: Pore Fluid Properties At 20-22 °C

Fluid	Pressure (bars)	Density (g/cc)	Bulk Modulus (kbar)	Viscosity Poise
Benzene	100	0.88	12.1	0.007
Water	100	1.00	22.3	0.010

APPENDIX

MATERIALS STUDIED

A short description is given for the rock samples listed in Table 1 and studied in this paper.

Weber sandstone. A dark brown colored, very fine-grained, moderately-sorted, subarkosic sandstone. Grains are subrounded. The sample was obtained from a core received from J. Byerlee's rock mechanics laboratory at the U.S.G.S., Menlo Park, California.

Navajo sandstone. A light straw colored, fine-grained, well-sorted orthoquartzite sandstone. From the upper member of the Navajo formation, as opposed to the lower member, which is red-colored and more porous (studied by Johnston, 1978). Mineralogy consists predominately of subrounded quartz grains (85%) with minor feldspar, chert, and siliceous rock fragments. Minor to moderate secondary quartz is the cementing material.

Berea sandstone. A light buff-gray colored, fine-grained, well-sorted, submature protoquartzite. Mineralogy consists of grains of rounded to subangular quartz, with calcite, siderite, micas, and fine-grained clays. Bedding is indicated by fine striations of dark brown oxidized minerals, probably siderite. Quartz grains are point to concave-convex. Cementing material is calcite, silica, and micas. Samples in this study were obtained from blocks collected at the Buckeye quarry, South Amherst, Ohio. Samples are from the lower, massive sandstone, phase of Berea sandstone, as opposed to the upper, sheet sandstone, phase (Pepper et al., 1954). Simmons et al. (1982) described the pore geometry of Berea sandstone as seen by the SEM in crack section and pore cast. Pore geometry is described as a network of intergranular and connective pores which are relatively uniform in size, with irregular intergranular pores smaller than individual grains and many connective pores as thin, curved planes. Khilar and Fogler (1983) give a mineralogical content for a typical Berea sandstone sample as 76% quartz, 9% feldspars, 1% calcite, 4% dolomite, 1% siderite, 7% kaolinite, 1% chlorite, and 1% illite/mica. Lene and Owen (1969) give the modal analysis of Berea sandstone at the Buckeye quarry as 76.4% quartz, 11.2% chert, 4.6% feldspars, 1.1% leucoxene, 0.4% zircon, 0.3% tourmaline, 0.4% muscovite, 0.4% chlorite, 2.6% siderite, and 2.5% calcite. Lene and Owen (1969) also give the grain-size parameters of Folk and Ward (1957): mean is 2.70 φ (fine-grained), sorting is 0.61 φ (moderately well sorted), skewness is 0.47 (strongly fine-skewed), and kurtosis is 2.05 (very leptokurtic). Tosaya and Nur (1983) report that clays are mixed illite-kaolinite on the basis of X-ray diffraction.

Kayenta sandstone. A light yellow colored, medium to coarse-grained, poorly consolidated arkosic sandstone. Mineralogy consists primarily of quartz grains with feldspar and calcite as the cementing material. Modal analysis for a sample of Kayenta sandstone given by Brace (1974) is 52% quartz, 21% orthoclase, 20% calcite, and 7% microcline opaque lithic fragments. Sample appears however to have approximately 20% clay (illite or kaolinite) in thin section.

Bedford limestone. A light tannish-gray colored, coarse-grained, poorly-sorted, well-cemented calcarenite, brecciated limestone, or coquina consisting of poorly sorted clastic calcite fossil debris. Crystalline calcite is the cementing material. Pore space is vuggy and irregularly scattered. Bedding is indicated by faint, broad laminations on a wetted surface. Sample was cored from a rock cube obtained from stock at the U.S. Bureau of Mines Twin Cities Mining Research Center, the properties of which are reported in Krech et al. (1974). Mineralogy is reported by the same to be 69% fossiliferous calcite (shells of gastropods, crinoid stems and calices) and 31% calcite cement.

Westerly granite. The blue variety of Westerly granite was collected at the Bonner Monument Co. in Westerly, R.I. Mineralogies of the red and blue varieties are indistinguishable. Both are fine-grained, equigranular, biotite granites of very uniform texture and grain size. Mineralogy consists of subhedral plagioclase and microcline feldspar, anhedral quartz, subhedral biotite and muscovite, and opaque accessory minerals. Modal analysis reported in Brace (1965) is 35.4% microcline, 31.4% plagioclase (17% anorthite), 27.5% quartz, 4.9% mica. Modal analysis reported in Siegfried and Simmons (1978) is 22.5% quartz, 30.7% potassium feldspar, 39.2% plagioclase (17% anorthite), 5.0% biotite, 0.7% muscovite, 0.7% opaques, 0.4% secondary minerals, and 0.8% others. Feves and Simmons (1976) compare the compositions of several samples of Westerly granite. Modal analysis reported in Krech et al. (1974) for a light gray colored variety is 43% plagioclase, 22% microcline, 24.6% quartz, 6.9% biotite, 2.0% muscovite, 1.0% zicron, 0.9% magnetite.

REFERENCES

Banthia, B.S., King, M.S., and Fatt, I., 1965, Ultrasonic shear-wave velocities in rocks subjected to simulated overburden pressure and internal pore pressure: Geophysics, 30, 117-121.

Biot, M.A., 1956a, Theory of propagation of elastic waves in a fluid-saturated porous solid - I. Low frequency range: J. Acoust. Soc. Am., 28, 168-178.

Biot, M.A., 1956b, Theory of propagation of elastic waves in a fluid-saturated porous solid - II. Higher frequency range: J. Acoust. Soc. Am., 28, 179-191.

Biot, M.A., 1962a, Mechanics of deformation and acoustic propagation in porous media: J. Appl. Phys., 33, 1482-1498.

Biot, M.A., 1962b, Generalized theory of acoustic propagation in porous dissipative media: J. Acoust. Soc. Am., 34, 1254-1264.

Birch, F., 1960, The velocity of compressional waves in rocks to 10 kb, part 1: J. Geophys. Res., 65, 1083-1102.

Birch, F., 1961, The velocity of compressional waves in rocks to 10 kb, part 2: J. Geophys. Res., 66, 2199.

Birch, F., 1966, Compressibility elastic constants: in Handbook of Physical Constants, Geol. Soc. Am. Mem. 97, 97-173.

Brown, R.J.S. and Korringa, J., 1975, On the dependence of the elastic properties of a porous rock on the compressibility of the pore fluid: Geophysics, 40, 608-616.

Cheng, C.H., 1978, Seismic velocities in porous rocks: direct and inverse problems: PhD. thesis, M.I.T., Cambridge, Ma.

Cheng, C.H. and Johnston, D.H., 1981, Dynamic and Static Moduli: Geophys. Res. Letters, 8, 39-42.

Coyner, K.B., 1984, Static deformation of fluid-saturated rocks: M.I.T. Full Waveform Acoustic Logging Consortium Annual Report, 1984, Paper 12, 289-356.

Engineering Sciences Data, Items 68010, 71003, 77024, 78040.

Gardner, H.F., Wyllie, M.R.J. and Droschak, D.M., 1965, Hysteresis in the velocity-pressure characteristics of rocks: Geophysics, 30, 111-116.

Gassmann, F., 1951, Uber die elastizitat poroser medien: Vierteljahrsschr. Naturforsch. Ges. Zurich, 96, 1-21.

Hughes, D.S. and Cooke, C.E., 1953, The effect of pressure on the reduction of pore volume of consolidated sandstones: Geophysics, 18, 298-309.

Hughes, D.S., and Cross, J.H., 1951, Elastic wave velocities in rocks at high pressures and temperatures: Geophysics, 16, 577-593.

Johnston, D.H., 1978, The attenuation of seismic waves in dry and saturated rocks: Ph.D. thesis, M.I.T., Cambridge, Ma.

Jones, T., and Nur, A., 1984, Velocity and attenuation in sandstone at elevated temperatures and pressures, Geophys. Res. Lett., 10, 140-143.

Khilar, K.C., and Fogler, 1983, Water sensitivity of sandstones: J. Soc. Pet. Eng., AIME, 55-64.

King, M.S., 1966, Wave velocities in rocks as a function of changes in overburden pressure and pore fluid saturants: Geophysics, 31, 50-73.

Korringa, J., Brown, R.J.S., Thompson, D.D., and Runge, R.J., 1979, Self-consistent imbedding and the ellipsoidal model for porous rocks: J. Geophys. Res., 84, 5591-5598.

Love, A.E.H., 1944, A Treatise on the Mathematical Theory of Elasticity, Dover, New York.

Mann, R.L. and Fatt, I., 1960, Effect of pore fluids on the elastic properties of sandstones: Geophysics, 25, 433-444.

Murphy, W.F., 1984, Acoustic measures of partial gas saturation in tight sandstones, J. Geophys. Res., 11549-11559.

Nur, A., 1969, Effects of stress and fluid inclusions on wave propagation in rocks: Ph.D. Thesis, M.I.T., Cambridge, Ma.

Nur, A. and Simmons, G., 1969, The effect of saturation on velocity in low porosity rocks: Earth Planet. Sci. Lett., 7, 183-193.

O'Connell, R.J. and Budiansky, B., 1974, Seismic velocities in dry and saturated cracked solids: J. Geophys. Res., 79, 5412-5426.

O'Connell, R.J. and Budiansky, B., 1977, Viscoelastic properties of fluid-saturated cracked solids: J. Geophys. Res., 82, 5719-5735.

Perry, R.H., and Chilton, C.H., editors, Chemical Engineers Handbook, 5th ed., McGraw-Hill, 1973.

Simmons, G., 1964, Velocity of shear waves in rocks to 10 kilobars, 1: J. Geophys. Res., 69, 1123.

Simmons, G., Wilkens, R., Caruso, L., Wissler, T., and Miller, F., 1982, Physical properties and microstructures of a set of sandstones, and annual report to the Schlumberger-Doll Research Center.

Spencer, J.W., 1979, Bulk and shear attenuation in Berea sandstone: the effects of pore fluids: J. Geophys. Res., 84, 7521-7523.

Spencer, J.W., 1981, Stress relaxations at low frequencies in fluid- saturated rocks: attenuation and modulus dispersion: J. Geophys. Res., 86, 1803-1812.

Spencer, J.W., and Nur, A.M., The effects of pressure, temperature, and pore water on

velocities in Westerly granite, J. Geophys. Res., 81, 899-904.

Stephen, K., and Lucas, K., Viscosity of Dense Fluids, Plenum Press, 1979, 268 pp.

Tittmann, B.R., Nadler, H., Clark, V.A., and L.A. Ahlberg, 1981, Frequency dependence of seismic dissipation in saturated rocks, Geophy. Res. Lett., 8, 36-38.

Toksöz, M.N., Cheng, C.H., and Timur, A., 1976, Velocities of seismic waves in porous rocks: Geophysics, 41, 621-645.

Tosaya, C., and Nur, A., 1982, Effects of diagenesis and clays on compressional velocities in rocks: Geophy. Res. Letters, 9, 5-8.

Walsh, J.B., 1965, The effect of cracks on the compressibility of rocks: J. Geophys. Res., 70, 381-389.

Winkler ,K., and Nur, A., 1979, Pore fluids and seismic attenuation in rocks, Geophy. Res. Lett., 6, 1-4.

Wyllie, M.R.J., Gregory, A.R. and Gardner, G.H.F., 1958, An experimental investigation of factors affecting elastic wave velocities in porous media: Geophysics, 23, 459-493.

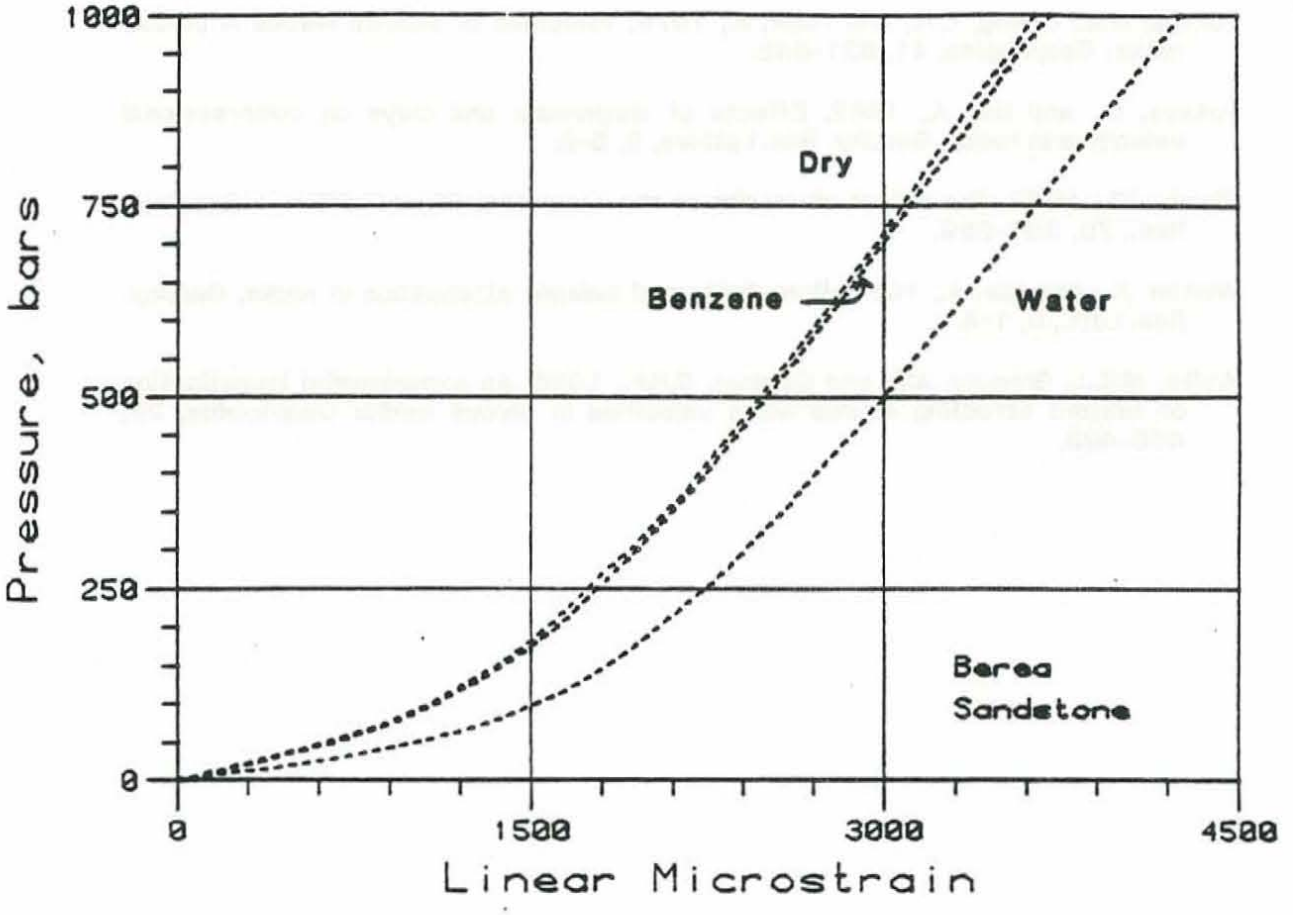

Figure 1. Vacuum dry, water saturated, and benzene saturated stress-strain relations for a sample of Berea sandstone. Saturated pore pressures are 1 bar (drained to atmospheric pressure).

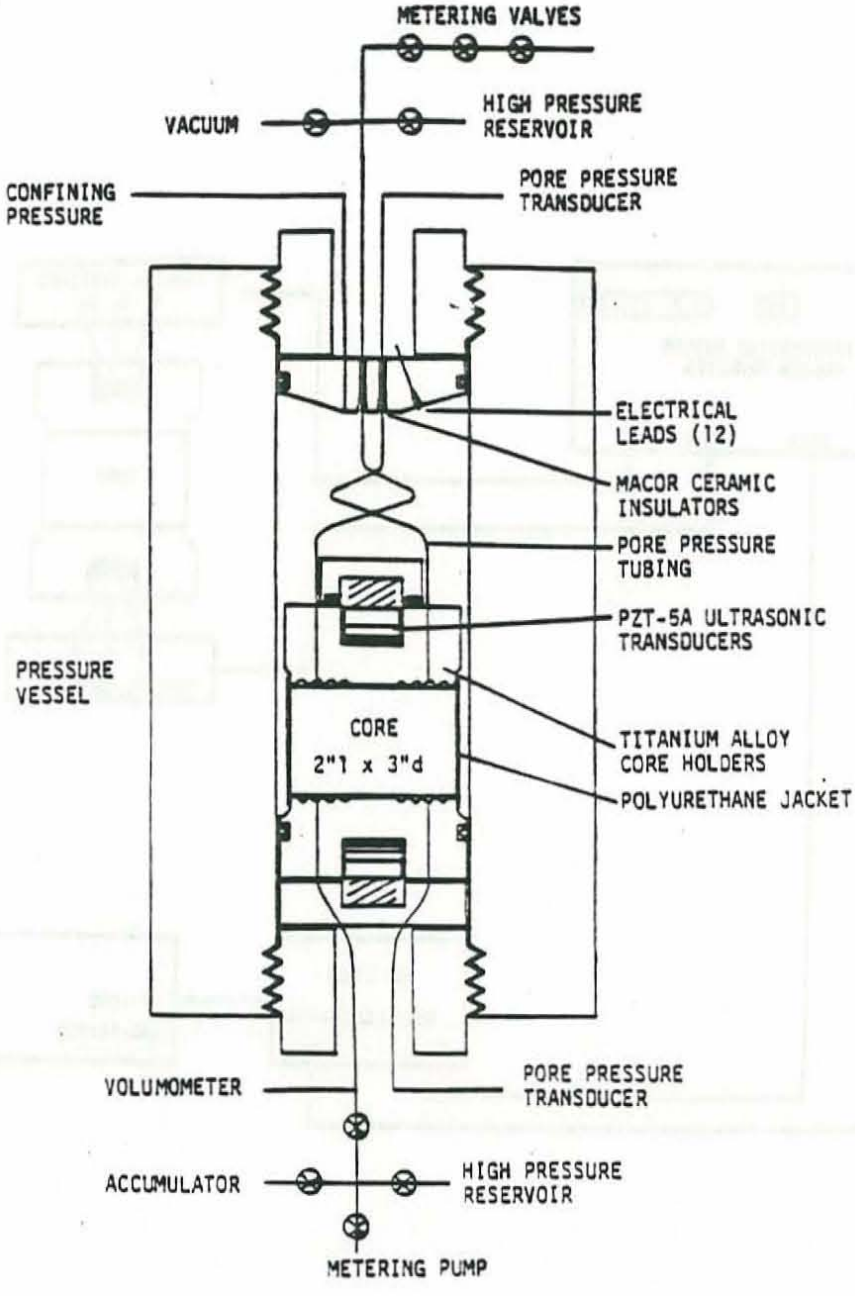

Figure 2. High pressure experimental apparatus for the measurement of P- and S-wave velocities. Hydrostatic confining pressure and pore fluid pressure are independently controlled.

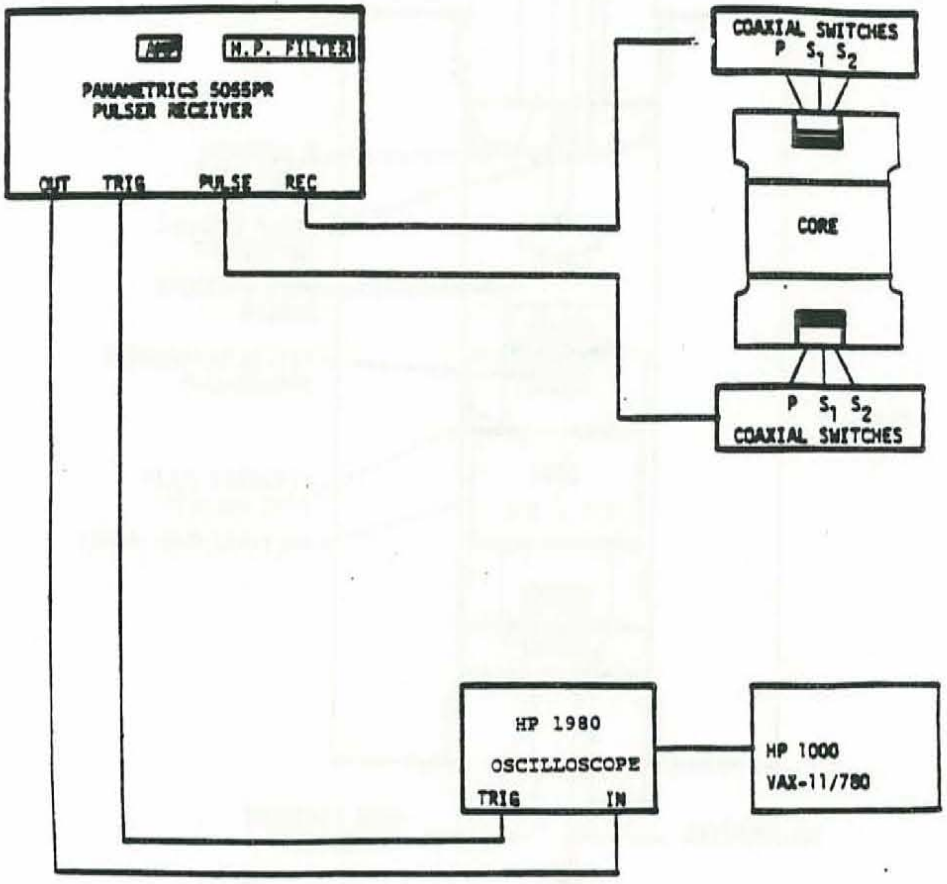

Figure 3. Block diagram of sample with transducer heads and electronics used to measure ultrasonic velocities and to record waveforms.

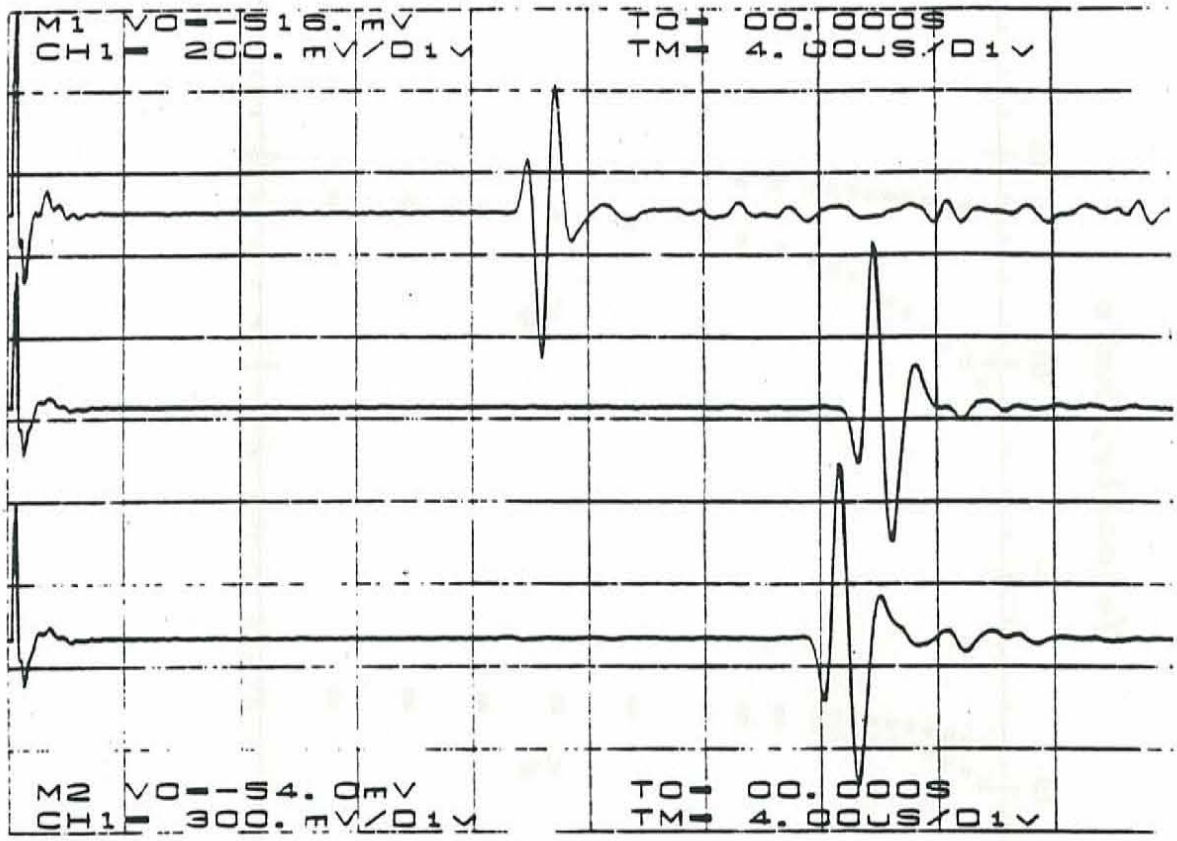

Figure 4. Examples of ultrasonic waveforms sequentially measured through a 5 cm thick core of Navajo sandstone at 1000 bars confining pressure. Top trace is P-wave and the lower 2 traces are S-waves oriented at 90 degrees to each other. Signals are attenuated by 10 dB. The vertical voltage scale is 200 mv/div for the P-wave and 300 mv/div for the S-wave signals. Time is horizontal (4 μs/div) and the lefthand edge of the plot is the zero time at which the source is excited. Delay time introduced by the titanium transducer holders is approximately 7.54 μs for the P-wave, 13.7 μs for the middle S-wave, and 12.45 μs for the lower S-wave. S-wave arrival times are offset in the mechanical transducer design to isolate crosstalk.

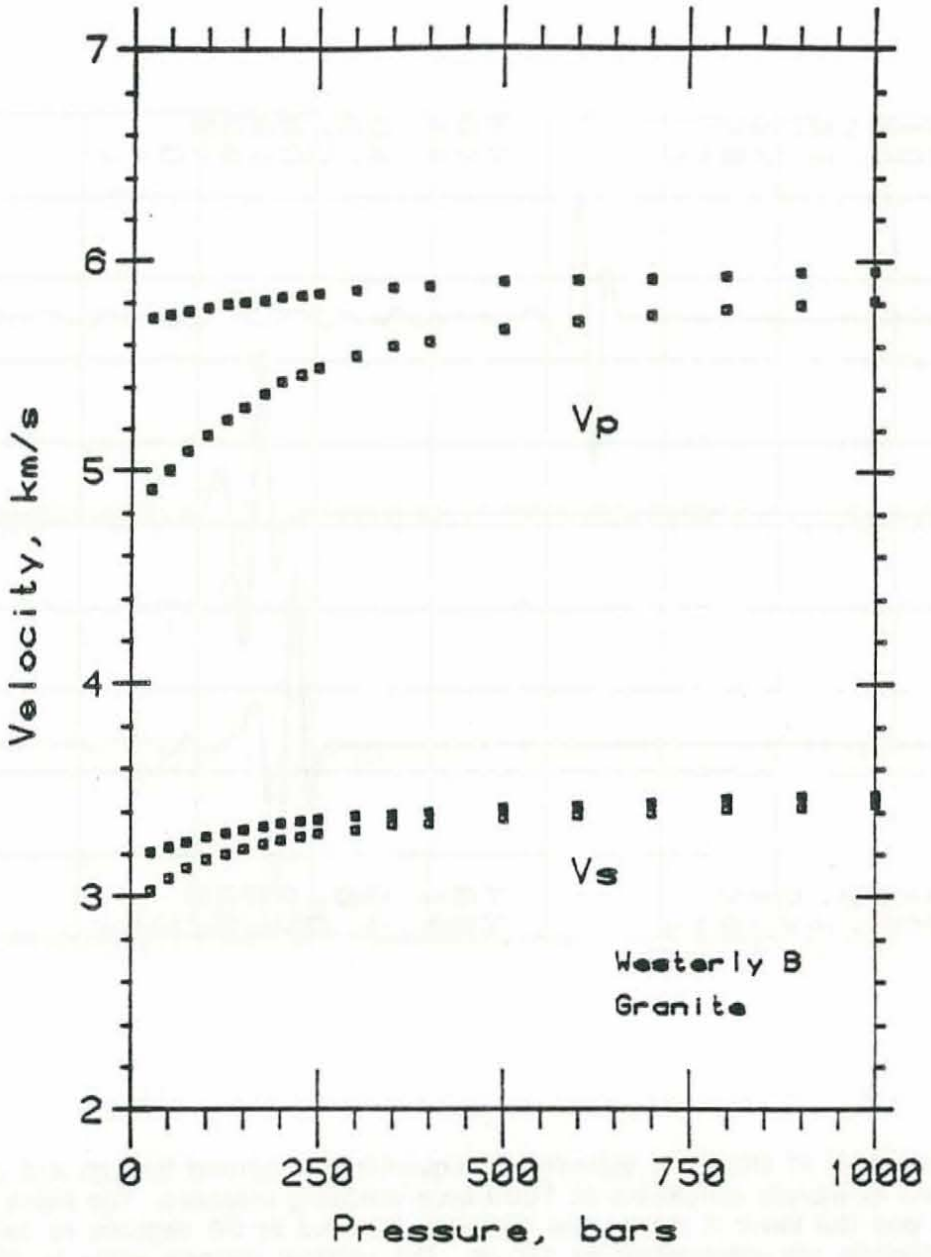

Figure 5. P- and S-wave velocities for Westerly granite versus differential pressure for dry (open squares; 20 μm Hg vacuum) and benzene (solid squares; 100 bars pore pressure) saturations.

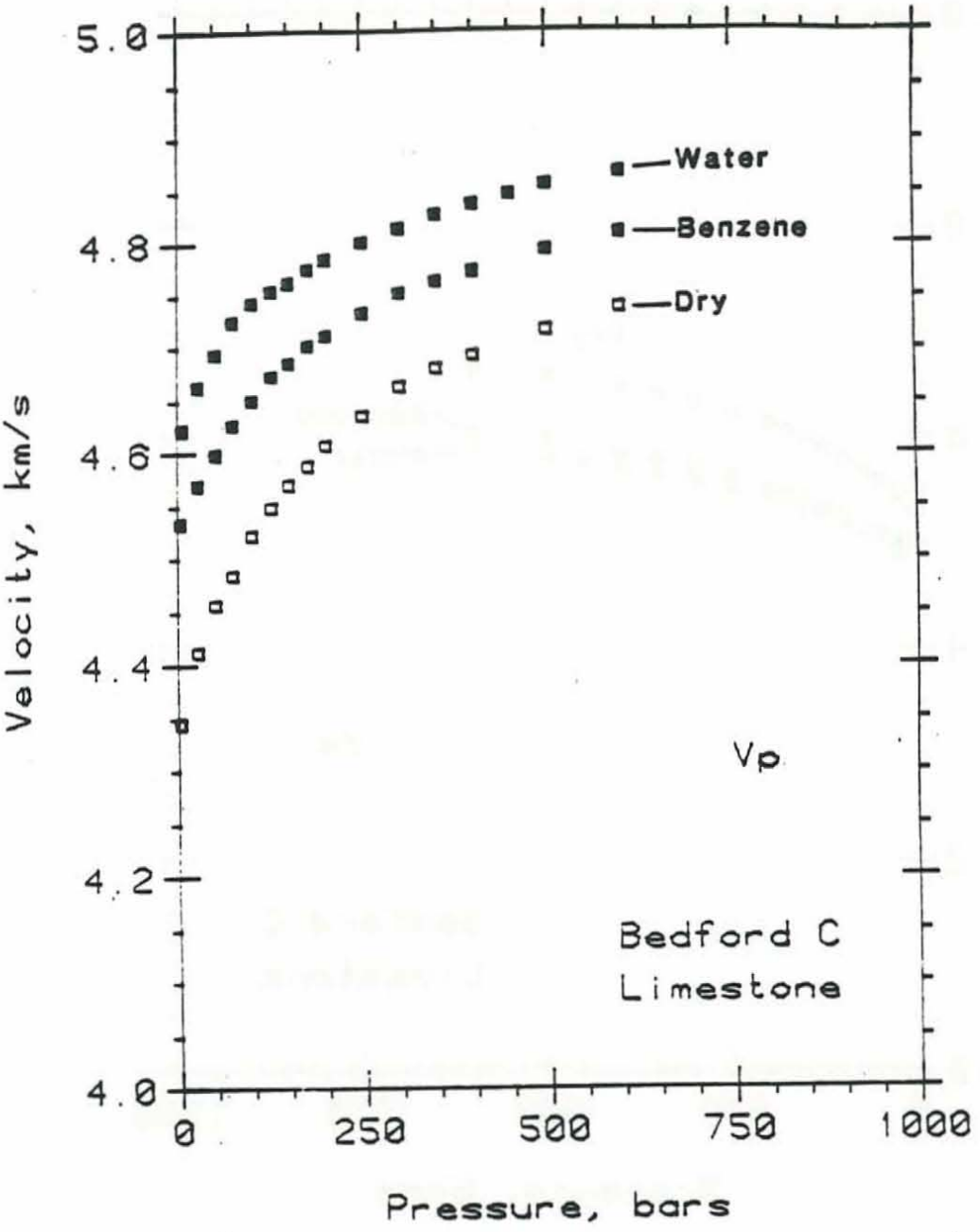

Figure 6. P-wave velocities for Bedford limestone versus differential pressure for dry (open squares; 20 μm Hg vacuum), benzene (labelled solid squares; 100 bars pore pressure), and distilled water (labelled solid squares; 100 bars pore pressure) saturations. Propagation direction parallel with bedding.

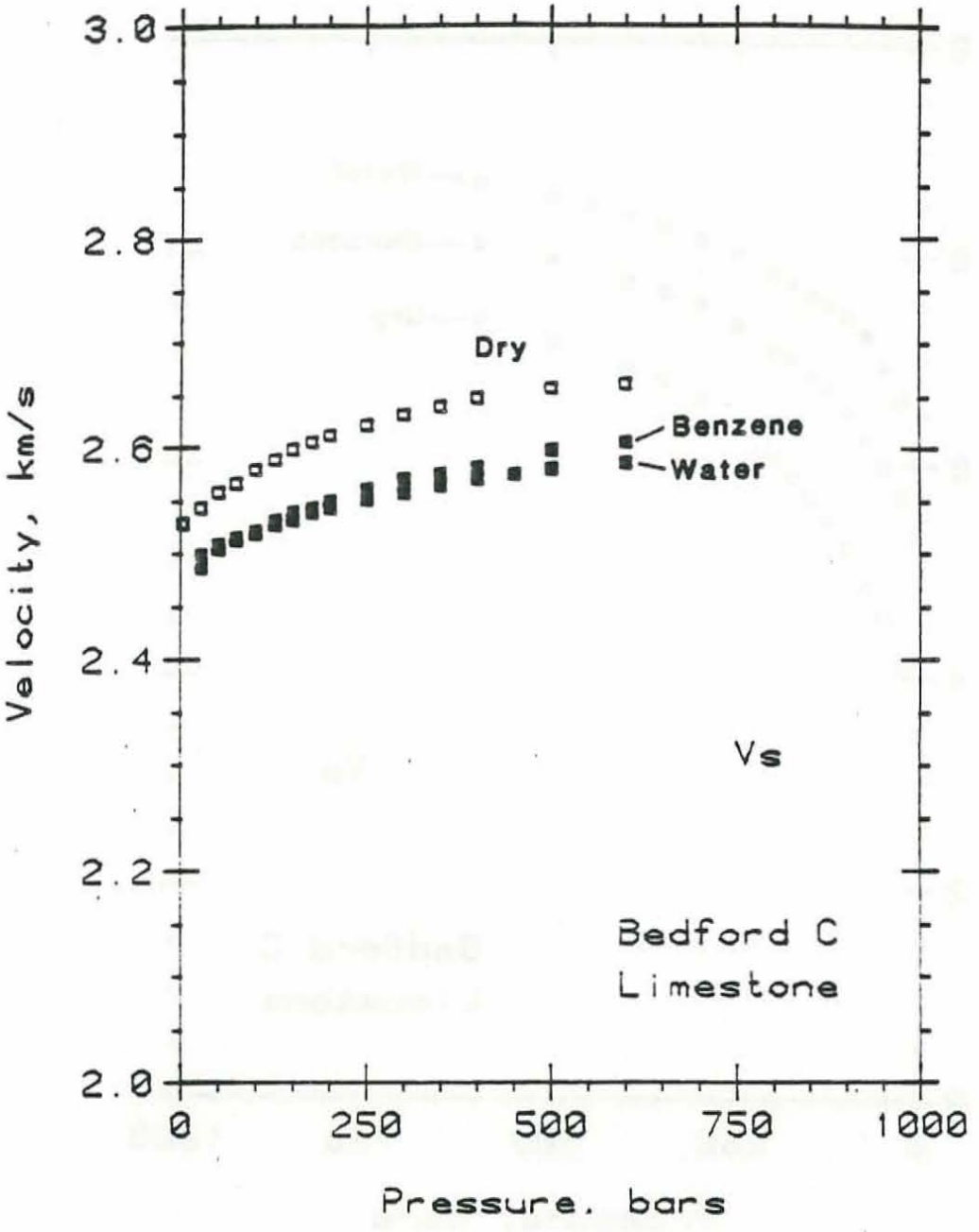

Figure 7. S-wave velocities for Bedford limestone versus differential pressure for dry (open squares; 20 μm Hg vacuum), benzene (labelled solid squares; 100 bars pore pressure), and distilled water (labelled solid squares; 100 bars pore pressure) saturations. Propagation direction parallel with bedding; sense of shear perpendicular to bedding.

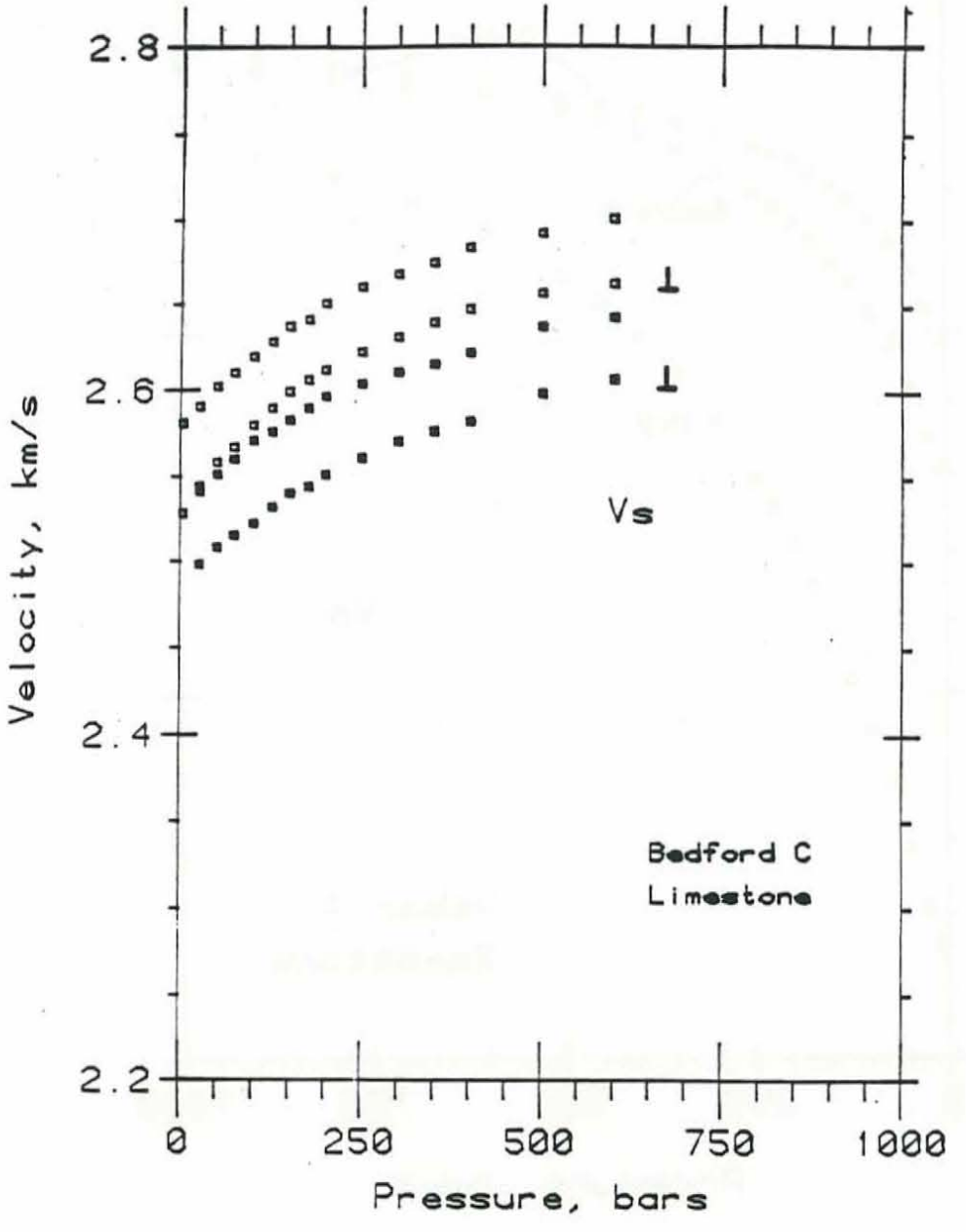

Figure 8. S-wave velocities in two directions for Bedford limestone versus differential pressure for dry (open squares; 20 μm Hg vacuum) and benzene (solid squares; 100 bars pore pressure) saturations. Propagation direction parallel with bedding. Sense of shear for labelled set of velocities perpendicular to bedding.

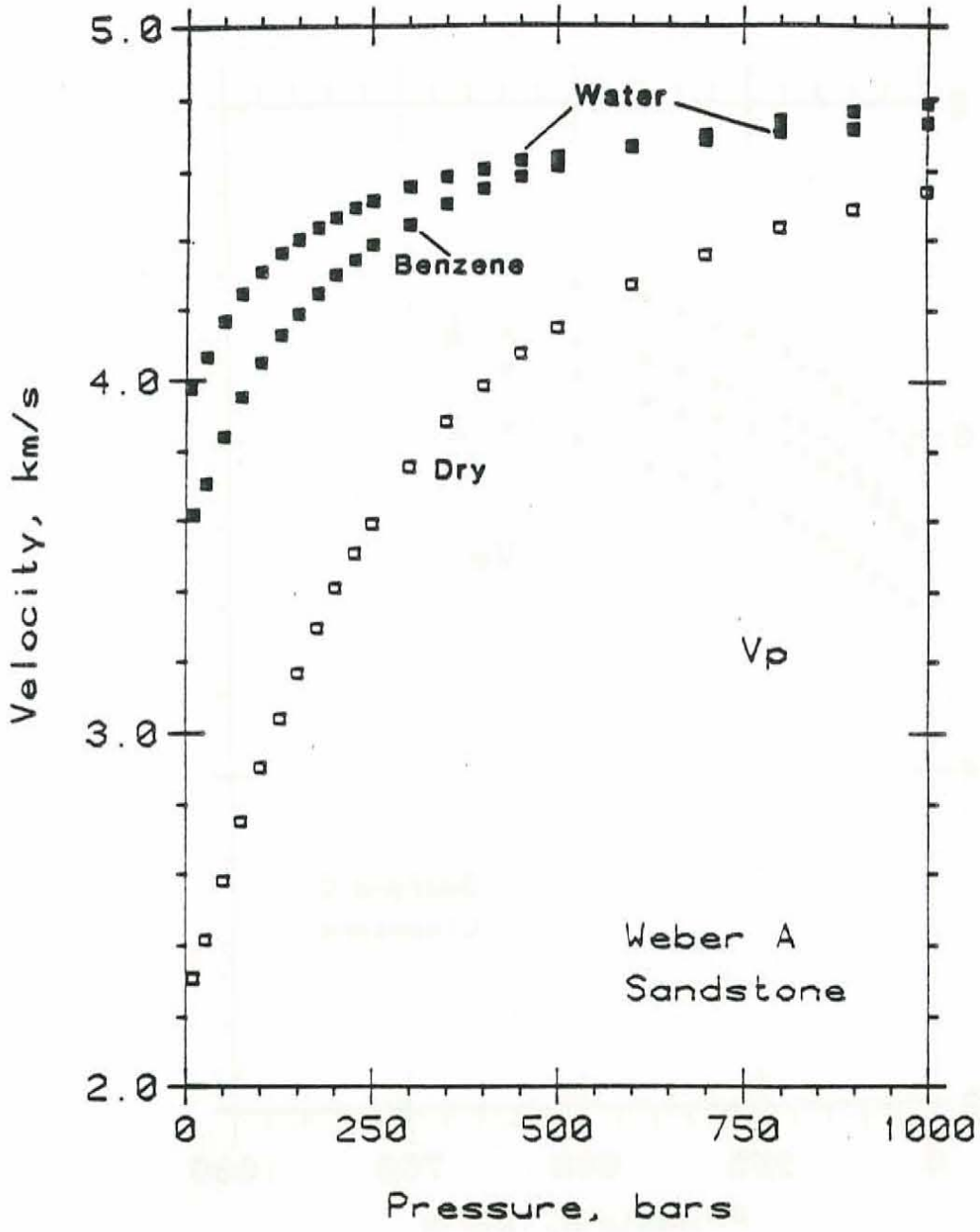

Figure 9. P-wave velocities for Weber sandstone versus differential pressure for dry (open squares; 20 μm Hg vacuum), benzene (labelled solid squares; 100 bars pore pressure), and distilled water (labelled solid squares; 100 bars pore pressure) saturations. Propagation direction perpendicular to bedding.

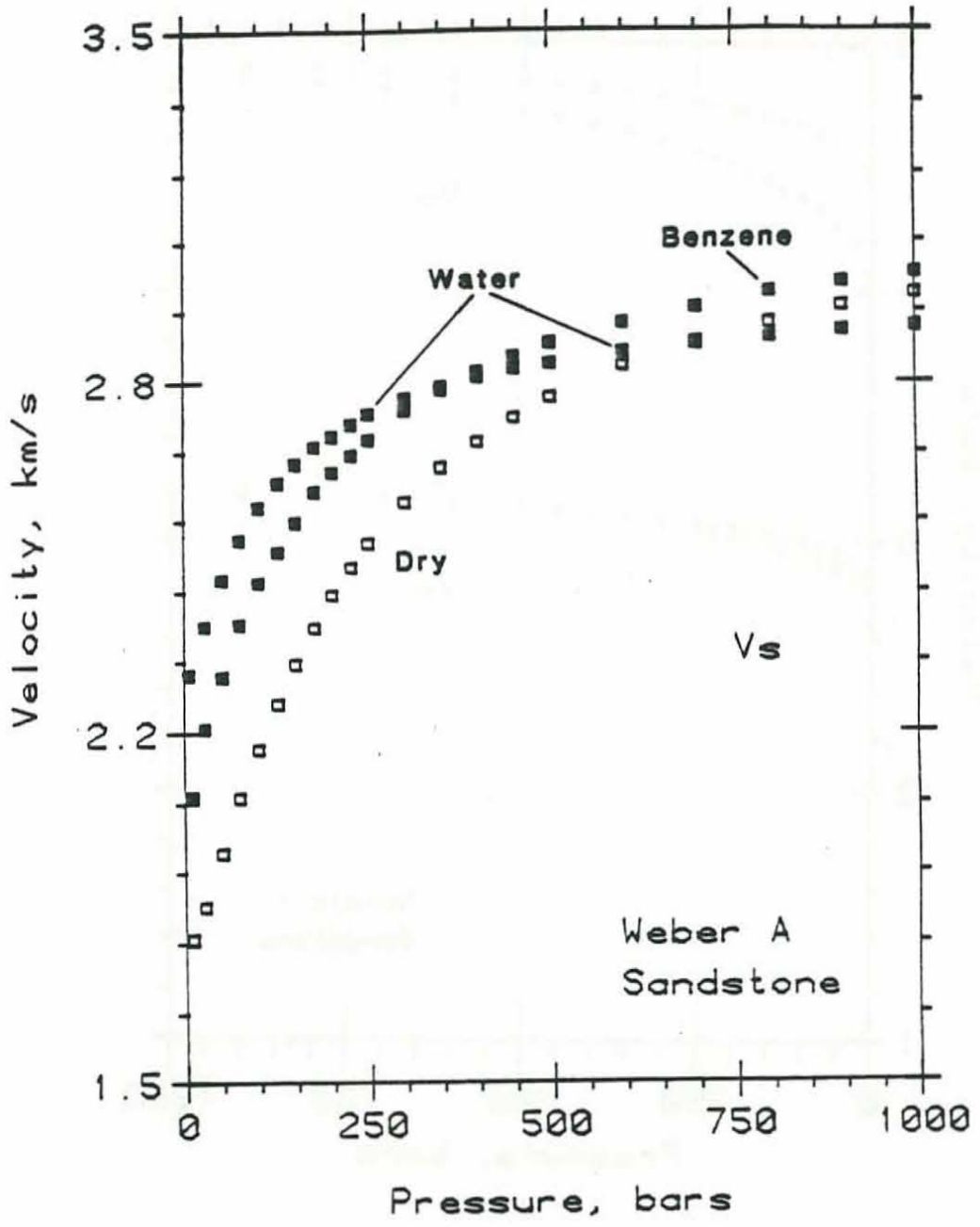

Figure 10. S-wave velocities for Weber sandstone versus differential pressure for dry (open squares; 20 μm Hg vacuum), benzene (labelled solid squares; 100 bars pore pressure), and distilled water (labelled solid squares; 100 bars pore pressure) saturations. Propagation direction perpendicular to bedding.

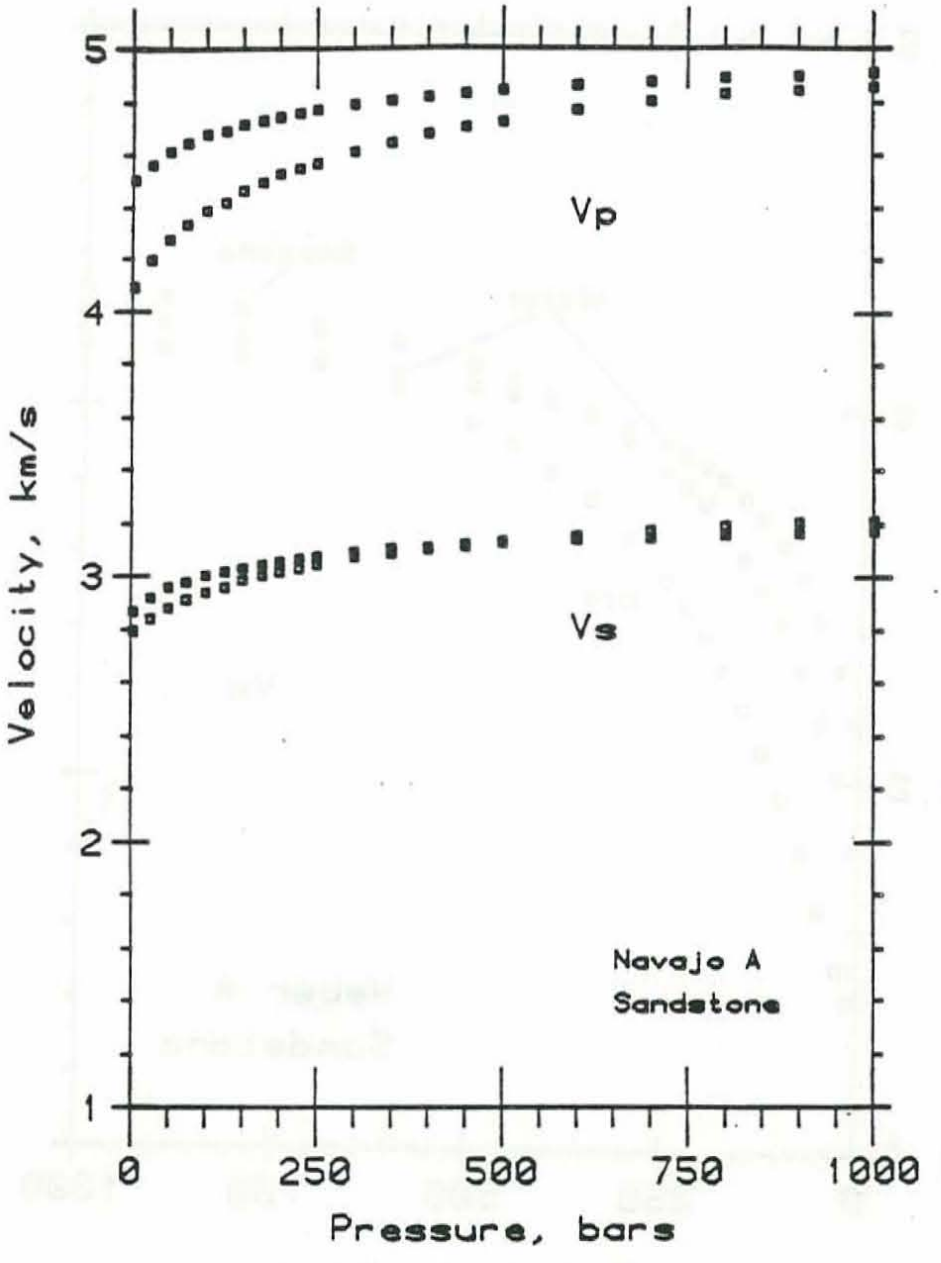

Figure 11. P- and S-wave velocities for Navajo sandstone versus differential pressure for dry (open squares; 20 μm Hg vacuum) and benzene (solid squares; 100 bars pore pressure) saturations. Propagation direction perpendicular to bedding.

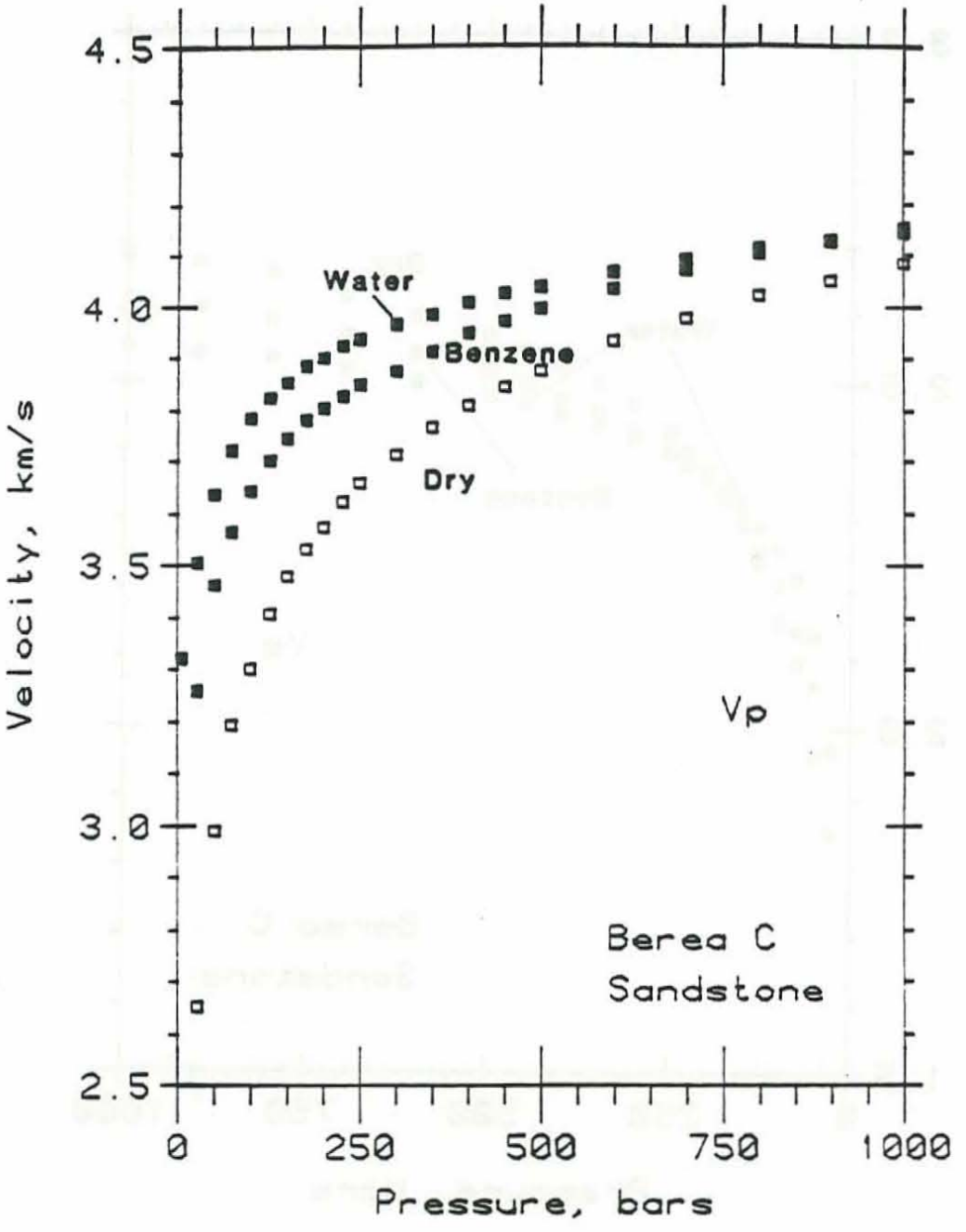

Figure 12. P-wave velocities for Berea sandstone versus differential pressure for dry (open squares; 20 μm Hg vacuum), benzene (labelled solid squares; 100 bars pore pressure), and distilled water (labelled solid squares; 100 bars pore pressure) saturations. Propagation direction parallel to bedding.

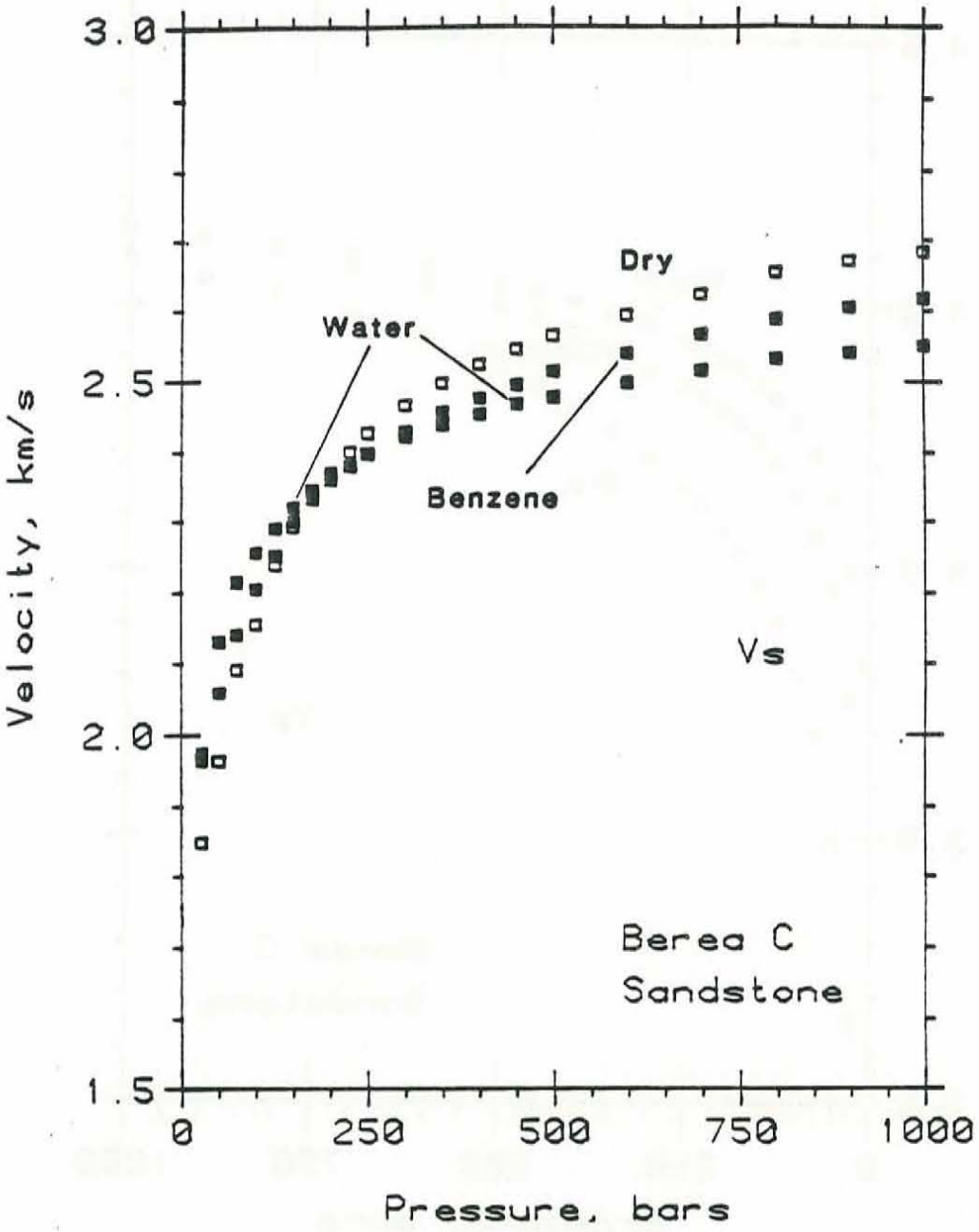

Figure 13. S-wave velocities for Berea sandstone versus differential pressure for dry (open squares; 20 μm Hg vacuum), benzene (labelled solid squares; 100 bars pore pressure), and distilled water (labelled solid squares; 100 bars pore pressure) saturations. Propagation direction parallel with bedding.

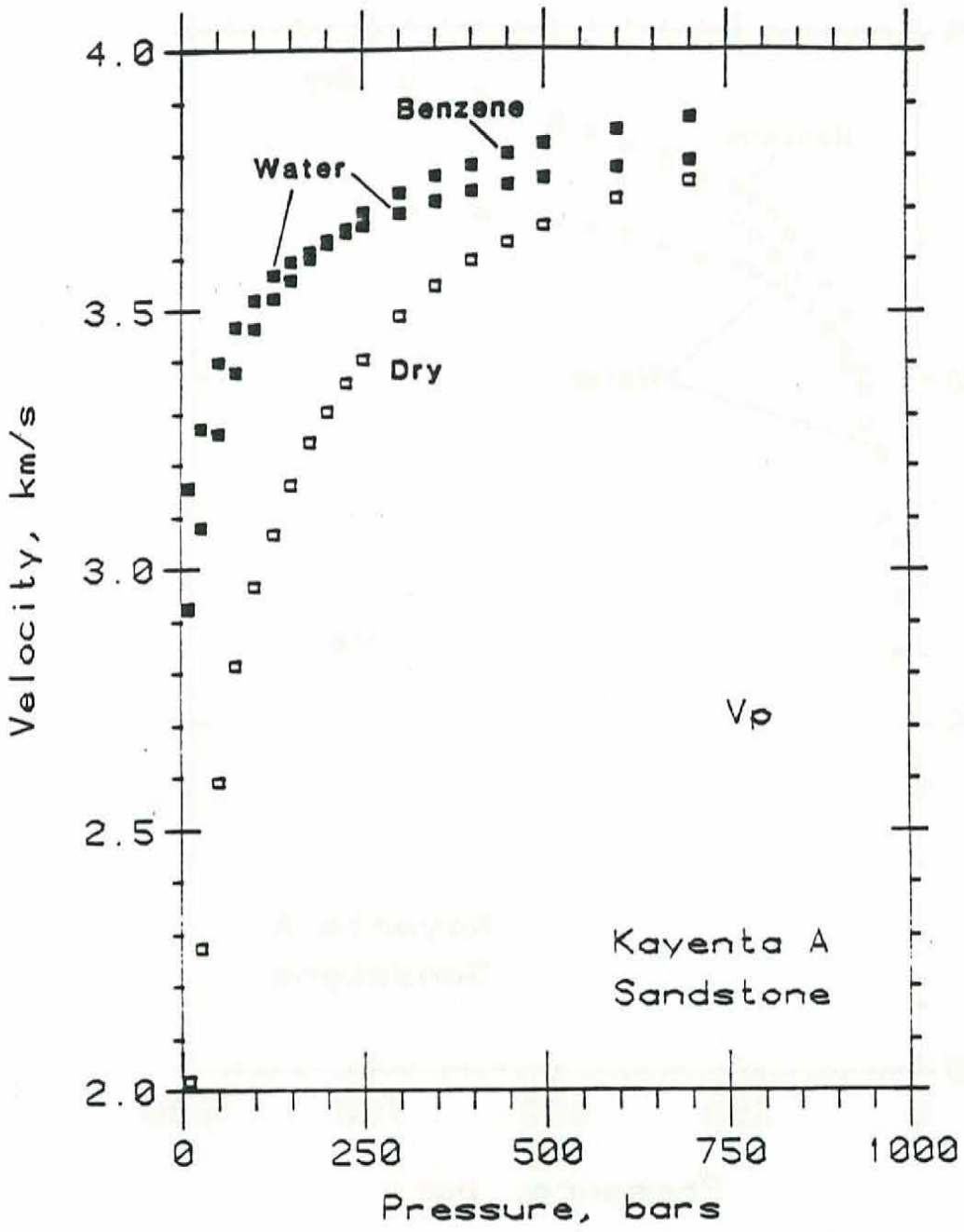

Figure 14. P-wave velocities for Kayenta sandstone versus differential pressure for dry (open squares; 20 μm Hg vacuum), benzene (labelled solid squares; 100 bars pore pressure), and distilled water (labelled solid squares; 100 bars pore pressure) saturations. Propagation direction perpendicular to bedding.

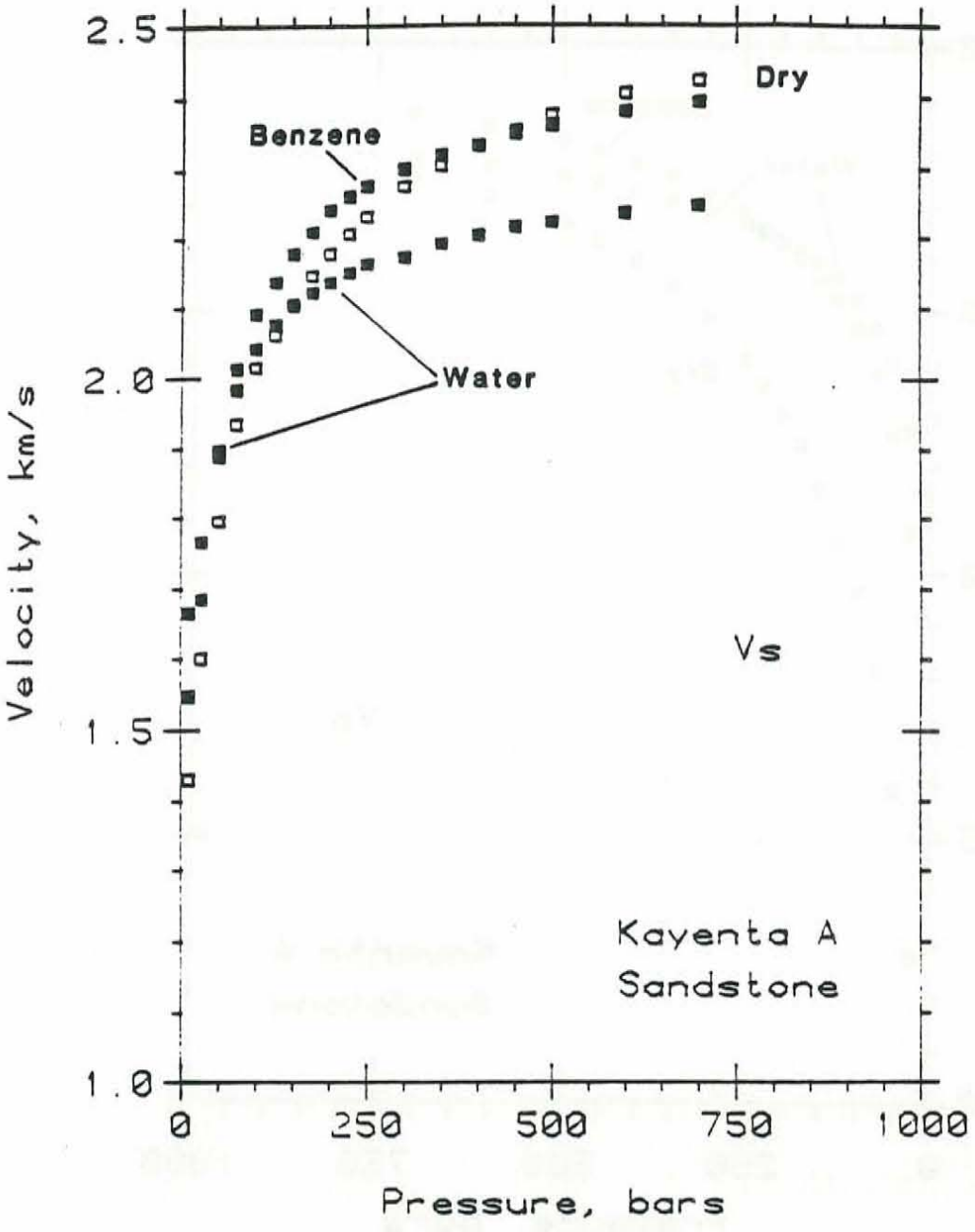

Figure 15. S-wave velocities for Kayenta sandstone versus differential pressure for dry (open squares; 20 μm Hg vacuum), benzene (labelled solid squares; 100 bars pore pressure), and distilled water (labelled solid squares; 100 bars pore pressure) saturations. Propagation direction perpendicular to bedding.

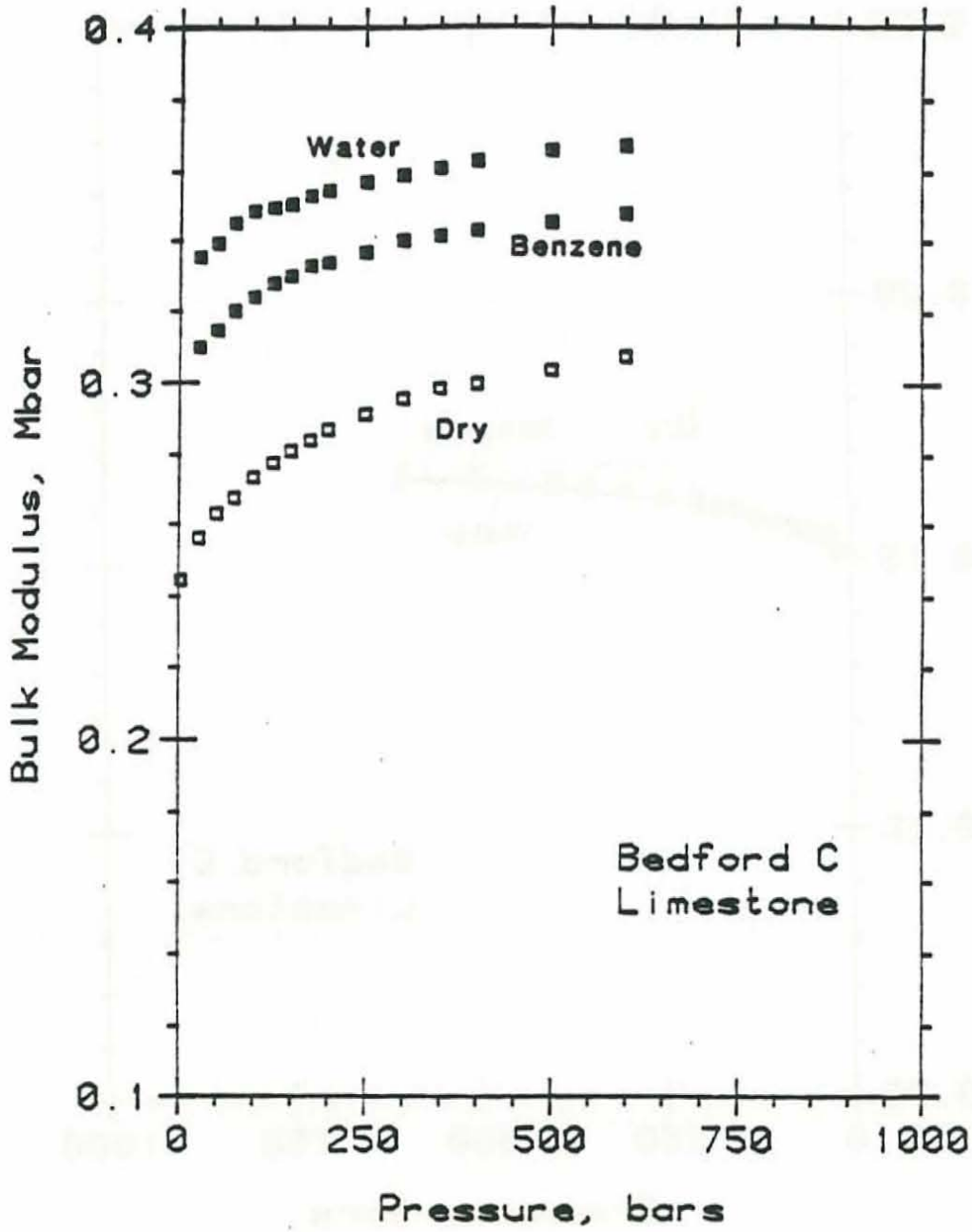

Figure 16. Vacuum dry, benzene-, and water-saturated bulk moduli for Bedford limestone as a function of differential pressure.

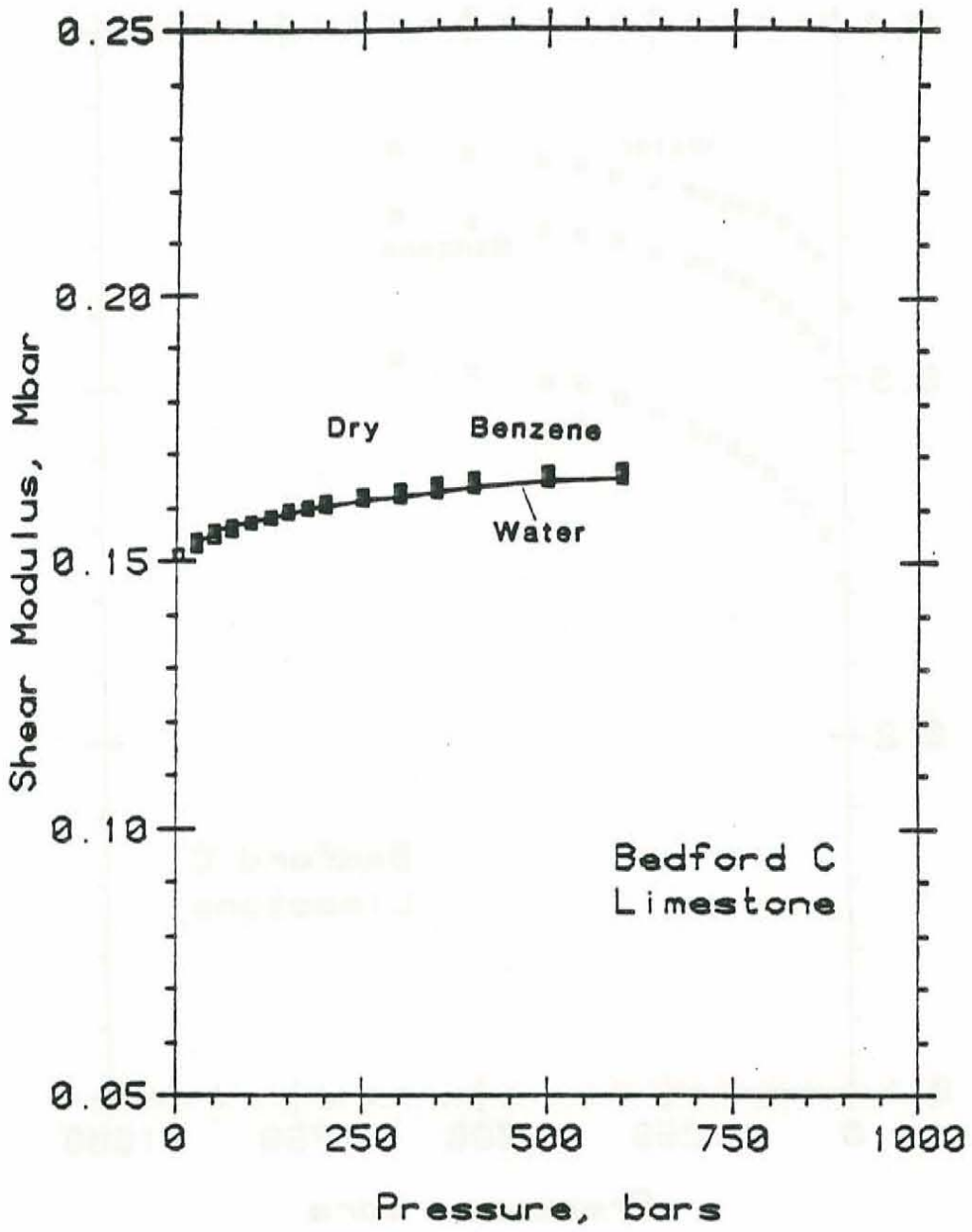

Figure 17. Vacuum dry, benzene-, and water-saturated shear moduli for Bedford limestone as a function of differential pressure.

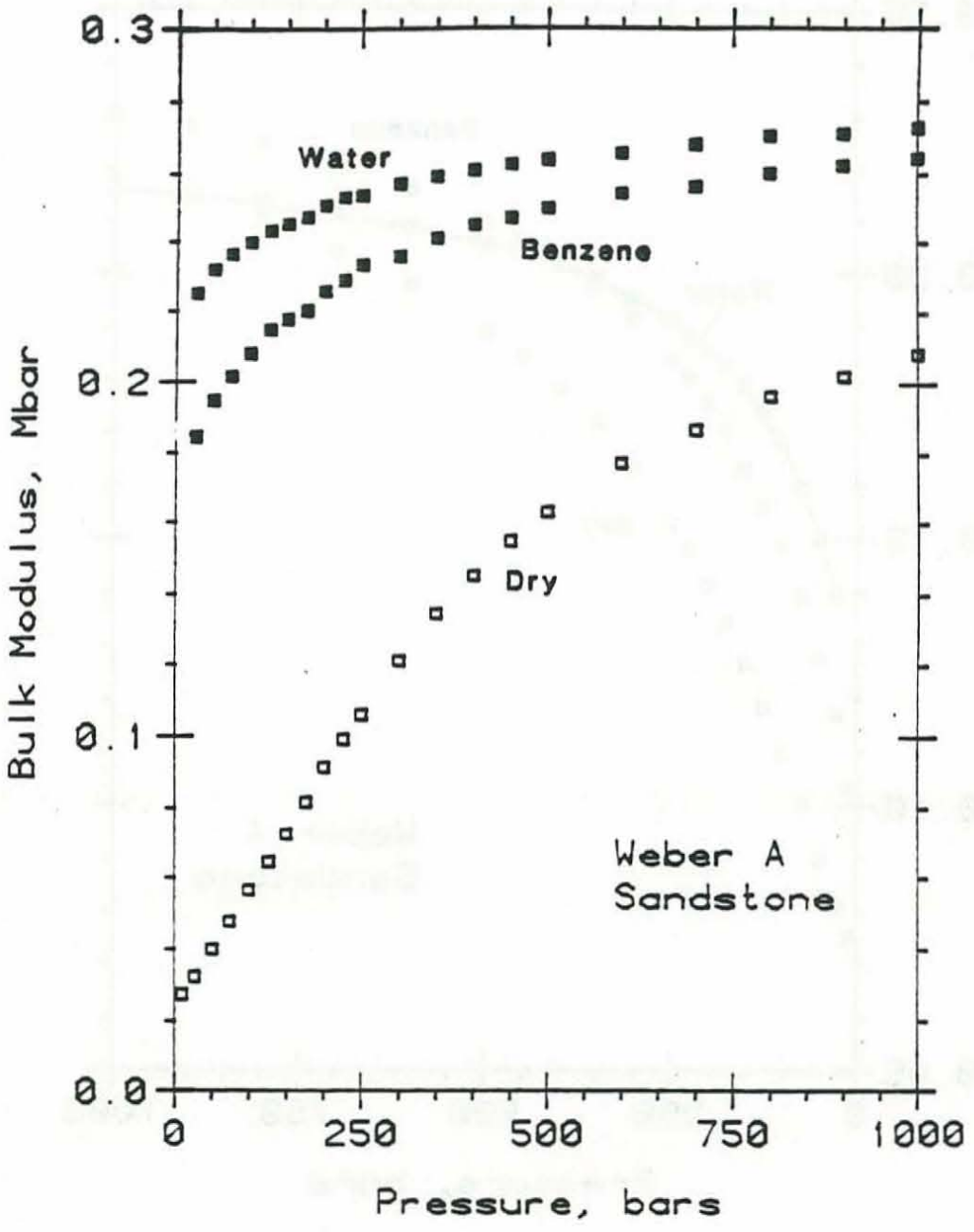

Figure 18. Vacuum dry, benzene-, and water-saturated bulk moduli for Weber sandstone as a function of differential pressure.

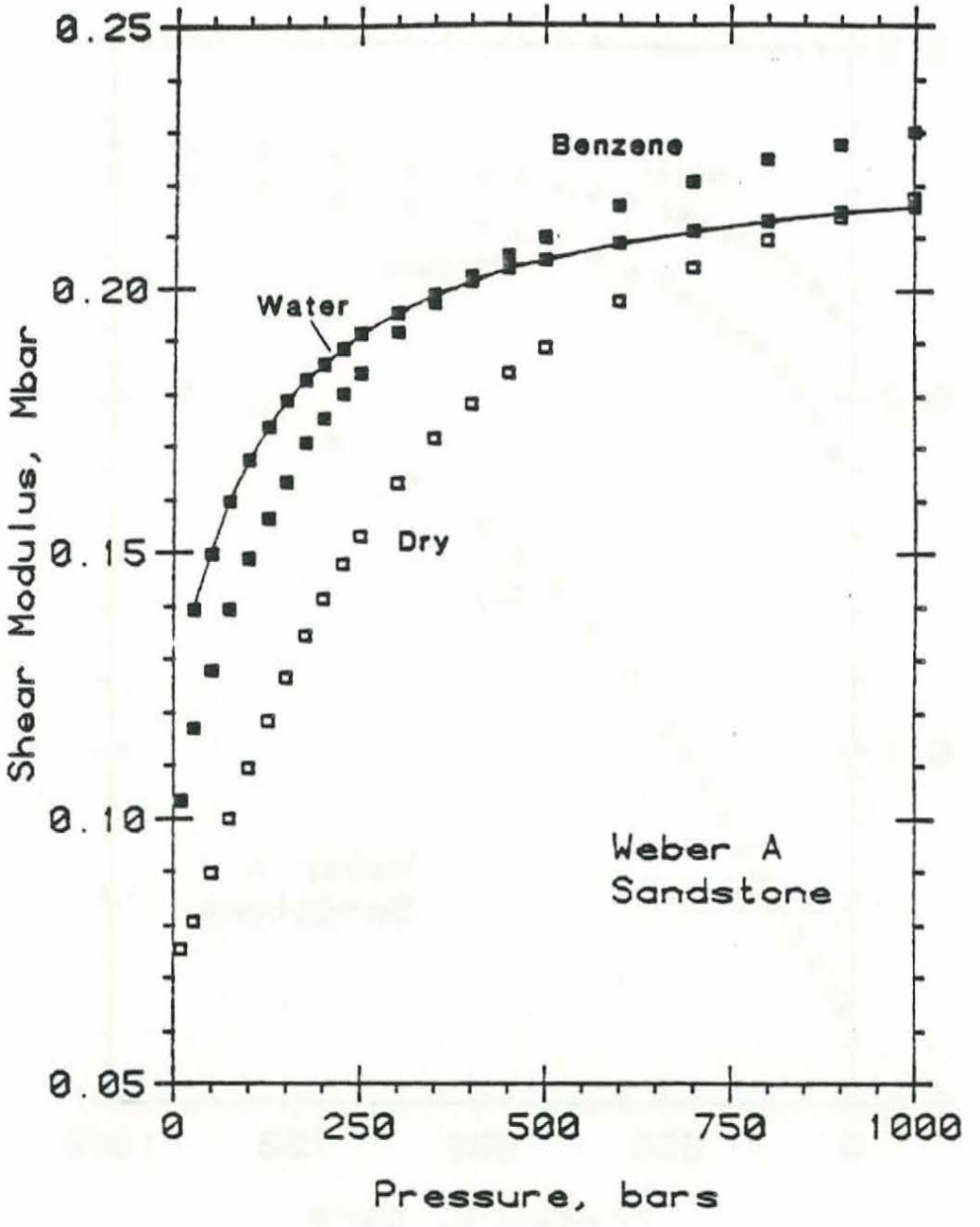

Figure 19. Vacuum dry, benzene-, and water-saturated shear moduli for Weber sandstone as a function of differential pressure.

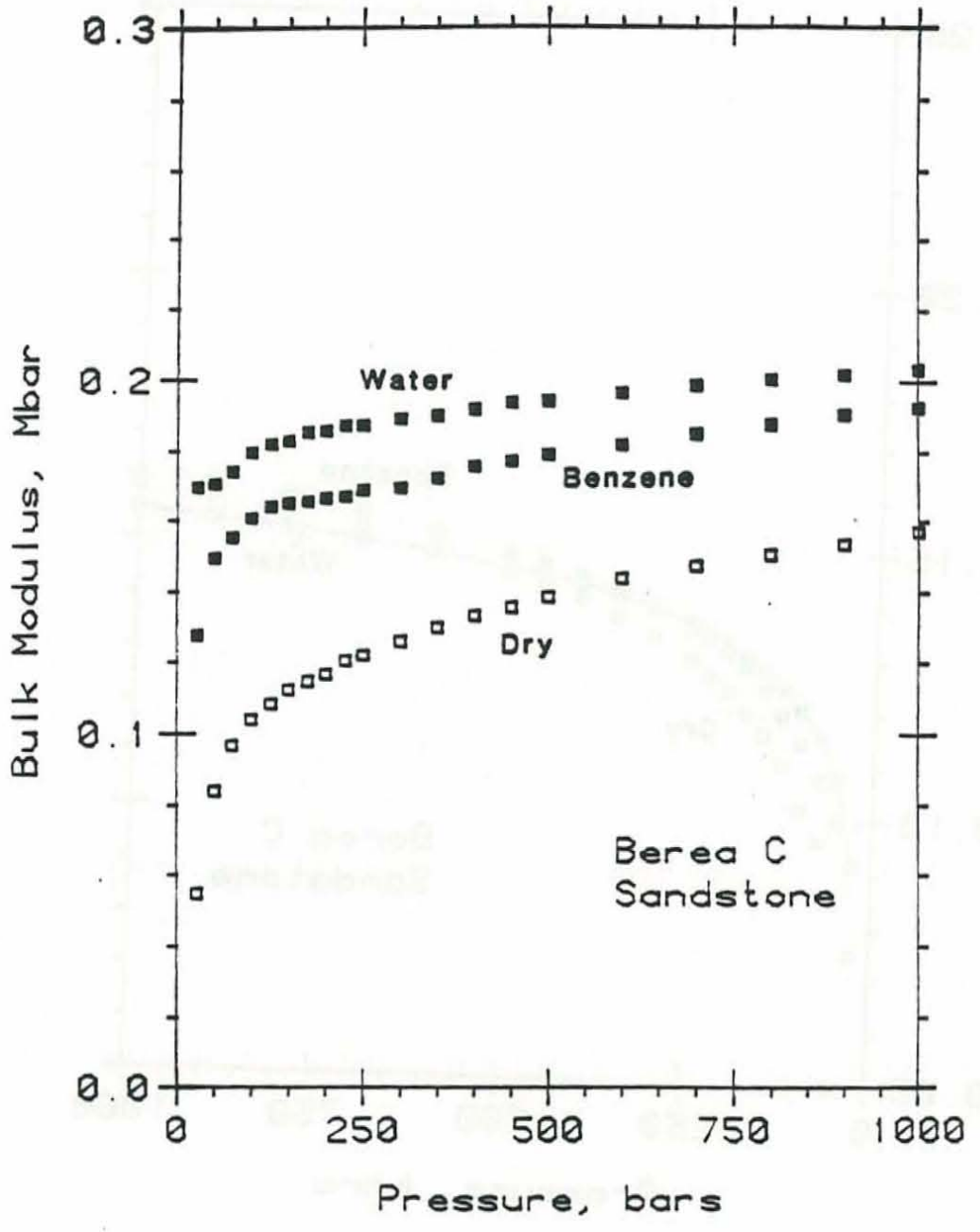

Figure 20. Vacuum dry, benzene-, and water-saturated bulk moduli for Berea sandstone as a function of differential pressure.

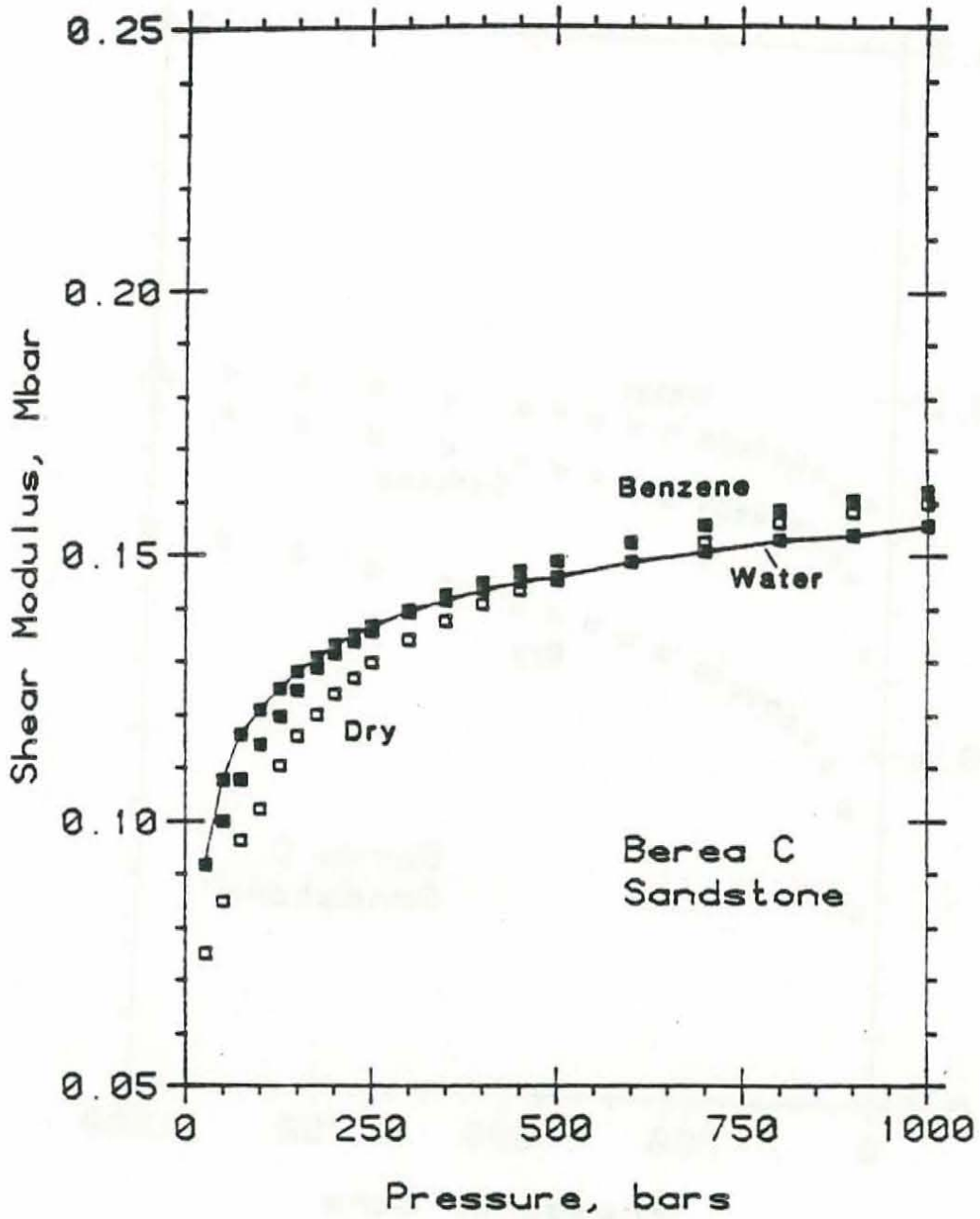

Figure 21. Vacuum dry, benzene-, and water-saturated shear moduli for Berea sandstone as a function of differential pressure.

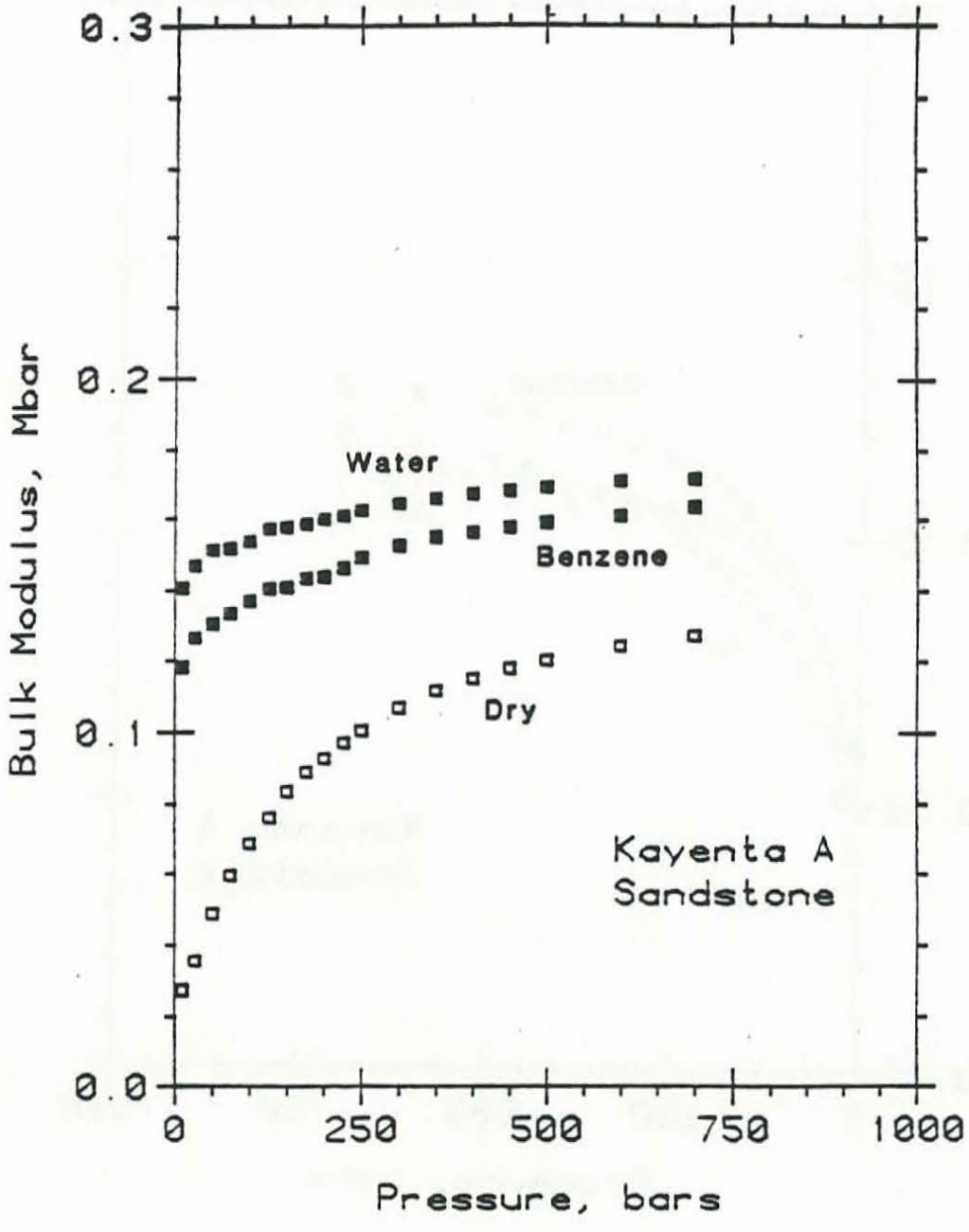

Figure 22. Vacuum dry, benzene-, and water-saturated bulk moduli for Kayenta sandstone as a function of differential pressure.

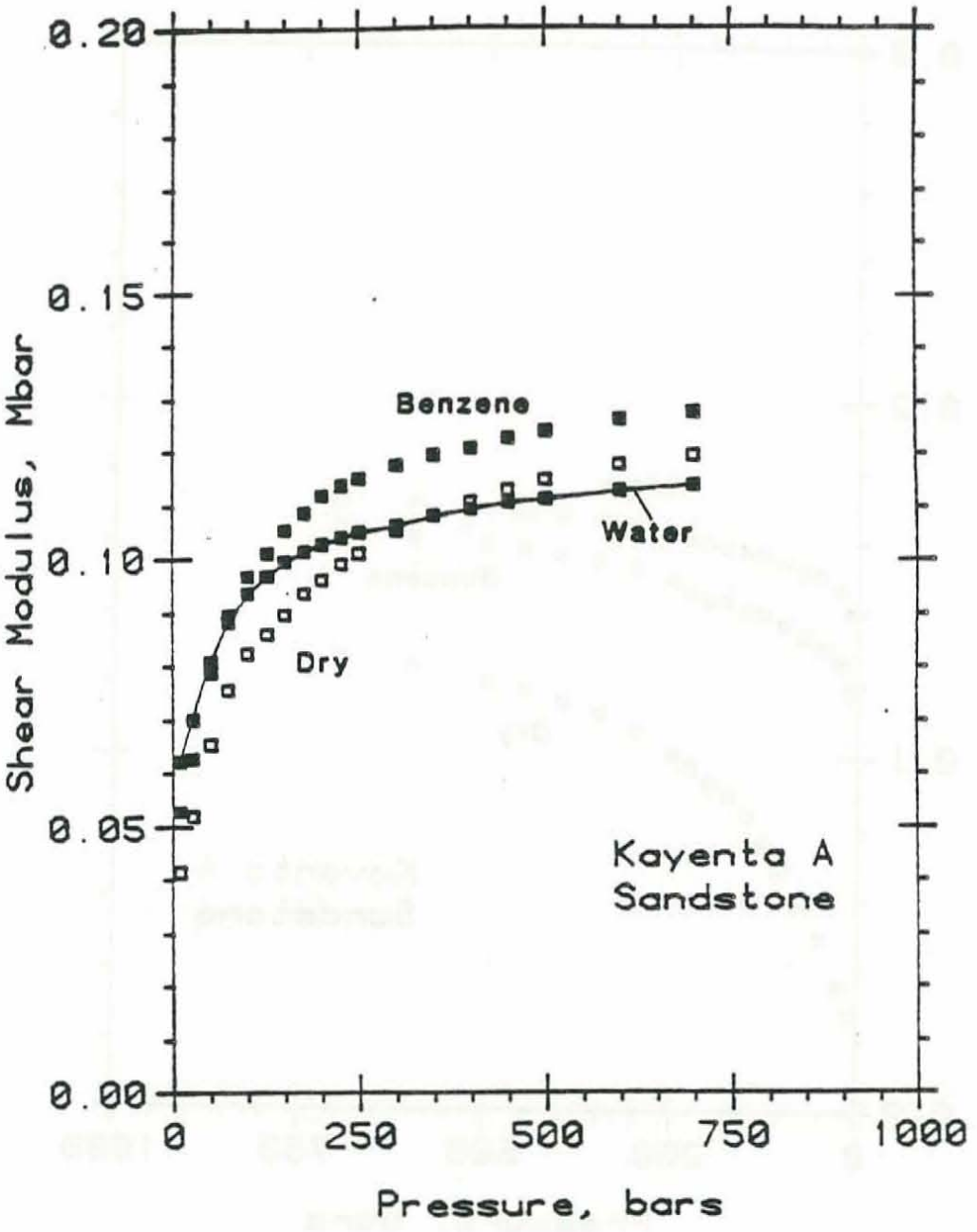

Figure 23. Vacuum dry, benzene-, and water-saturated shear moduli for Kayenta sandstone as a function of differential pressure.

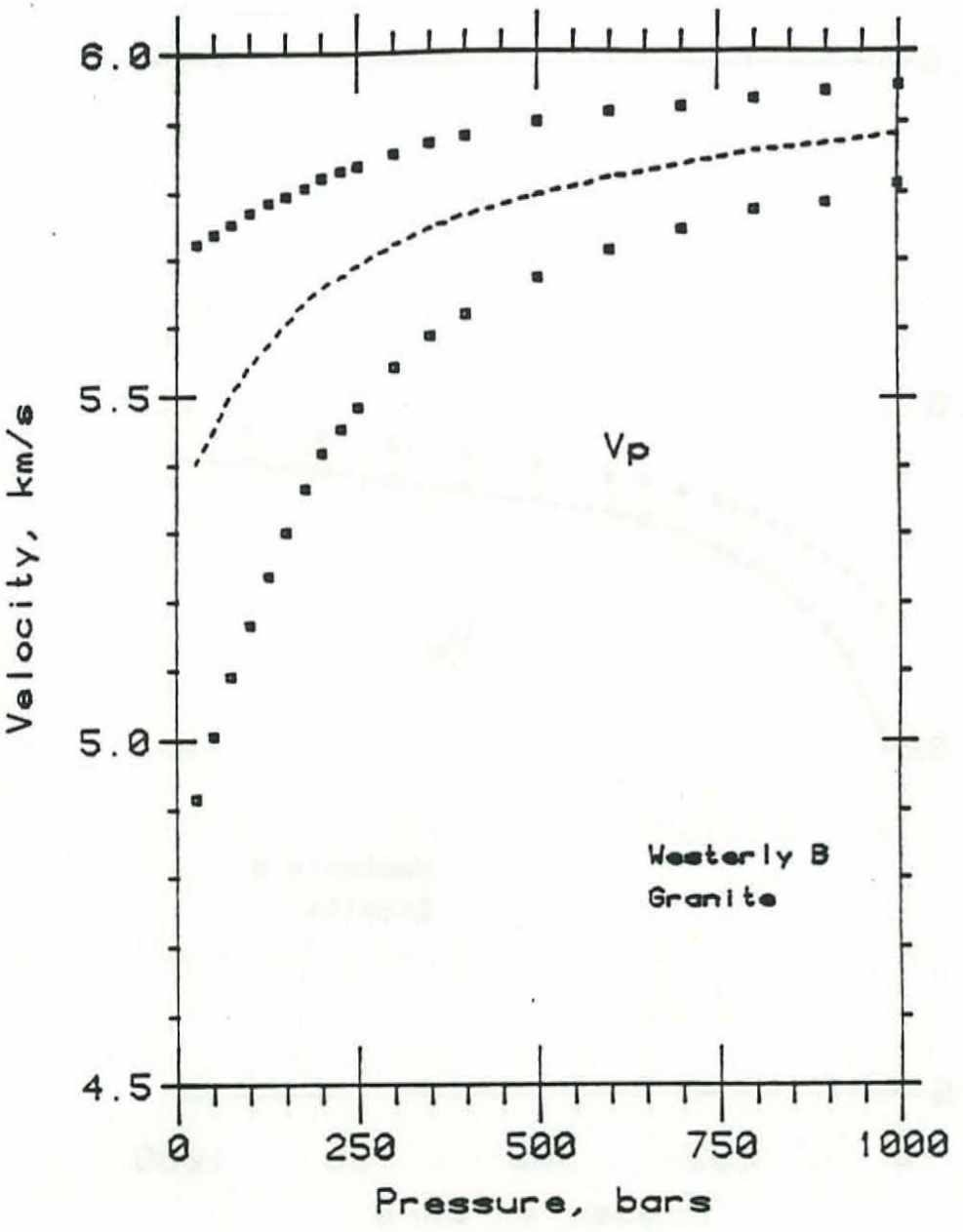

Figure 24. P-wave velocities for Westerly granite versus differential pressure for dry (open squares; 20 μm Hg vacuum) and benzene (solid squares; 100 bars pore pressure) saturations. Dashed line represents saturated P-wave velocities predicted from dry velocities (dry bulk and shear moduli) using Gassmann's equation for effective bulk modulus and the saturated bulk density.

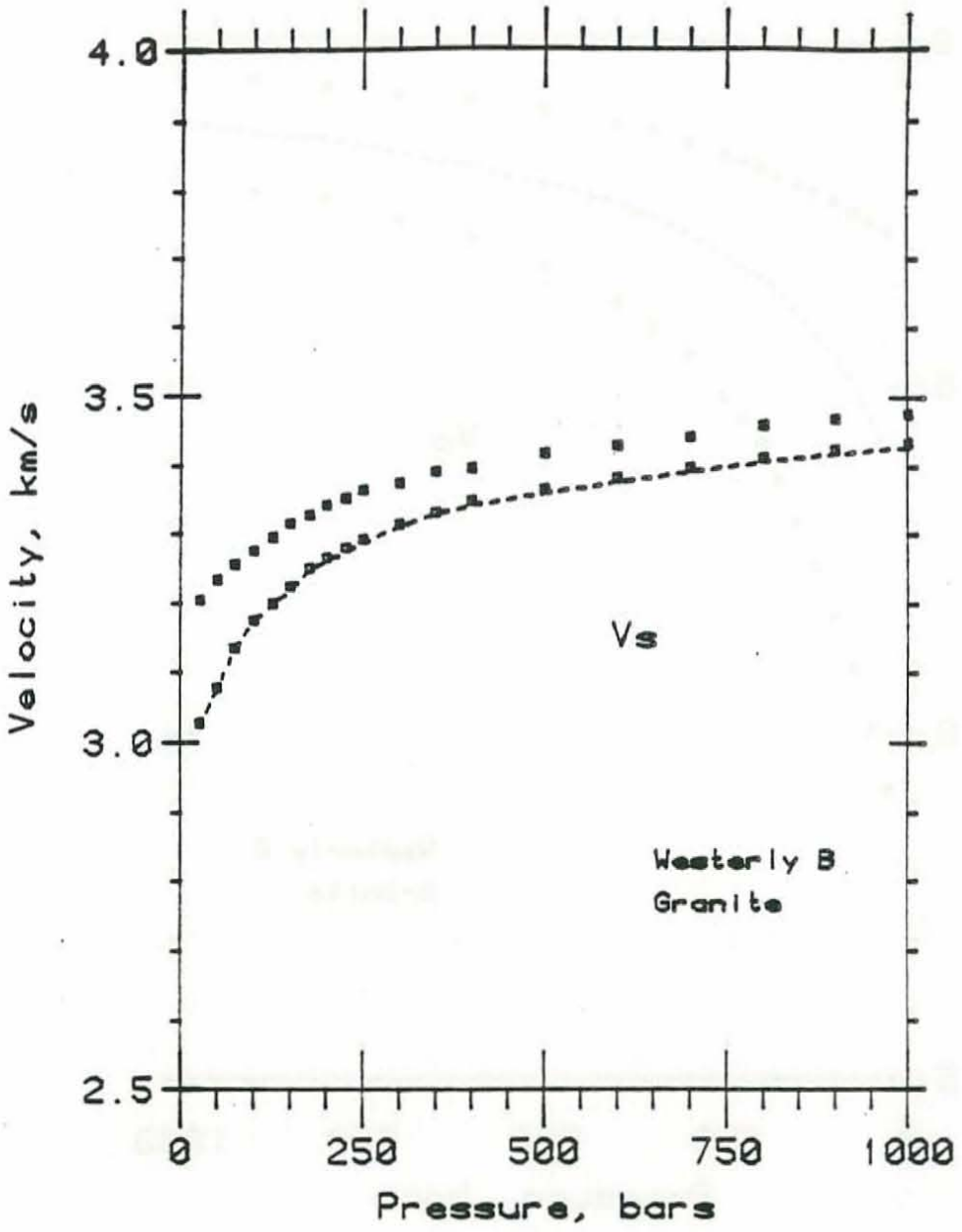

Figure 25. S-wave velocities for Westerly granite versus differential pressure for dry (open squares; 20 μm Hg vacuum) and benzene (solid squares; 100 bars pore pressure) saturations. Dashed line represents saturated S-wave velocities predicted from dry velocities (dry shear moduli) using the saturated bulk density.

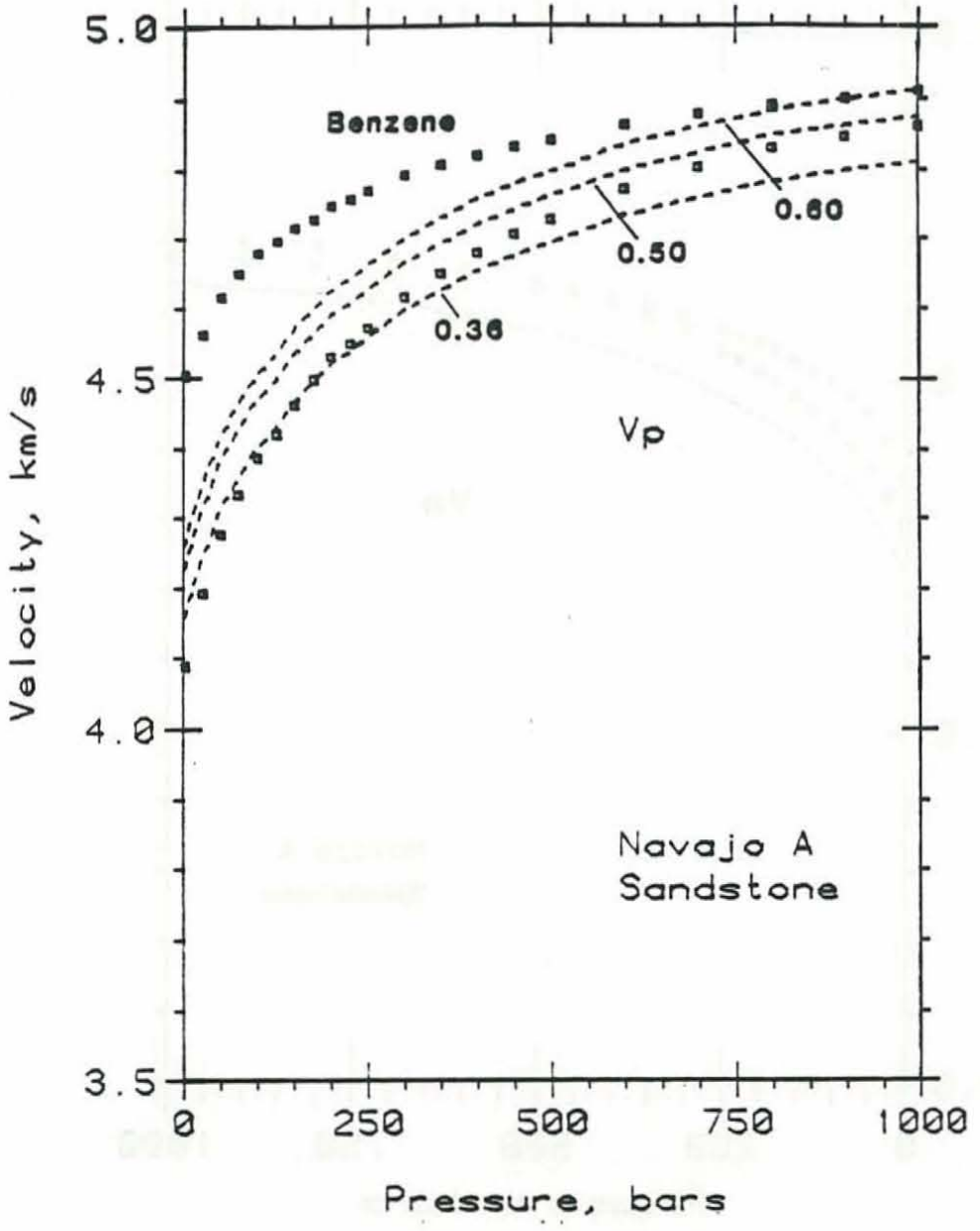

Figure 26. P-wave velocities for Navajo sandstone versus differential pressure for dry (open squares; 20 μm Hg vacuum) and benzene (solid squares; 100 bars pore pressure) saturations. Dashed lines represent saturated P-wave velocities predicted from dry velocities (dry bulk and shear moduli) using Gassmann's equation for effective bulk modulus and the saturated bulk density. Different dashed lines correspond to different intrinsic bulk moduli, K_s, in units of Mb, as indicated; K_s=0.36 Mb was measured in an unjacketed stress-strain test.

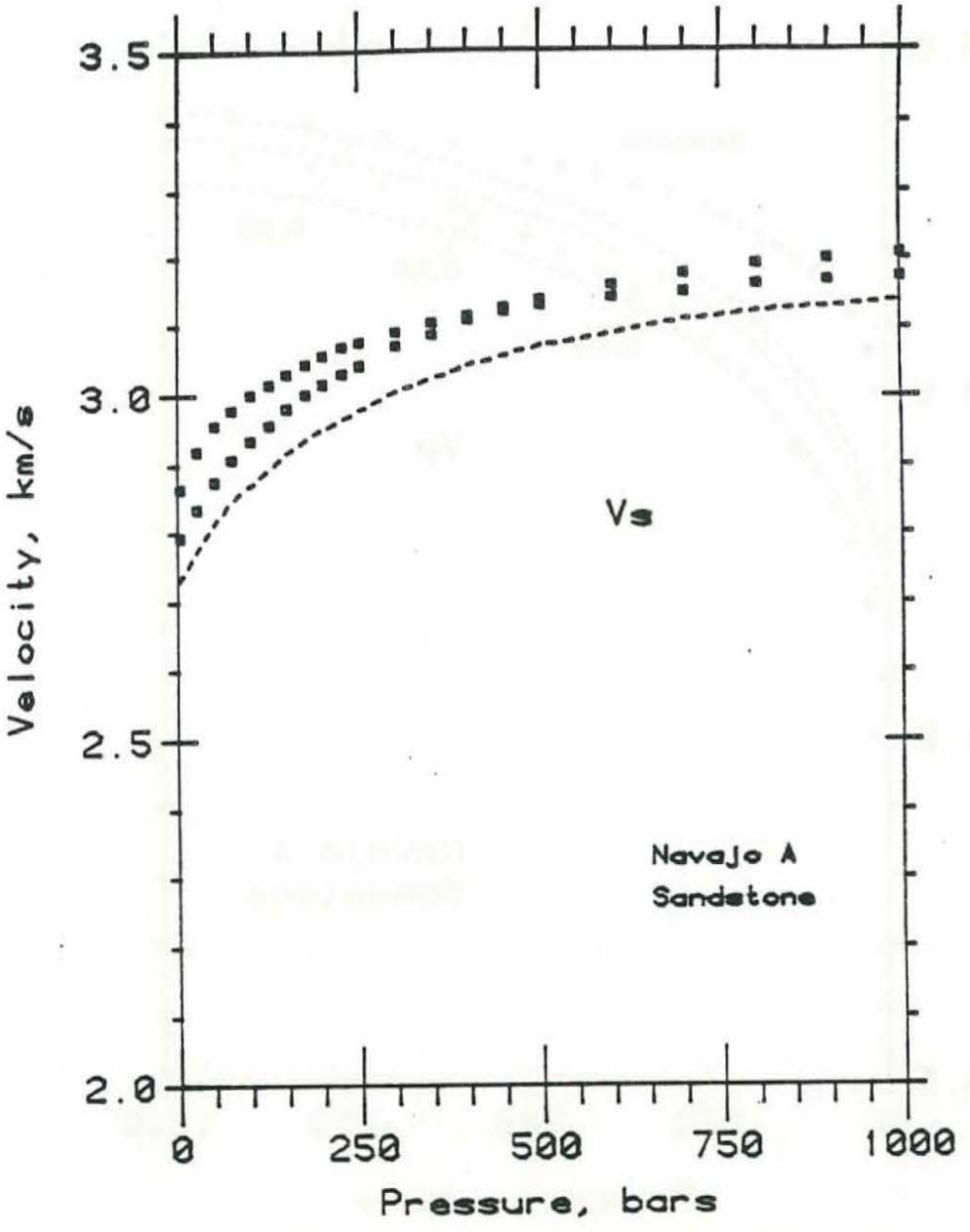

Figure 27. S-wave velocities for Navajo sandstone versus differential pressure for dry (open squares; 20 μm Hg vacuum) and benzene (solid squares; 100 bars pore pressure) saturations. Dashed line represents saturated S-wave velocities predicted from dry velocities (dry shear moduli) using the saturated bulk density.

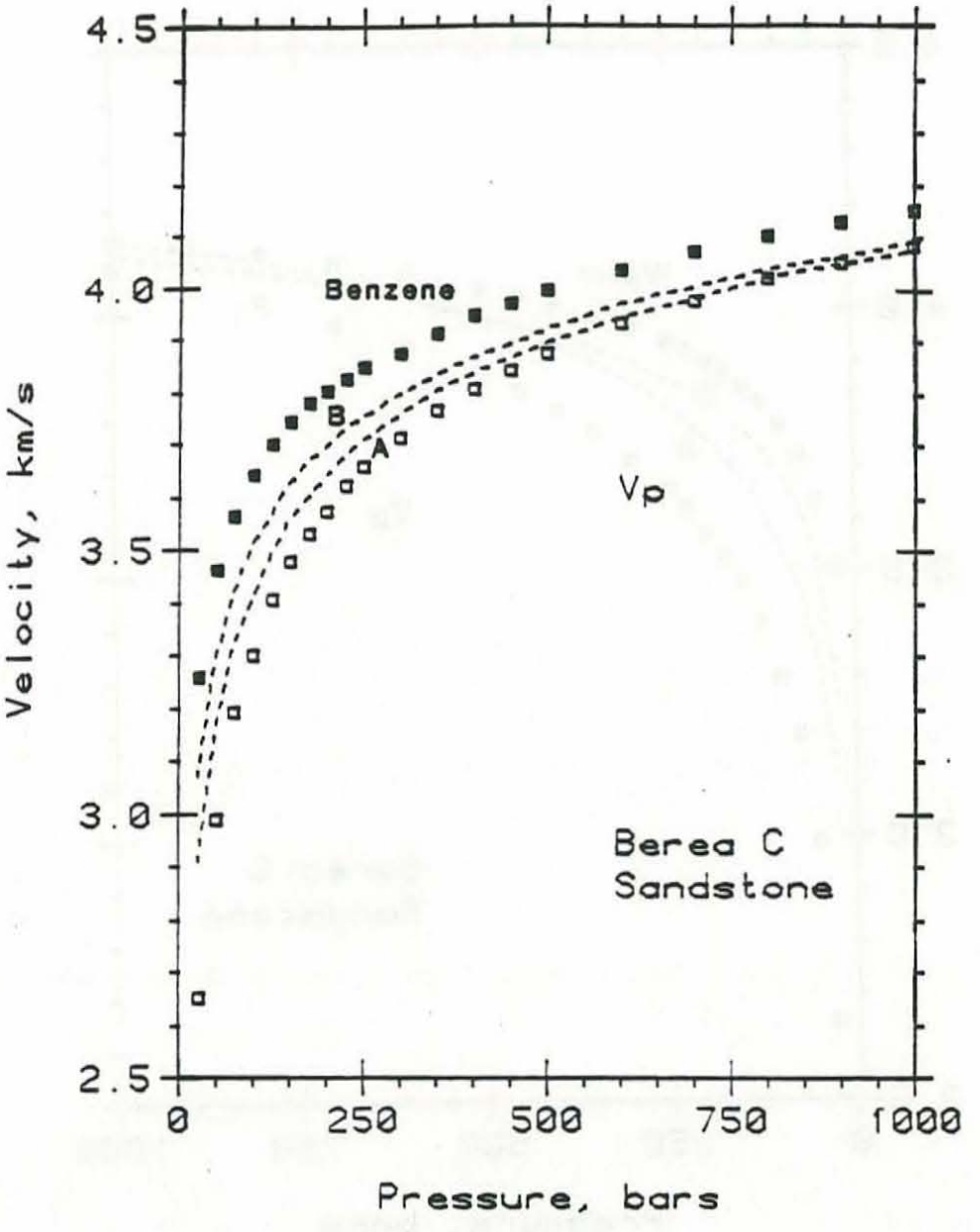

Figure 28. P-wave velocities for Berea sandstone versus differential pressure for dry (open squares; 20 μm Hg vacuum) and benzene (solid squares; 100 bars pore pressure) saturations. Dashed lines represent saturated P-wave velocities predicted from: A) dry velocities (dry bulk and shear moduli), and B) dry and saturated velocities (dry bulk moduli and benzene saturated shear moduli) using Gassmann's equation for effective bulk modulus and the saturated bulk density.

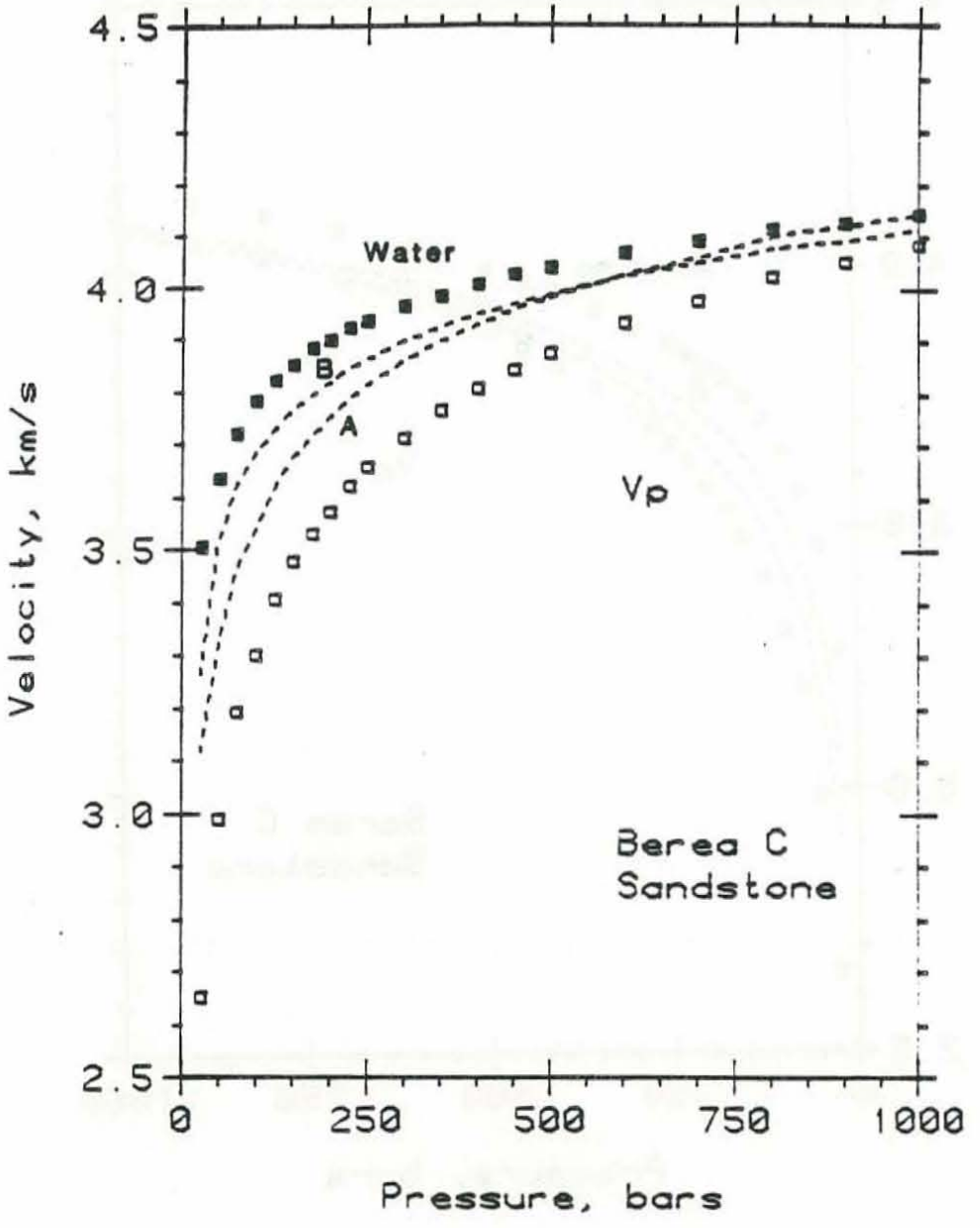

Figure 29. P-wave velocities for Berea sandstone versus differential pressure for dry (open squares; 20 μm Hg vacuum) and water (solid squares; 100 bars pore pressure) saturations. Dashed lines represent saturated P-wave velocities predicted from: A) dry velocities (dry bulk and shear moduli), and B) dry and saturated velocities (dry bulk moduli and water saturated shear moduli) using Gassmann's equation for effective bulk modulus and the saturated bulk density.

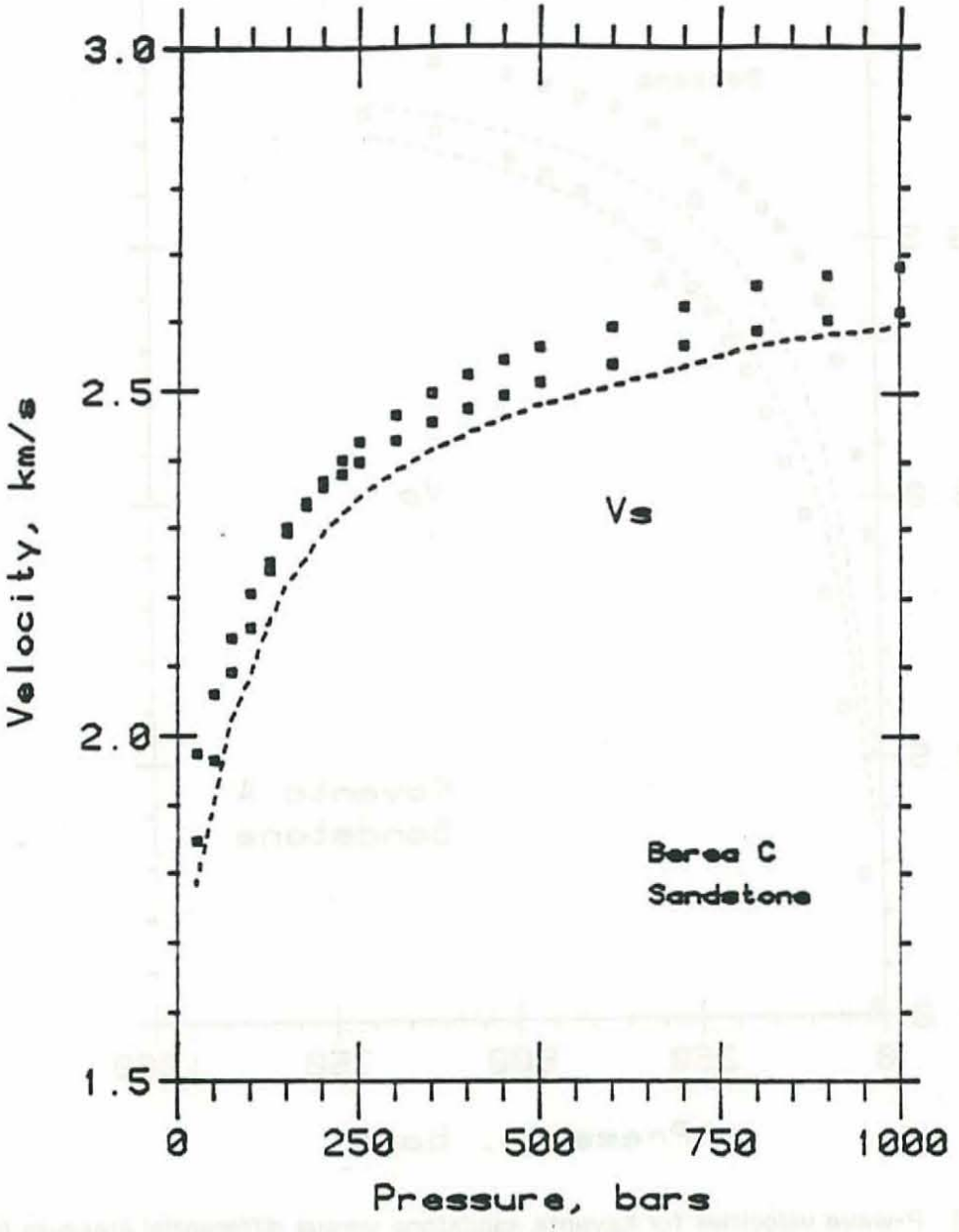

Figure 30. S-wave velocities for Berea sandstone versus differential pressure for dry (open squares; 20 μm Hg vacuum) and benzene (solid squares; 100 bars pore pressure) saturations. Dashed line represents saturated S-wave velocities predicted from dry velocities (dry shear moduli) using the saturated bulk density.

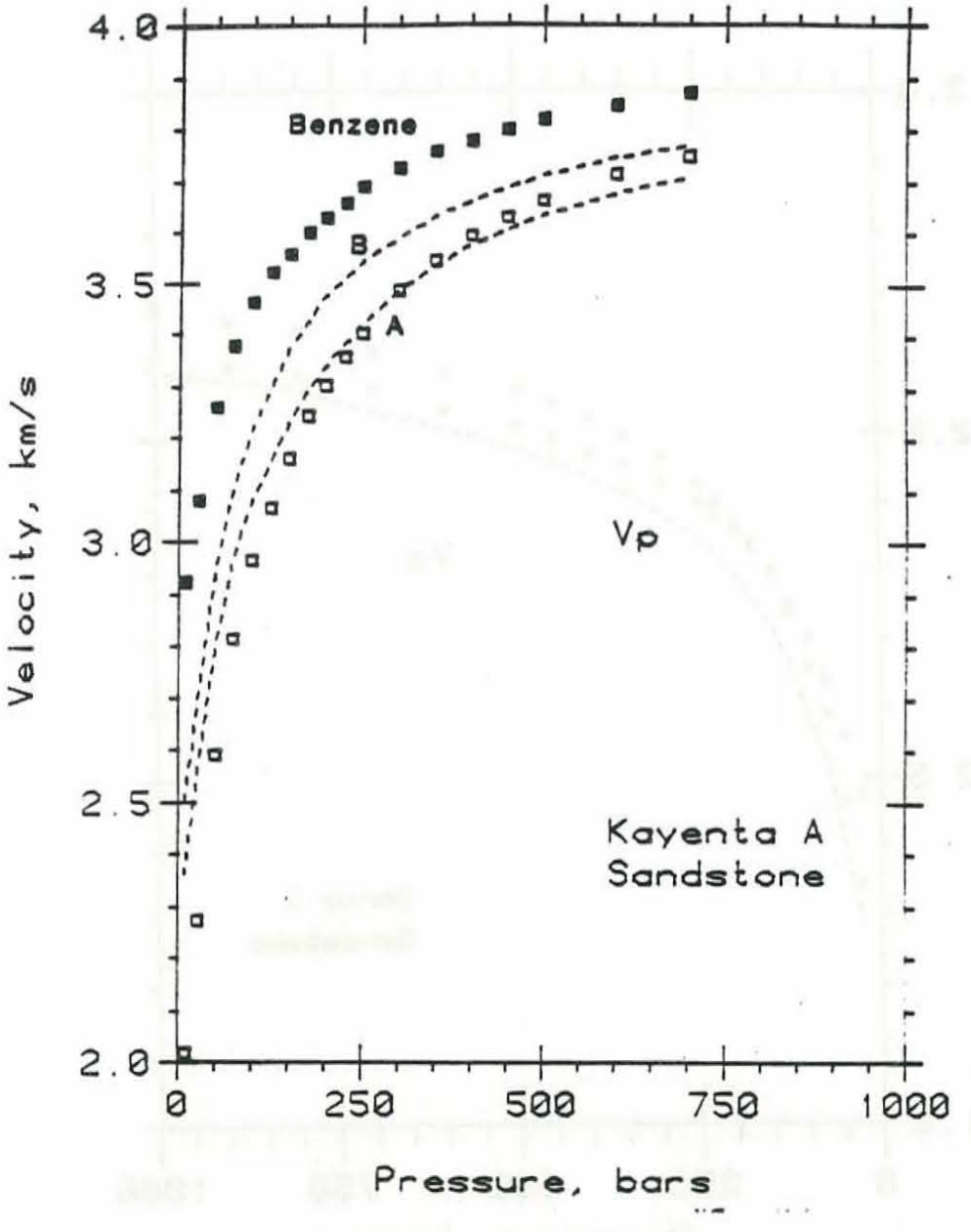

Figure 31. P-wave velocities for Kayenta sandstone versus differential pressure for dry (open squares; 20 μm Hg vacuum) and benzene (solid squares; 100 bars pore pressure) saturations. Dashed lines represent saturated P-wave velocities predicted from: A) dry velocities (dry bulk and shear moduli), and B) dry and saturated velocities (dry bulk moduli and saturated shear moduli) using Gassmann's equation for effective bulk modulus and the saturated bulk density.

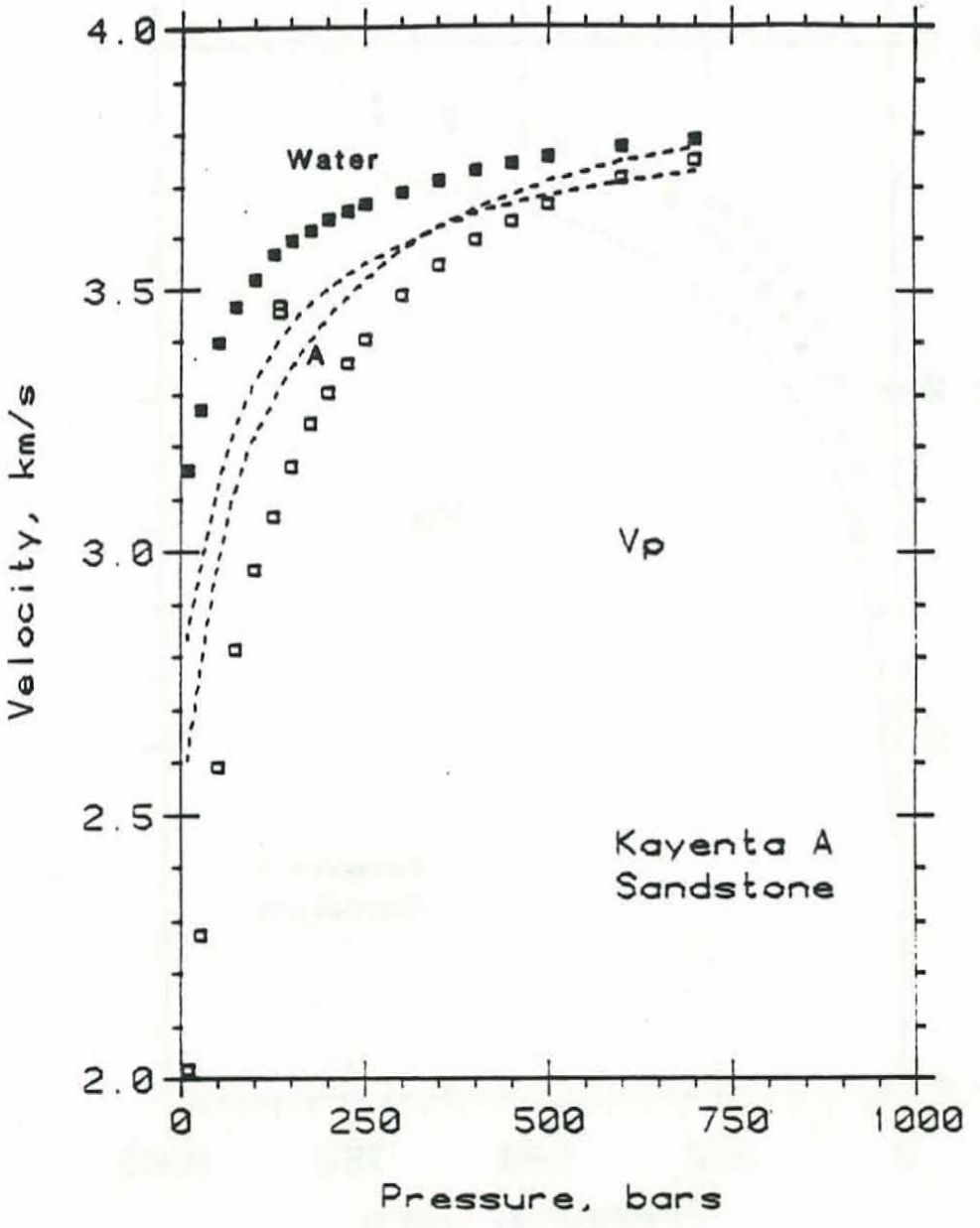

Figure 32. P-wave velocities for Kayenta sandstone versus differential pressure for dry (open squares; 20 μm Hg vacuum) and water (solid squares; 100 bars pore pressure) saturations. Dashed lines represent saturated P-wave velocities predicted from: A) dry velocities (dry bulk and shear moduli), and B) dry and saturated velocities (dry bulk moduli and saturated shear moduli) using Gassmann's equation for effective bulk modulus and the saturated bulk density.

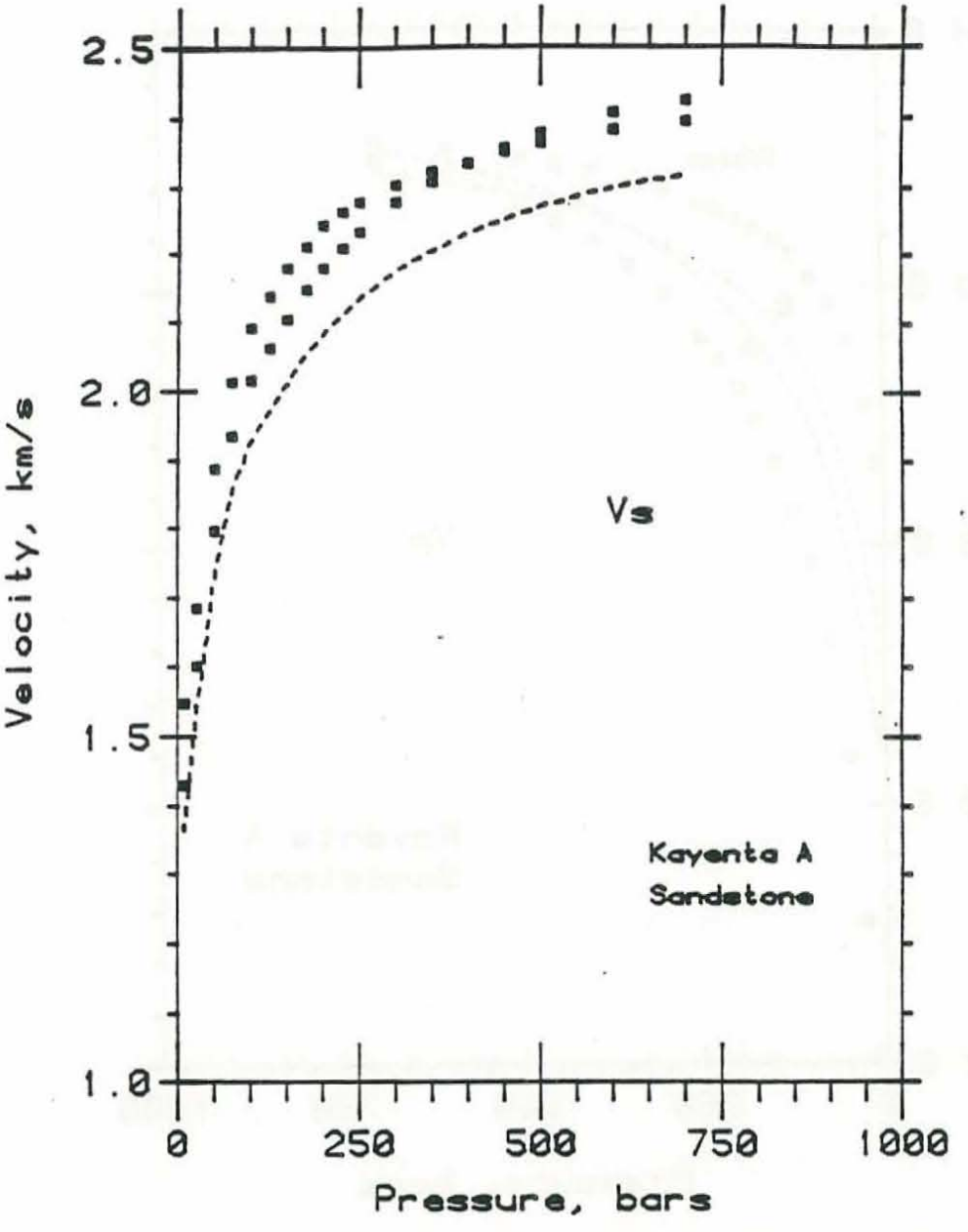

Figure 33. S-wave velocities for Kayenta sandstone versus differential pressure for dry (open squares; 20 μm Hg vacuum) and benzene (solid squares; 100 bars pore pressure) saturations. Dashed line represents saturated velocities predicted from dry velocities using the saturated bulk density.

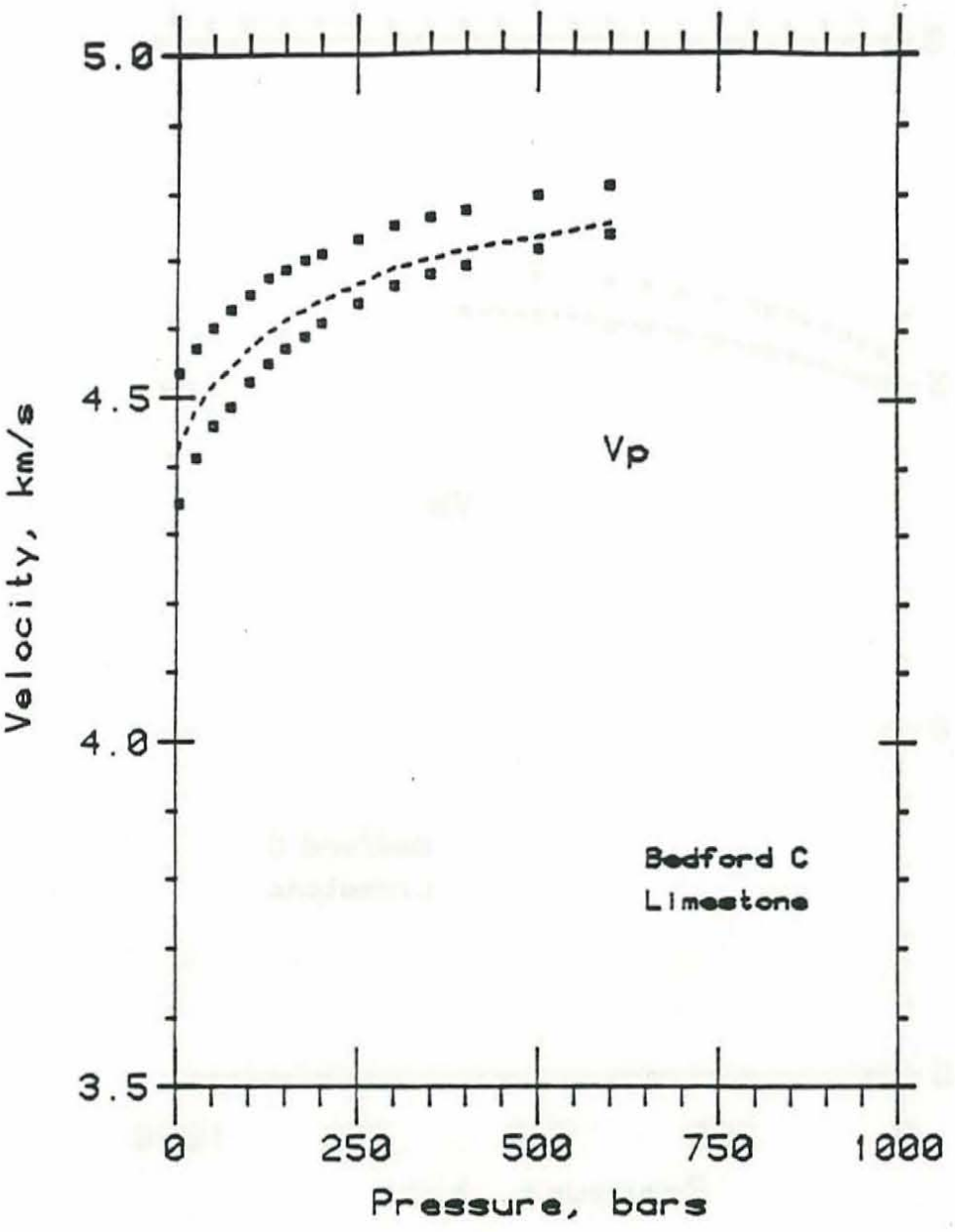

Figure 34. P-wave velocities for Bedford limestone versus differential pressure for dry (open squares; 20 μm Hg vacuum) and benzene (solid squares; 100 bars pore pressure) saturations. Dashed line represents saturated velocities predicted from dry velocities using Gassmann's equation for effective bulk modulus and the saturated bulk density.

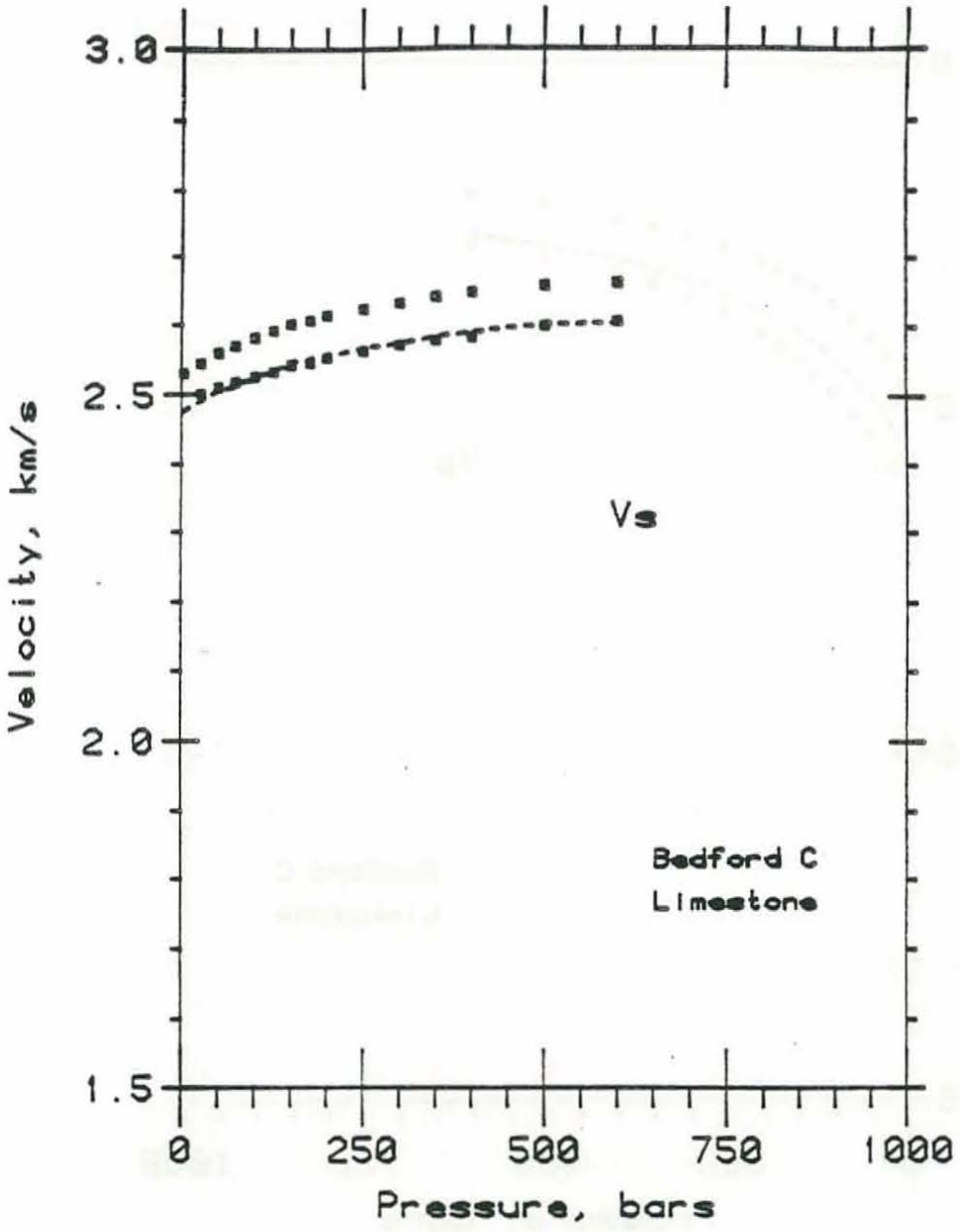

Figure 35. S-wave velocities for Bedford limestone versus differential pressure for dry (open squares; 20 μm Hg vacuum) and benzene (solid squares; 100 bars pore pressure) saturations. Dashed line represents saturated velocities predicted from dry velocities using the saturated bulk density.

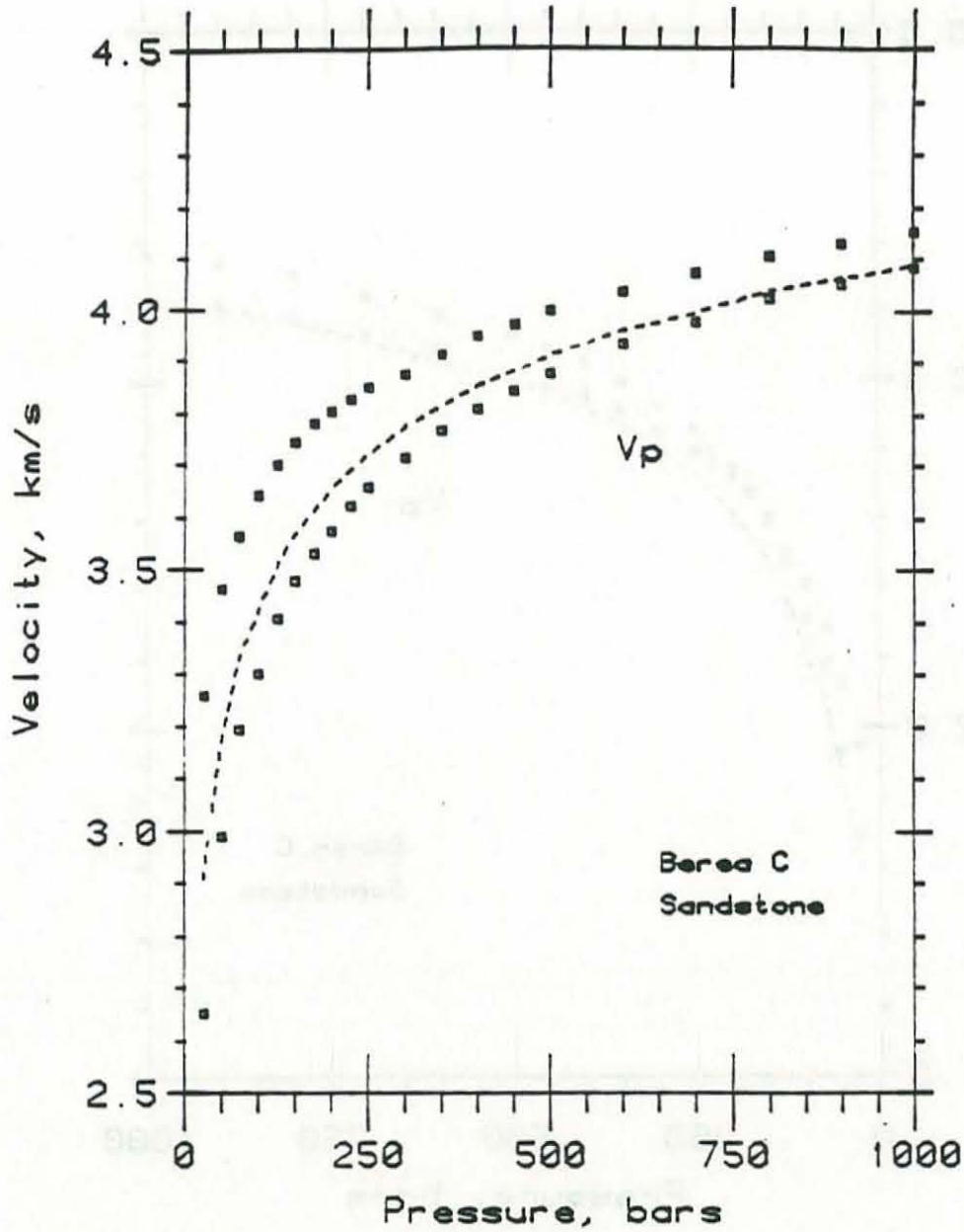

Figure 36. P-wave velocities for Berea sandstone versus differential pressure for dry (open squares; 20 μm Hg vacuum) and benzene (solid squares; 100 bars pore pressure) saturations. Dashed line represents saturated velocities predicted from dry velocities using the Biot inertial formulations with a geometrical factor α=4.4.

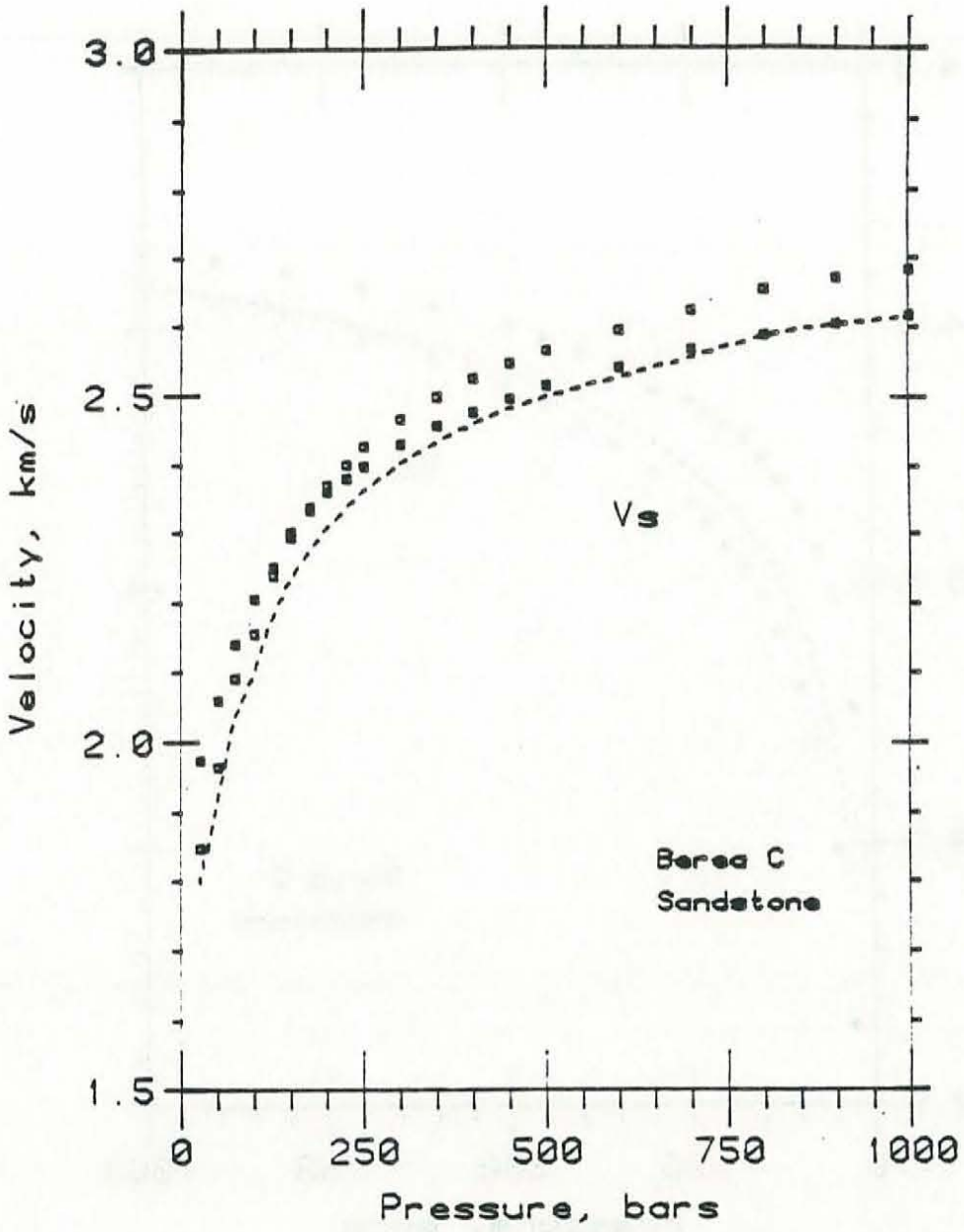

Figure 37. S-wave velocities for Berea sandstone versus differential pressure for dry (open squares; 20 μm Hg vacuum) and benzene (solid squares; 100 bars pore pressure) saturations. Dashed line represents saturated velocities predicted from dry velocities using the Biot inertial formulations with a geometrical factor α=4.4.

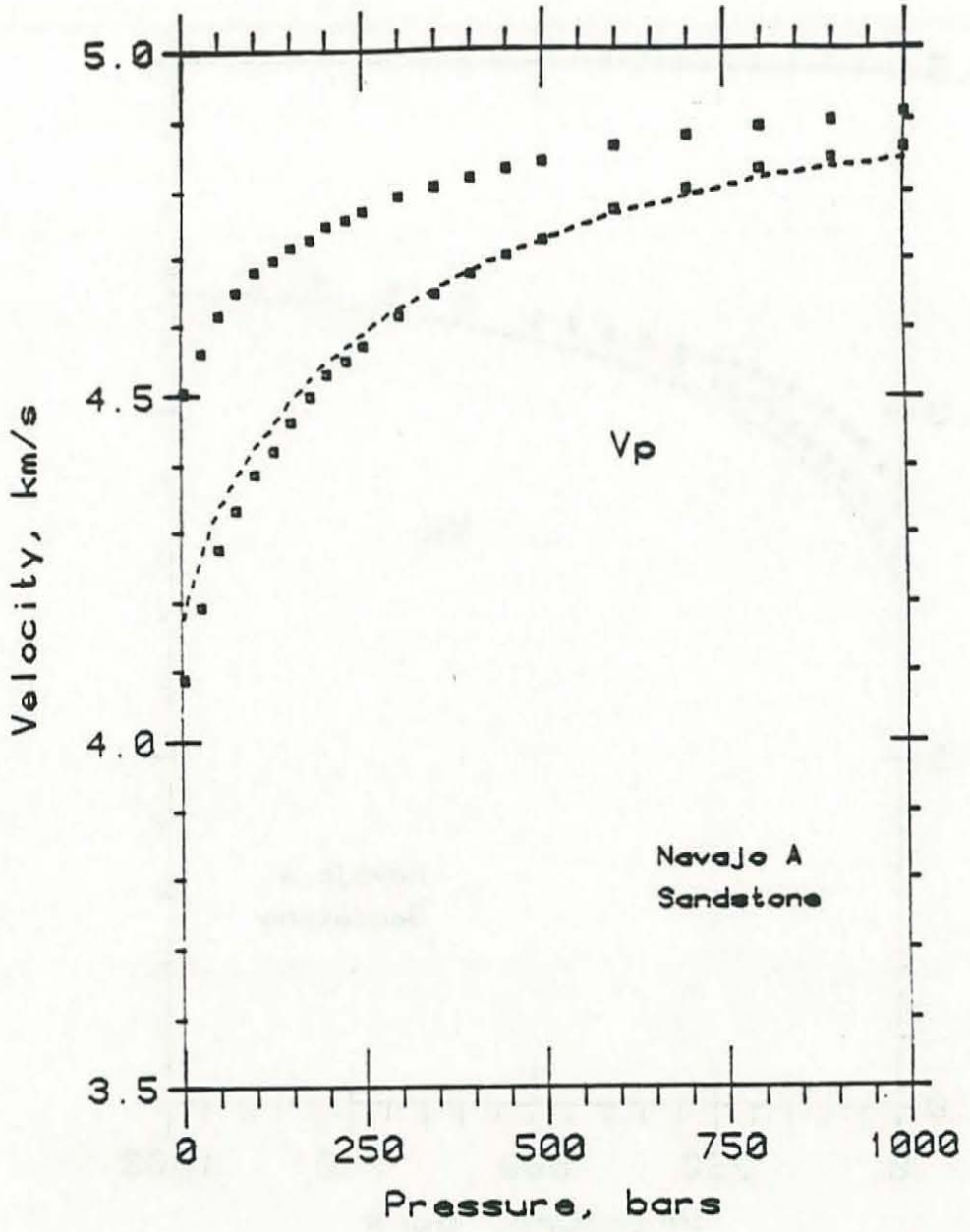

Figure 38. P-wave velocities for Navajo sandstone versus differential pressure for dry (open squares; 20 μm Hg vacuum) and benzene (solid squares; 100 bars pore pressure) saturations. Dashed line represents saturated velocities predicted from dry velocities using the Biot inertial formulations with a geometrical factor α=2.1.

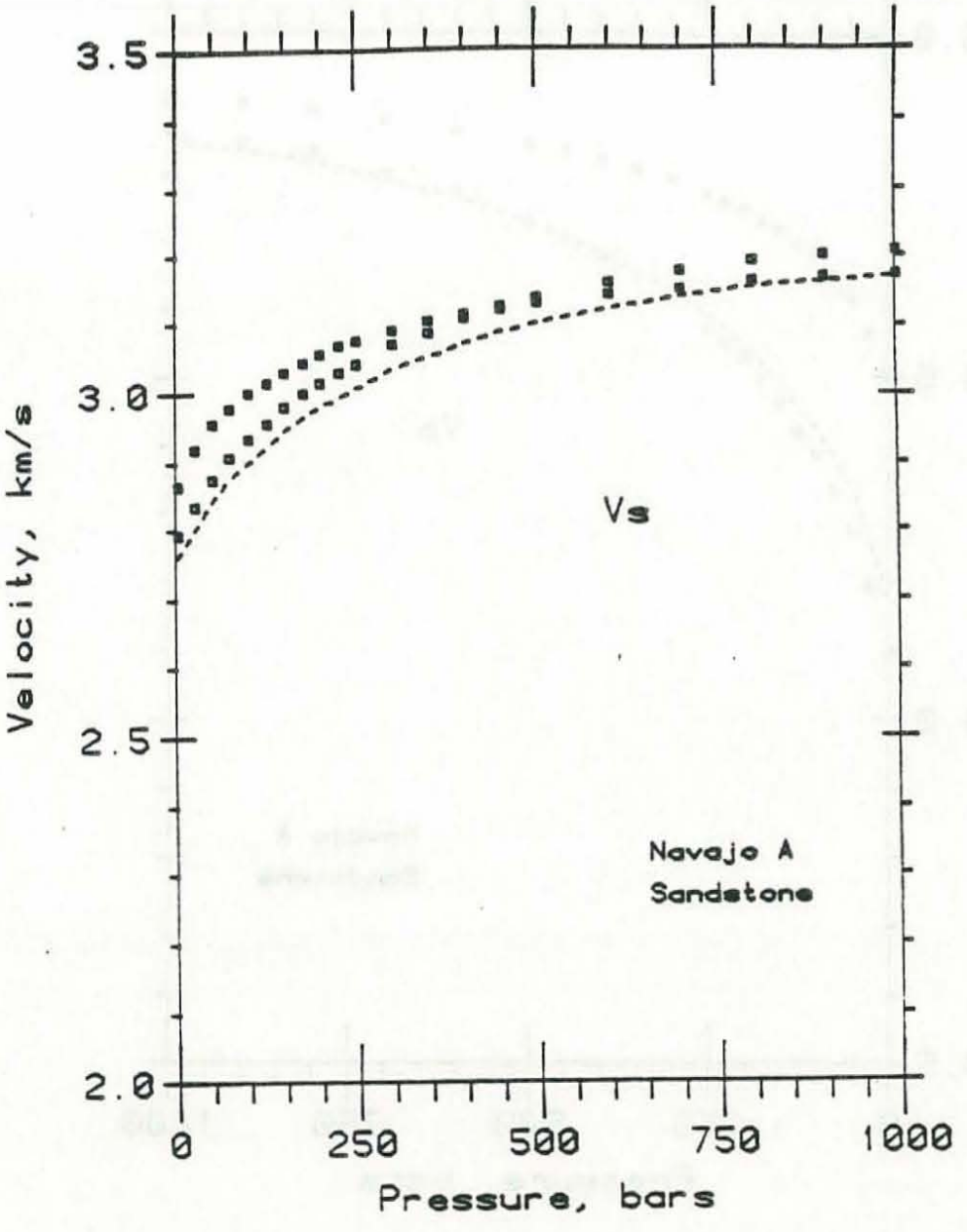

Figure 39. S-wave velocities for Navajo sandstone versus differential pressure for dry (open squares; 20 μm Hg vacuum) and benzene (solid squares; 100 bars pore pressure) saturations. Dashed line represents saturated velocities predicted from dry velocities using the Biot inertial formulations with a geometrical factor α=2.1.

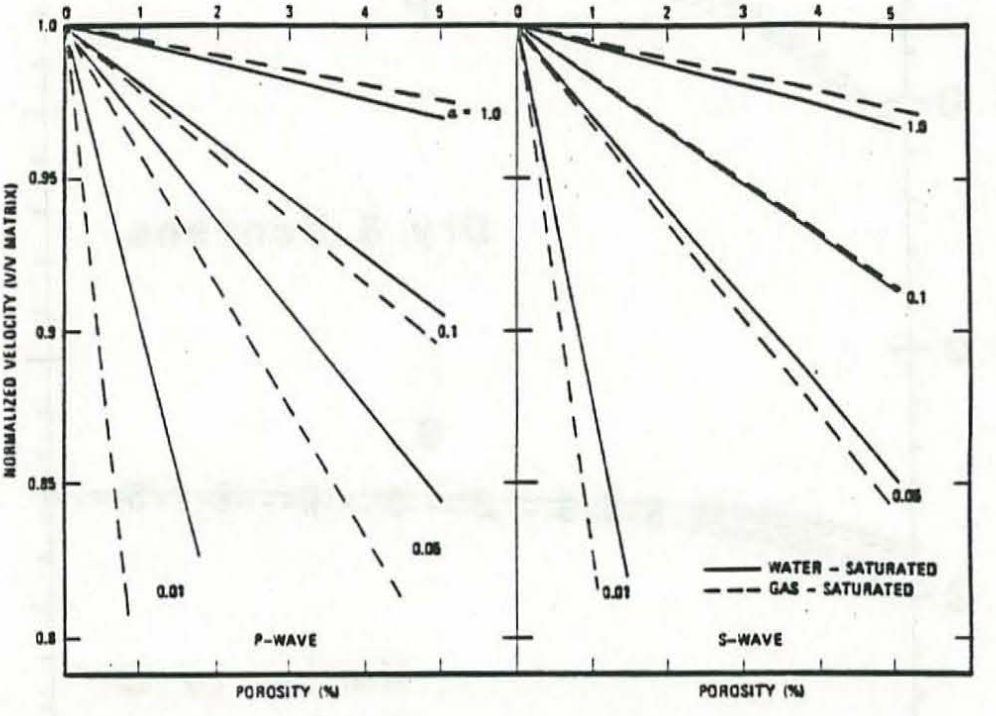

Figure 40. Normalized P- and S-wave velocities versus volume concentration of inclusions of different aspect ratios for water and gas saturated inclusions. After Toksöz et al. (1976).

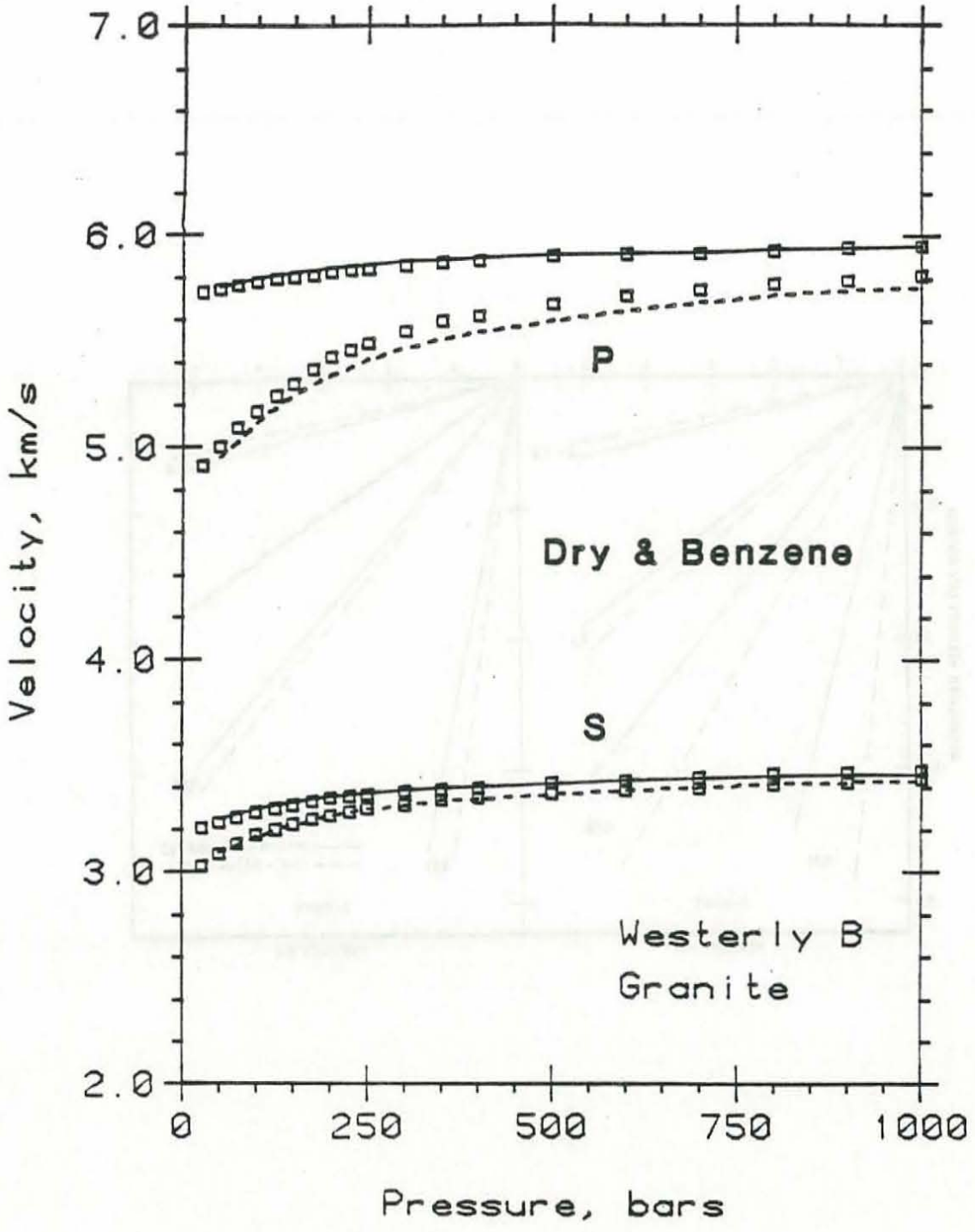

Figure 41. Measured dry (open squares) and benzene (solid squares) saturated P- and S-wave velocities for Westerly granite with results of inversion for pore aspect ratio spectra with the method of Cheng (1978) based on the model of Kuster and Toksöz (1974).

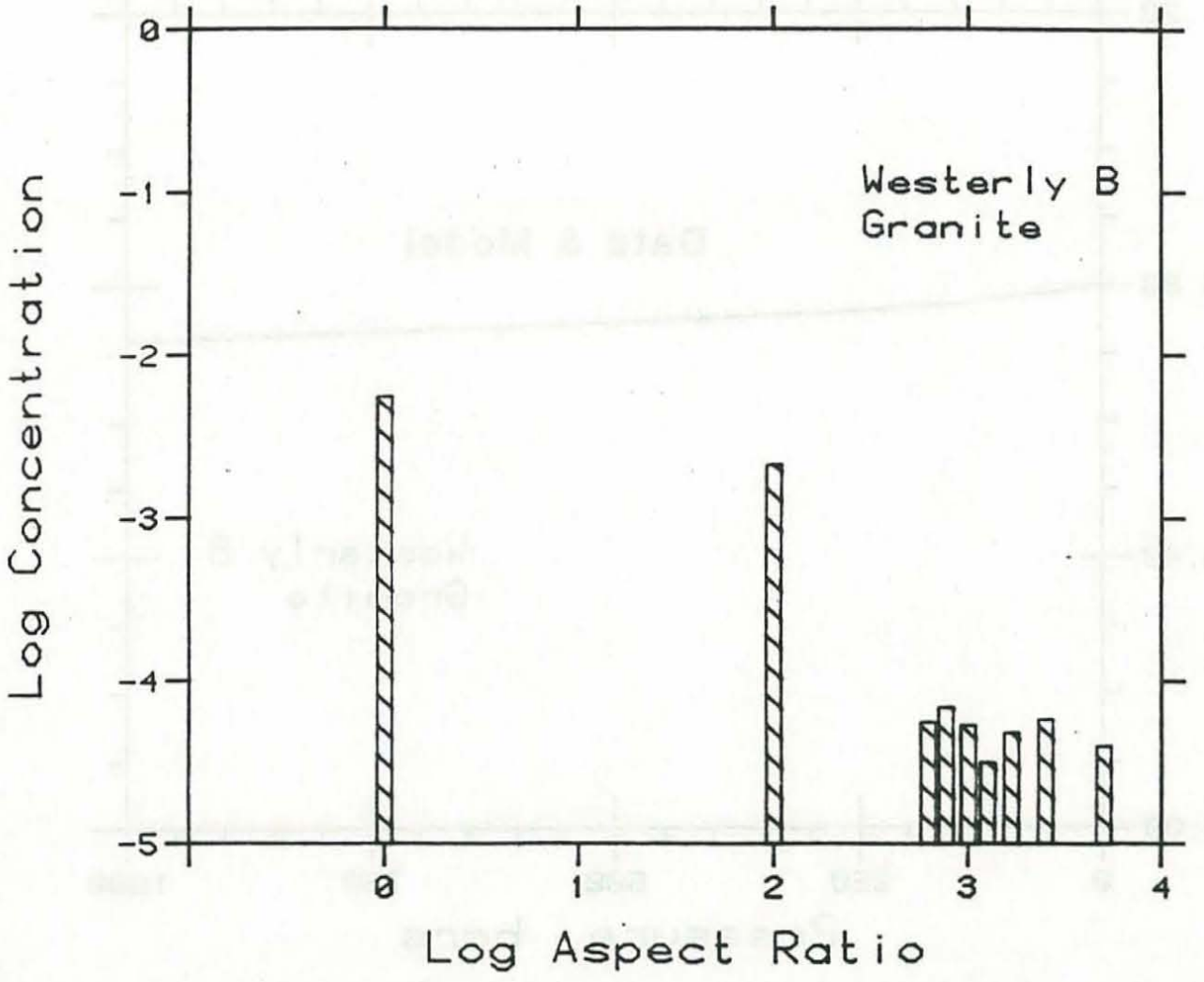

Figure 42. Pore aspect ratio distribution for Westerly granite at zero pressure based on inversion of dry and benzene saturated velocities.

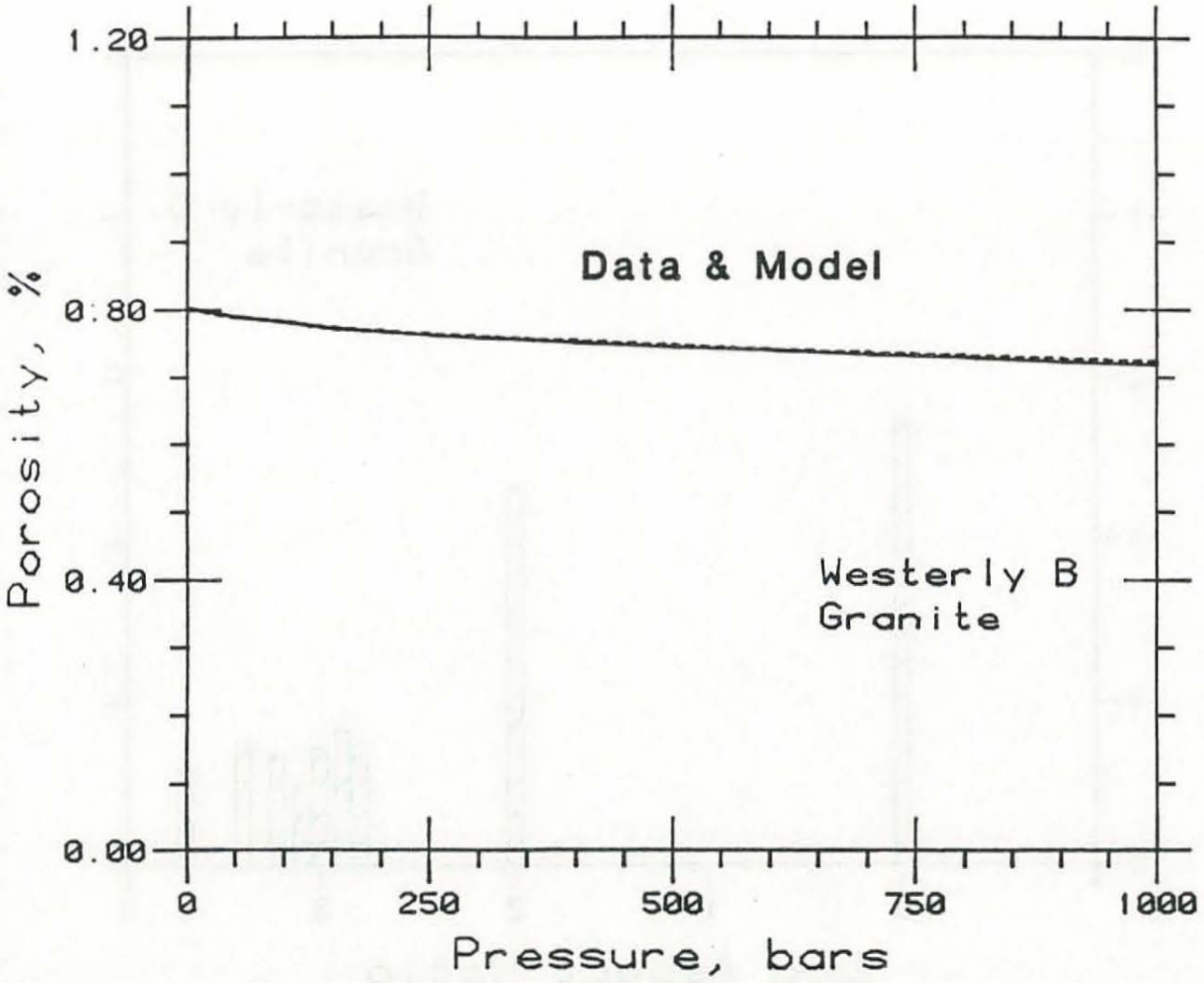

Figure 43. Measured porosity reduction versus confining pressure (solid line) for Westerly granite compared with that predicted by velocity inversion (dashed line).

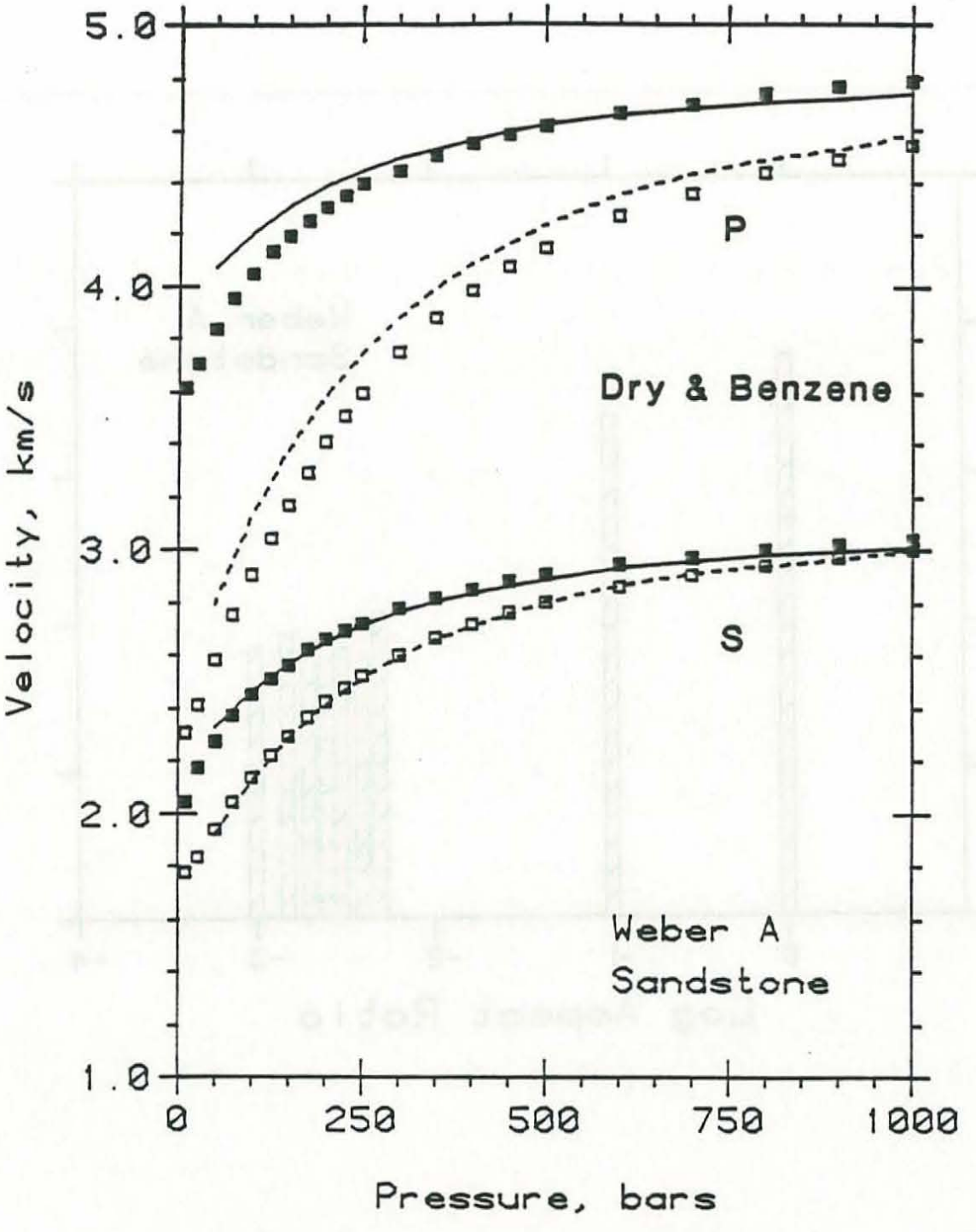

Figure 44. Measured dry (open squares) and benzene (solid squares) saturated P- and S-wave velocities for Weber sandstone with fitted dry (dashed line) and benzene (solid line) saturated velocities from inversion for pore aspect ratio spectra.

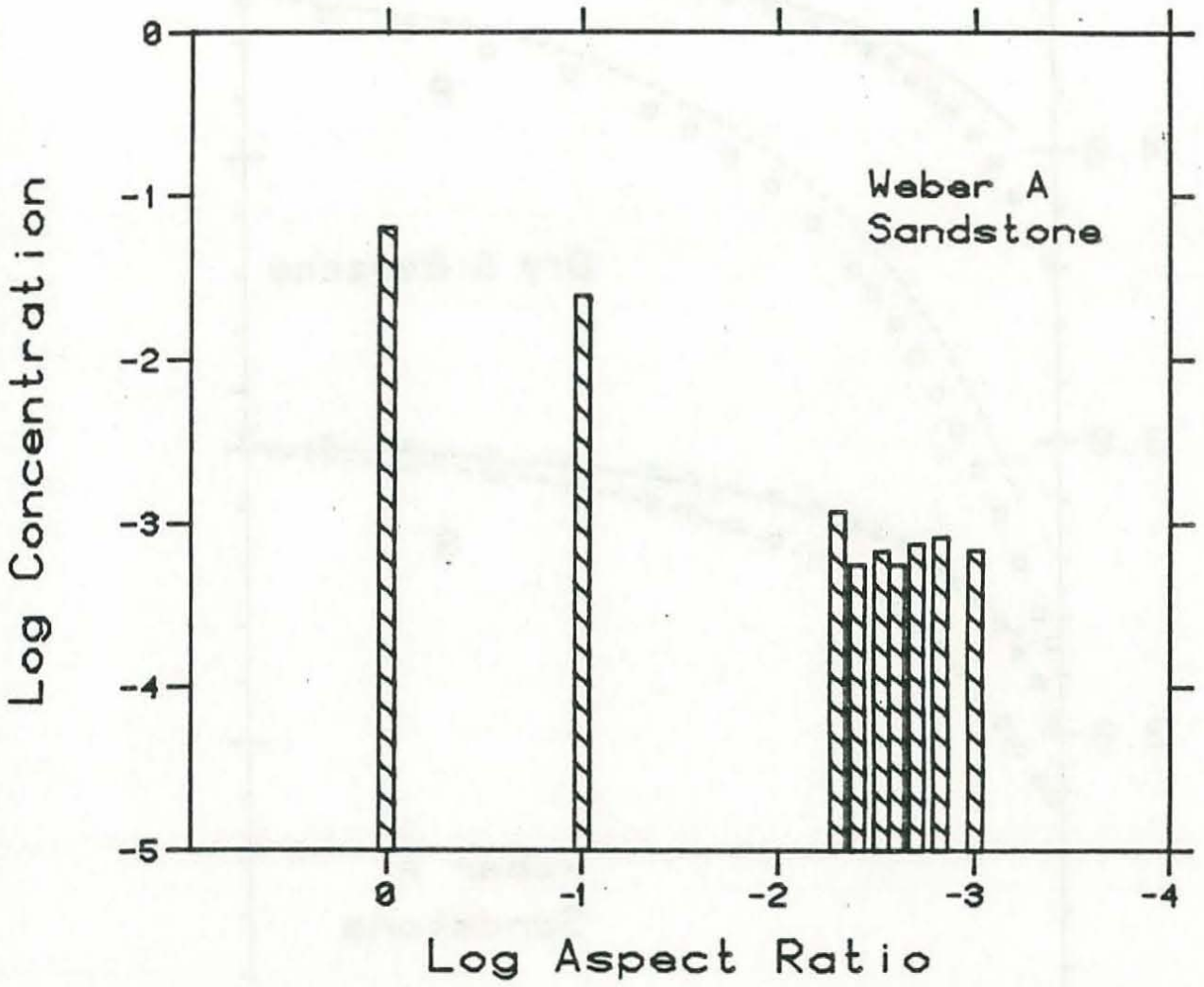

Figure 45. Pore aspect ratio distribution for Weber sandstone at zero pressure based on inversion of dry and benzene saturated velocities.

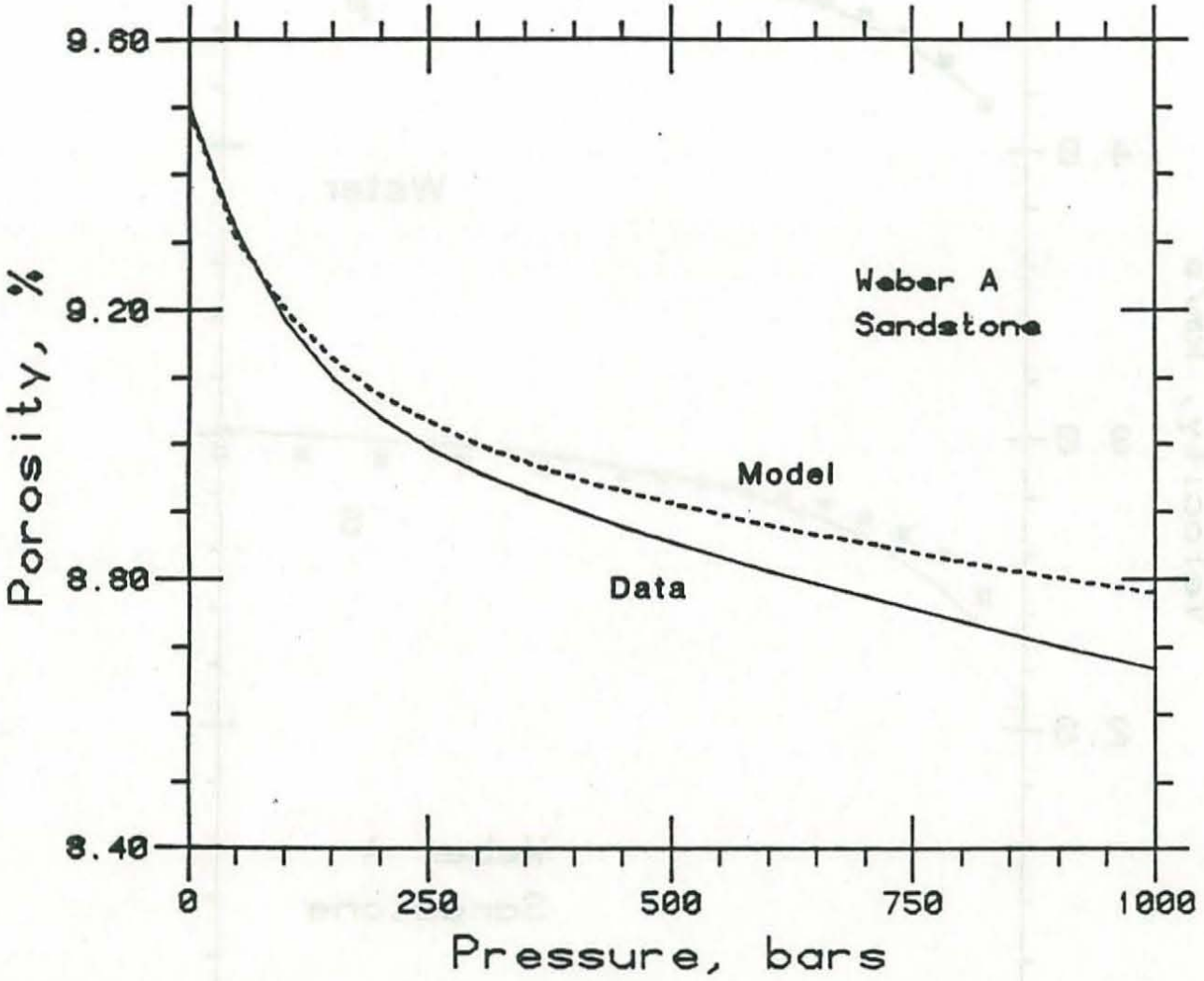

Figure 46. Measured porosity reduction versus confining pressure (solid line) for Weber sandstone compared with that predicted by velocity inversion (dashed line).

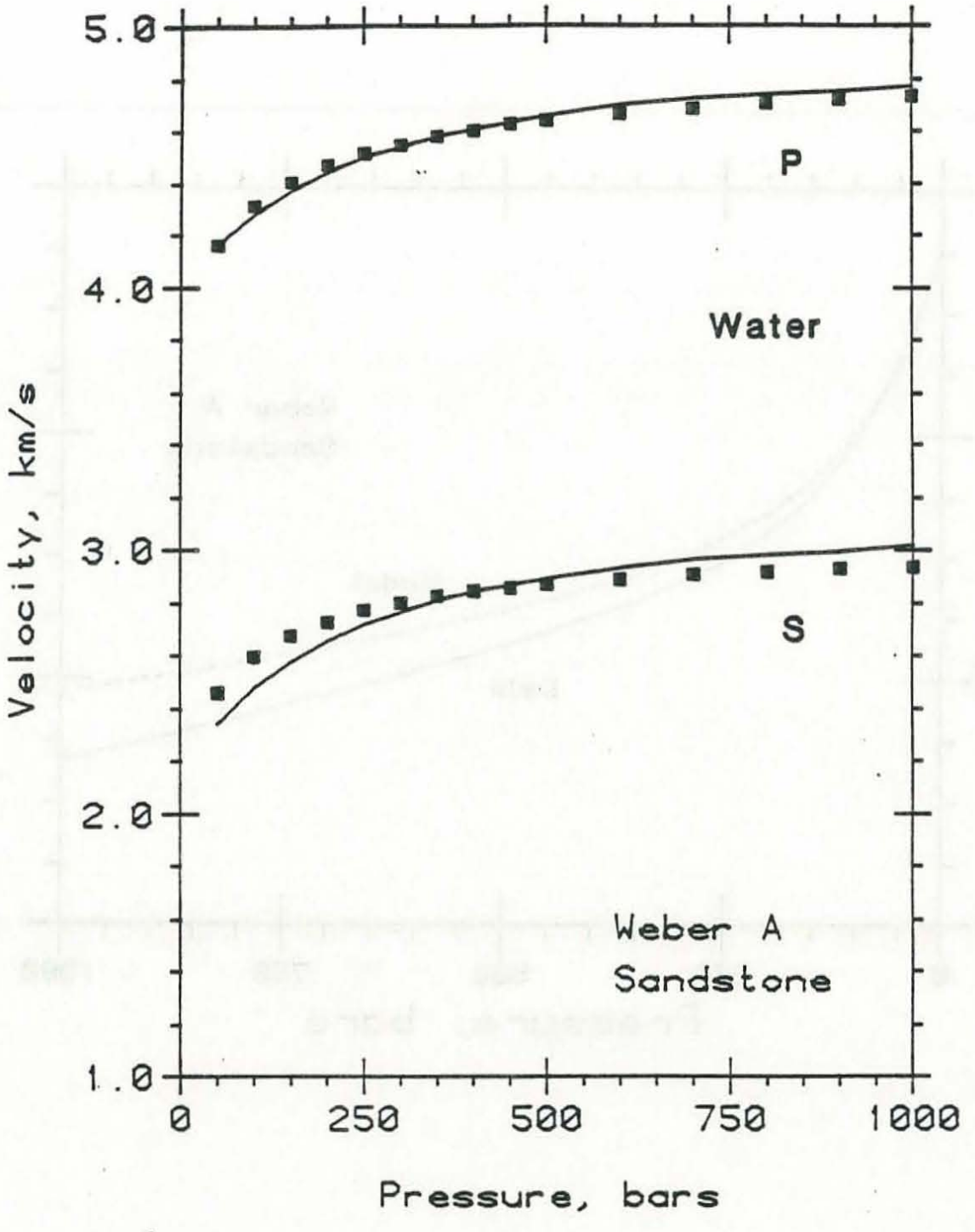

Figure 47. Measured water (solid squares) saturated P- and S-wave velocities for Weber sandstone with predicted water (solid line) saturated velocities from inversion for pore aspect ratio spectra.

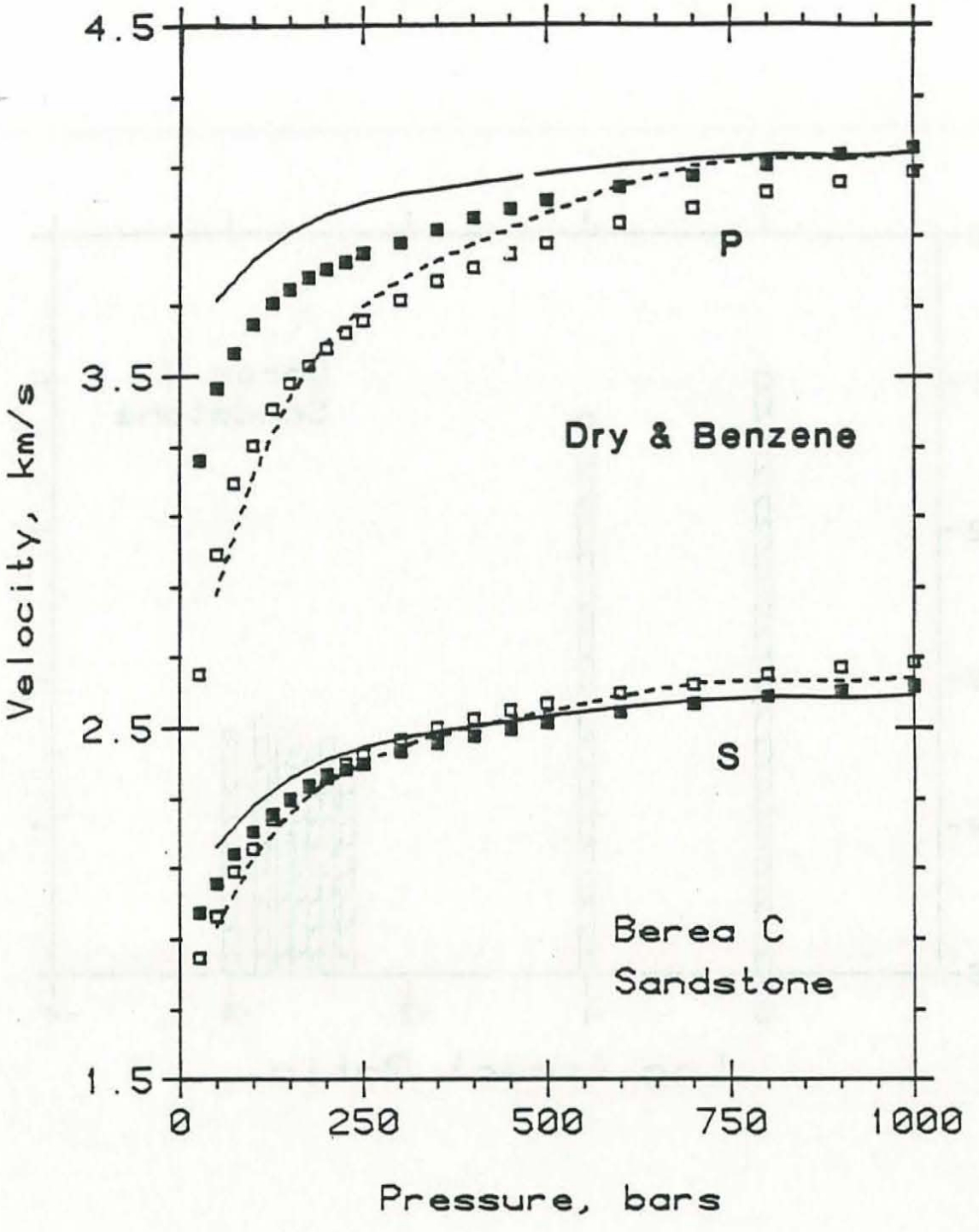

Figure 48. Measured dry (open squares) and benzene (solid squares) saturated P- and S-wave velocities for Berea sandstone with fitted dry (dashed line) and benzene (solid line) saturated velocities from inversion for pore aspect ratio spectra.

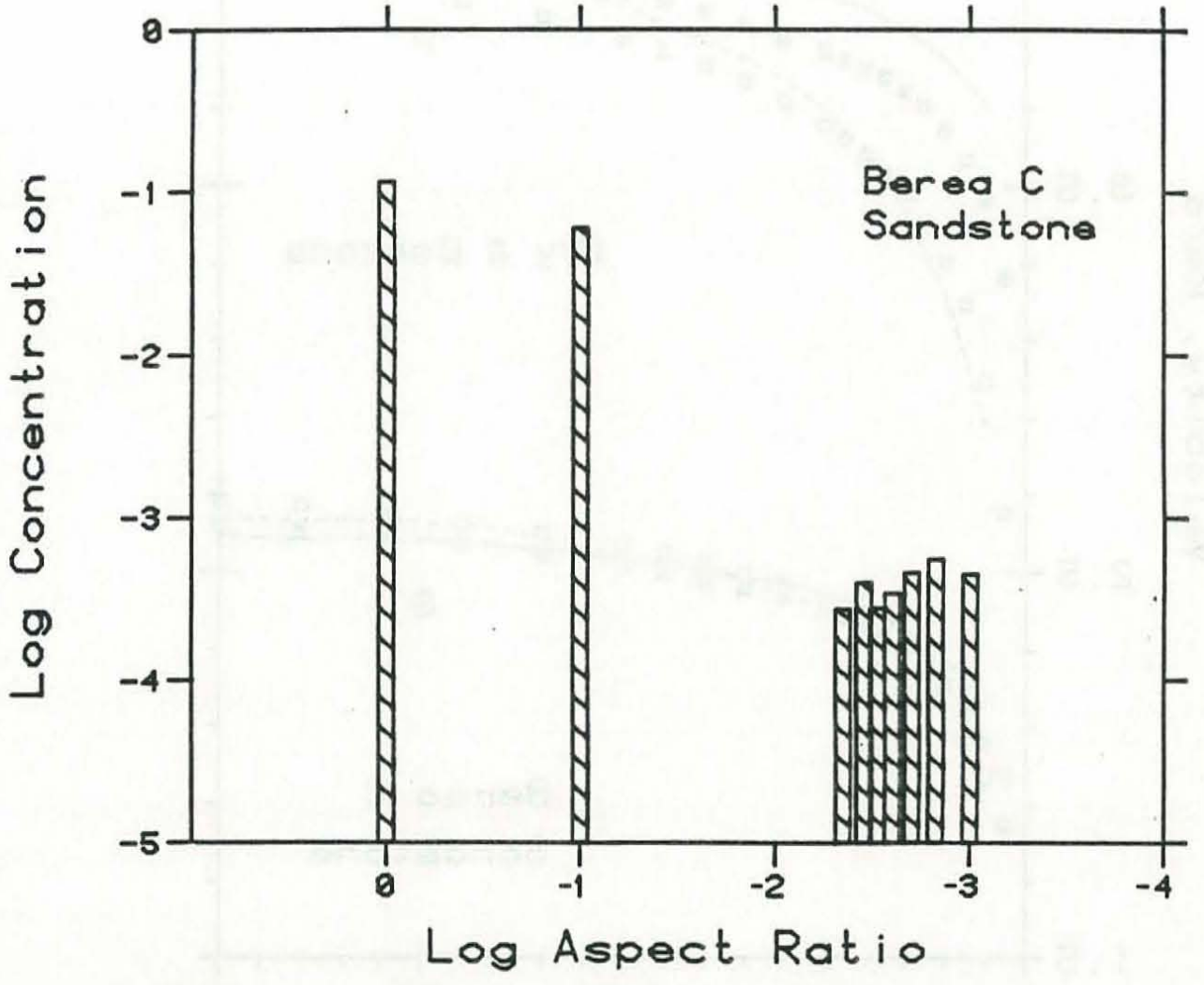

Figure 49. Pore aspect ratio distribution for Berea sandstone at zero pressure based on inversion of dry and benzene saturated velocities.

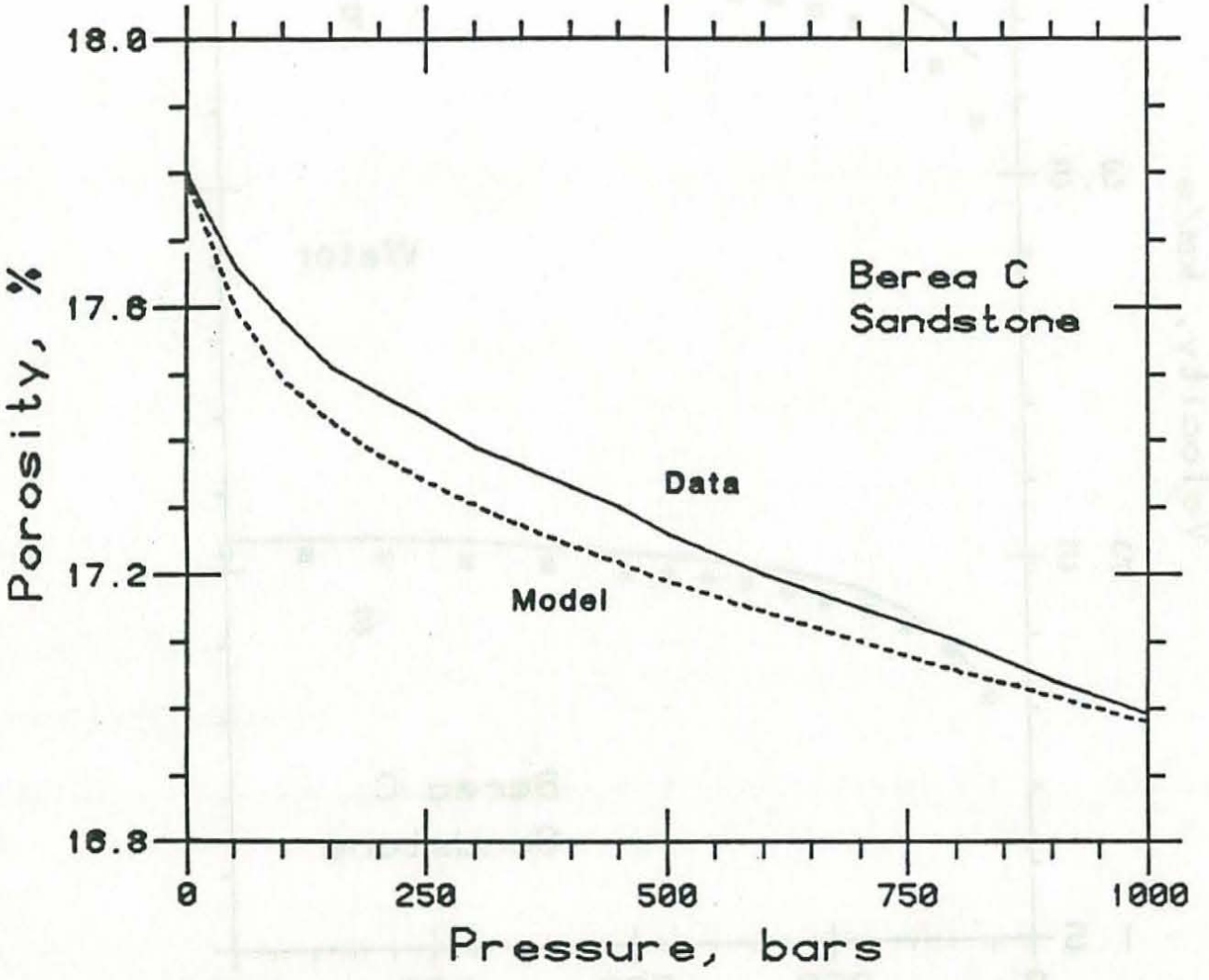

Figure 50. Measured porosity reduction versus confining pressure (solid line) for Berea sandstone compared with that predicted by velocity inversion (dashed line).

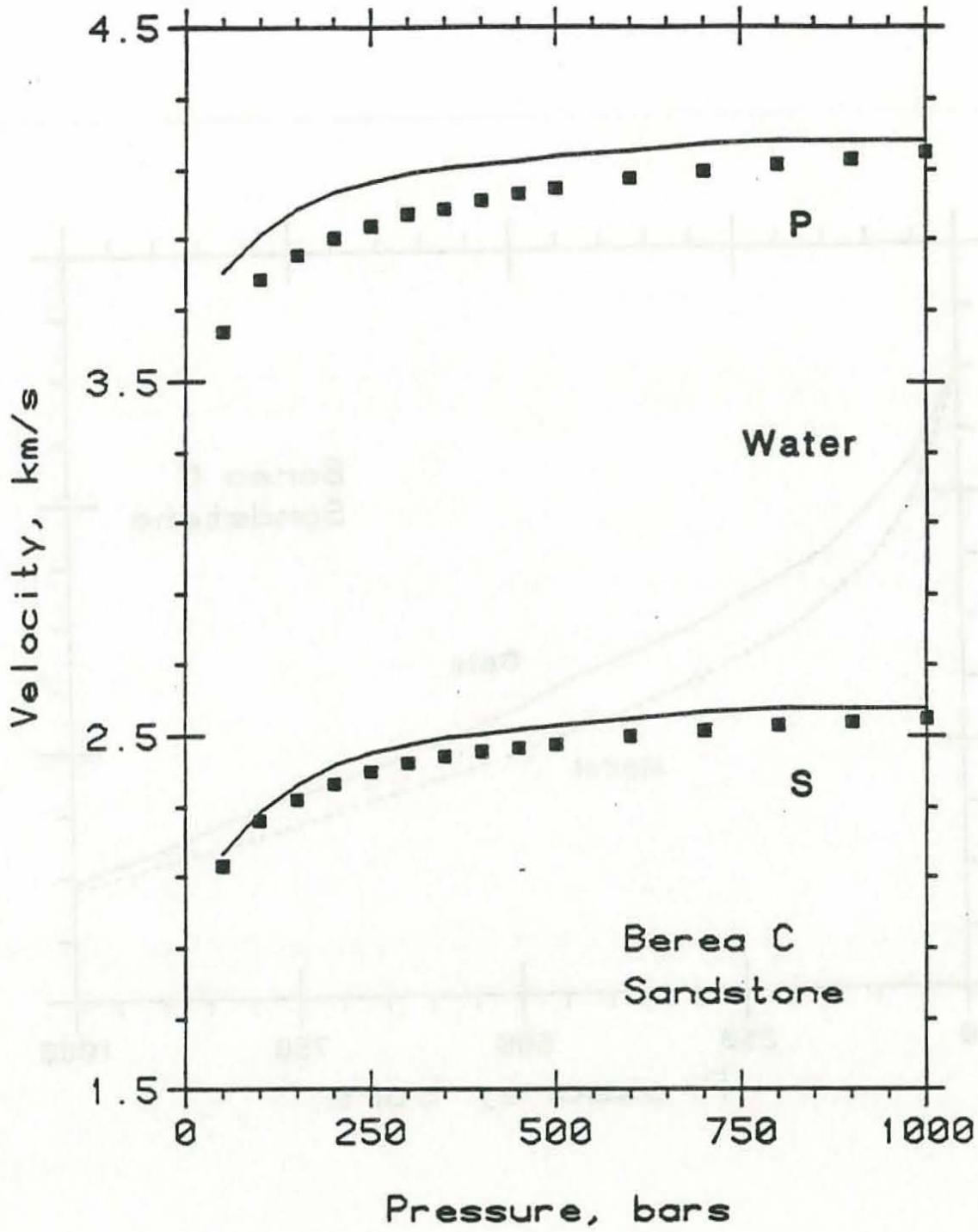

Figure 51. Measured water (solid squares) saturated P- and S-wave velocities for Berea sandstone with predicted water (solid line) saturated velocities from inversion for pore aspect ratio spectra.

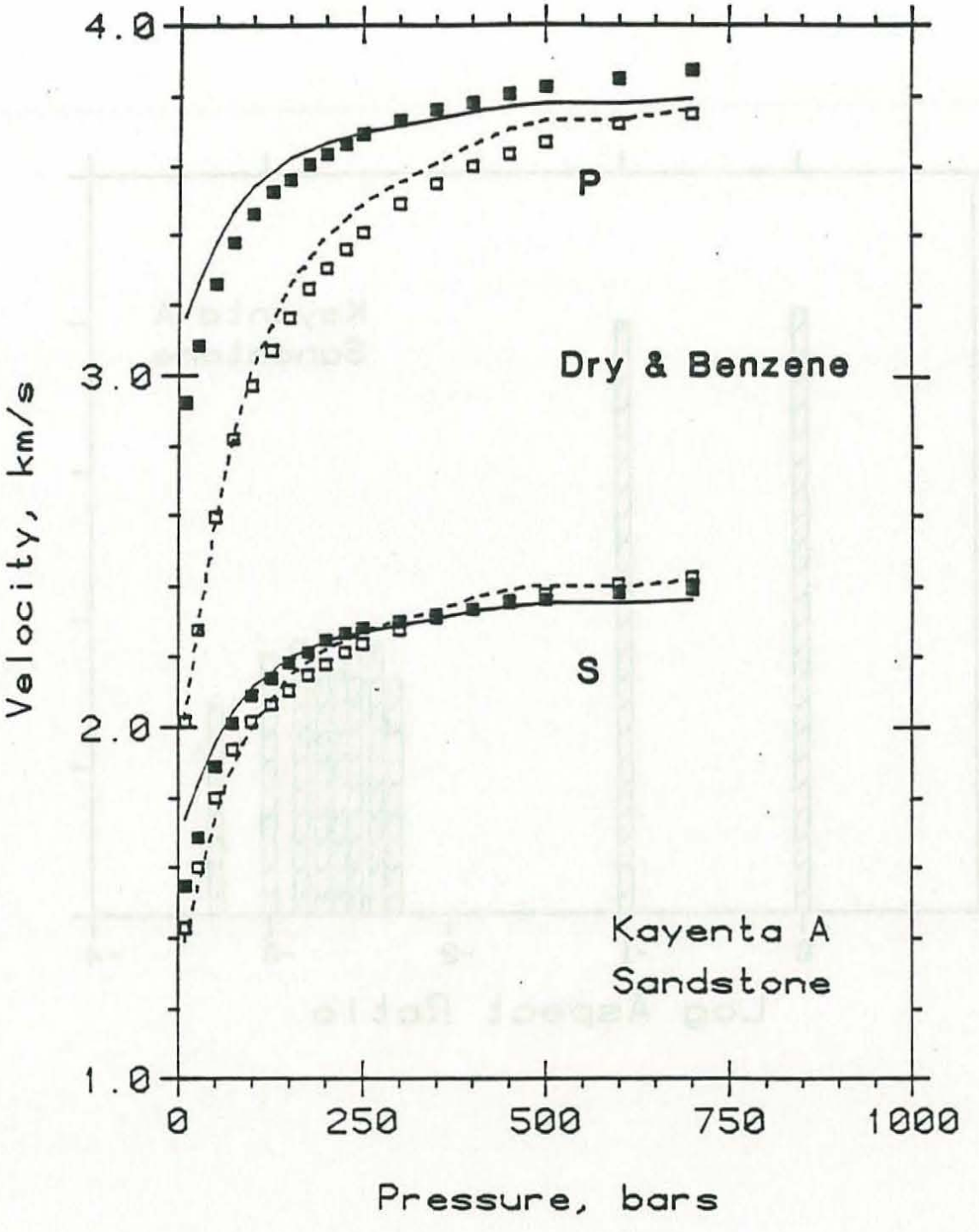

Figure 52. Measured dry (open squares) and benzene (solid squares) saturated P- and S-wave velocities for Kayenta sandstone with fitted dry (dashed line) and benzene (solid line) saturated velocities from inversion for pore aspect ratio spectra.

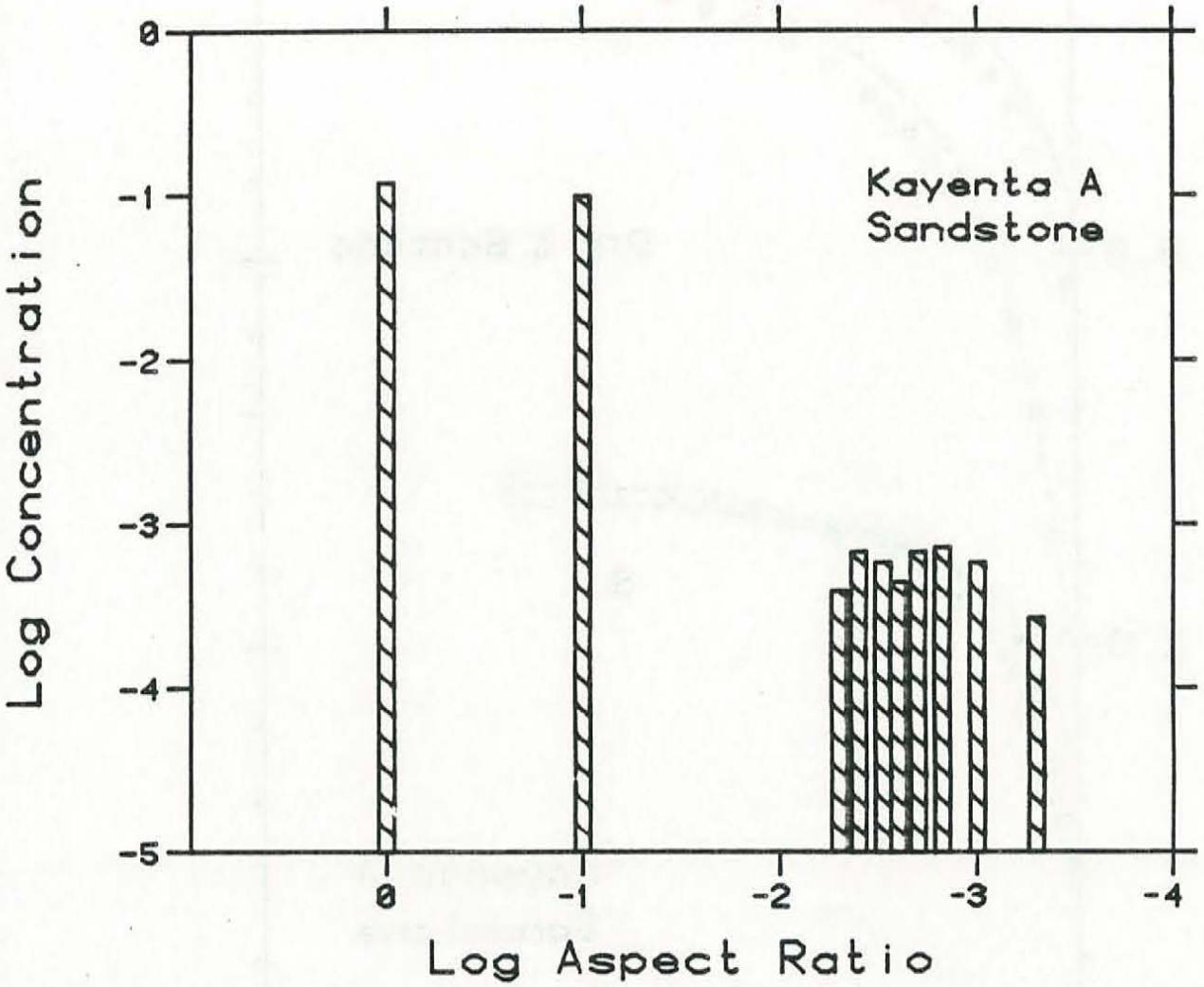

Figure 53. Pore aspect ratio distribution for Kayenta sandstone at zero pressure based on inversion of dry and benzene saturated velocities.

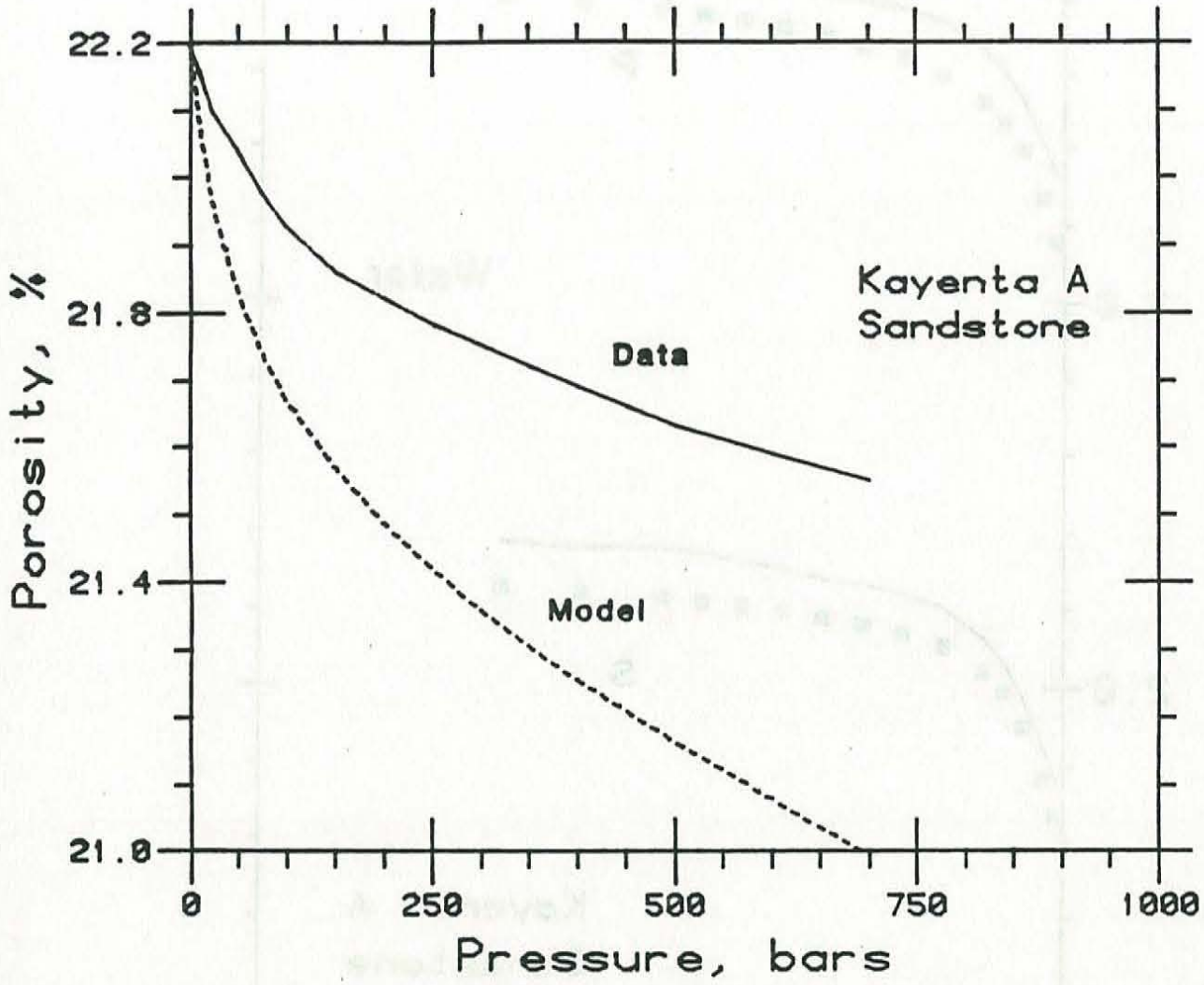

Figure 54. Measured porosity reduction versus confining pressure (solid line) for Kayenta sandstone compared with that predicted by velocity inversion (dashed line).

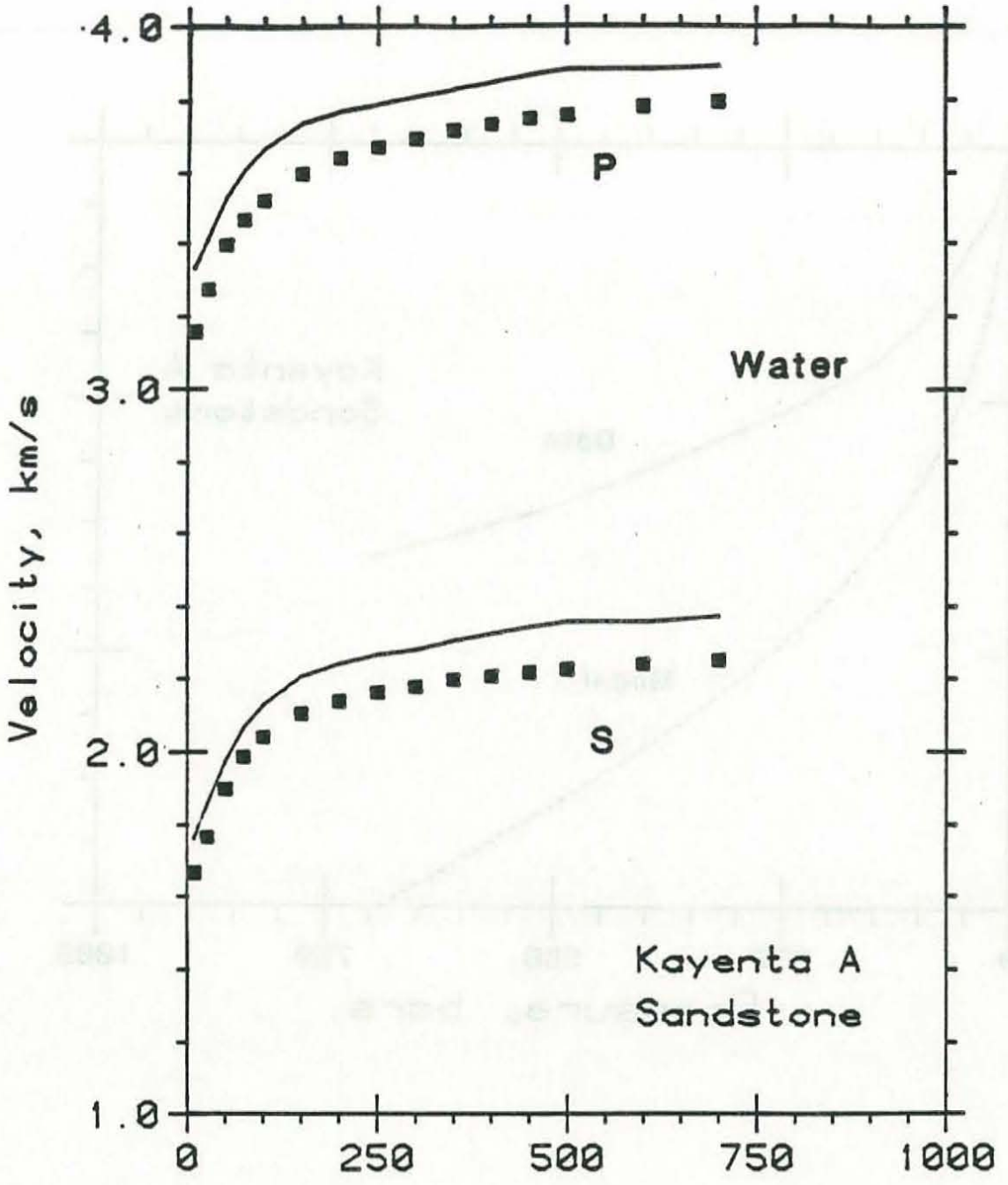

Figure 55. Measured water (solid squares) saturated P- and S-wave velocities for Kayenta sandstone with predicted water (solid line) saturated velocities from inversion for pore aspect ratio spectra.

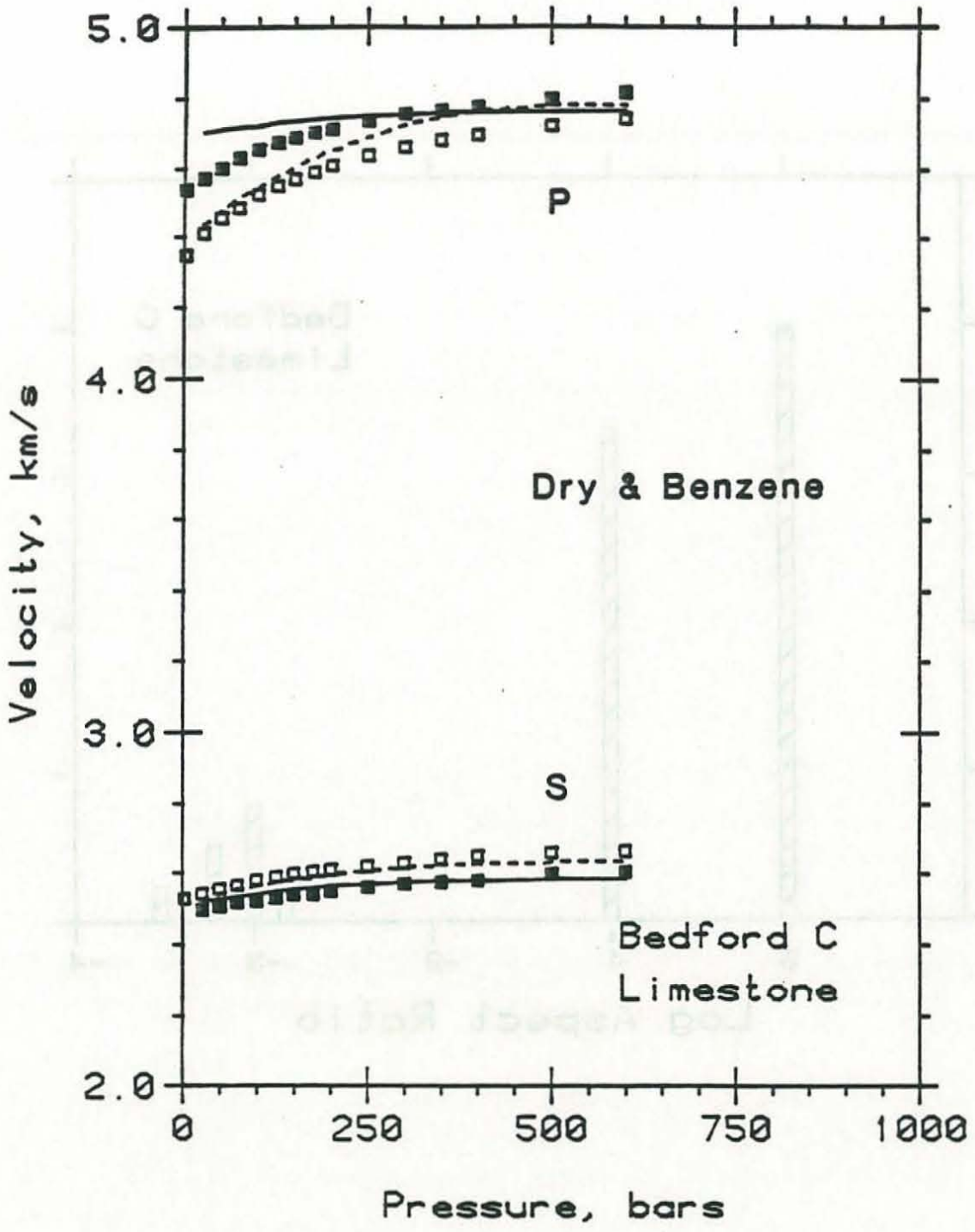

Figure 56. Measured dry (open squares) and benzene (solid squares) saturated P- and S-wave velocities for Bedford limestone with fitted dry (dashed line) and benzene (solid line) saturated velocities from inversion for pore aspect ratio spectra.

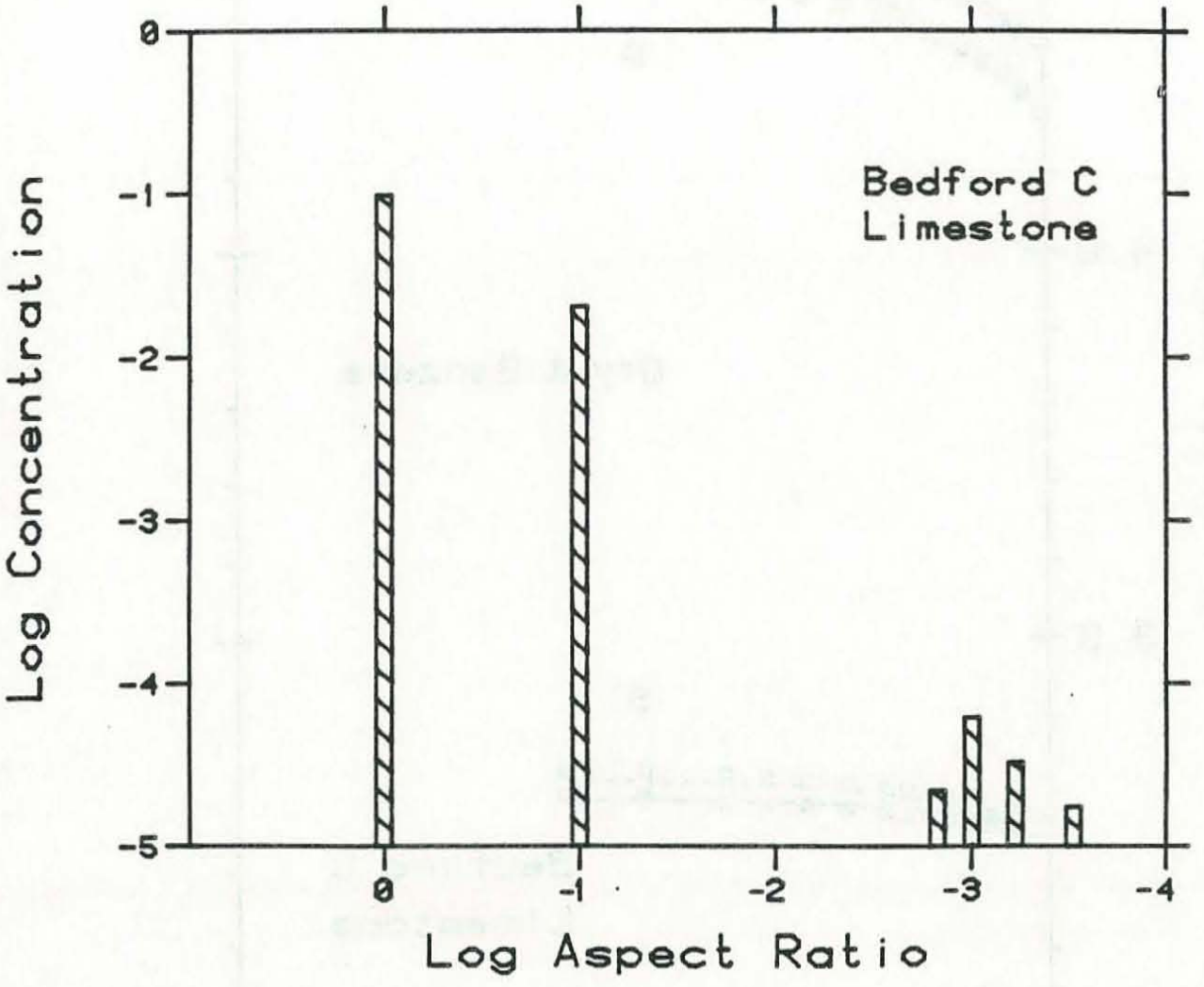

Figure 57. Pore aspect ratio distribution for Bedford limestone at zero pressure based on inversion of dry and benzene saturated velocities.

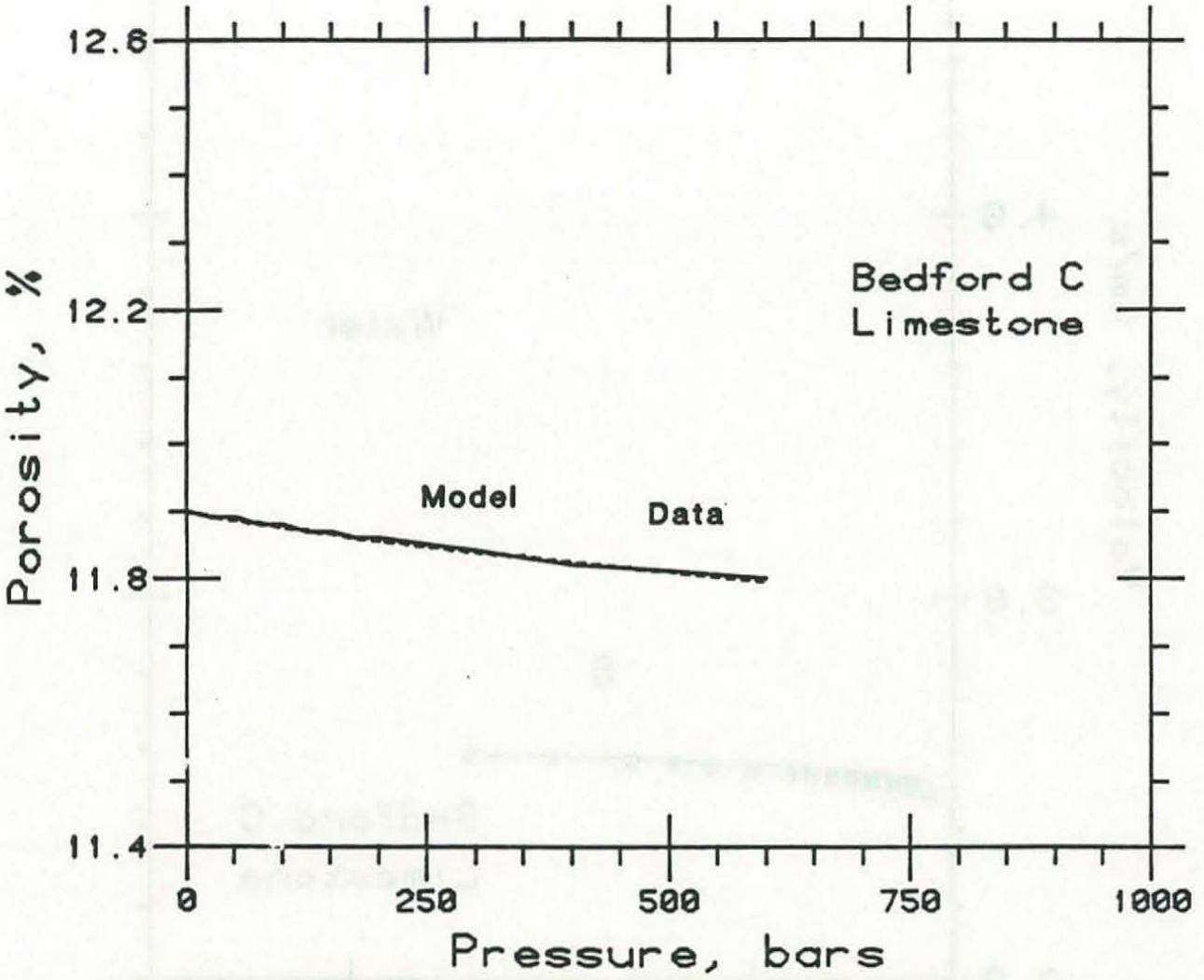

Figure 58. Measured porosity reduction versus confining pressure (solid line) for Bedford limestone compared with that predicted by velocity inversion (dashed line).

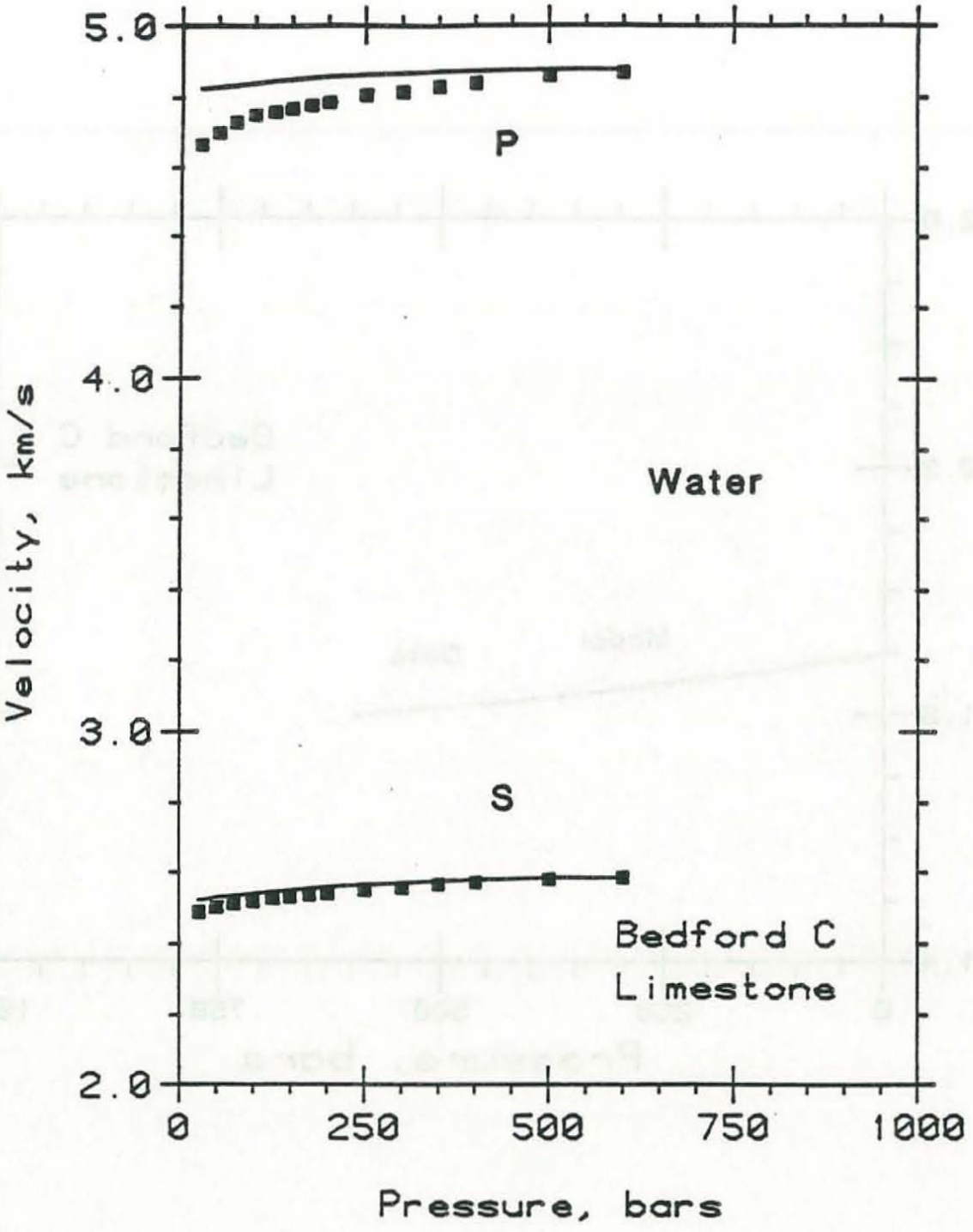

Figure 59. Measured water (solid squares) saturated P- and S-wave velocities for Bedford limestone with predicted water (solid line) saturated velocities from inversion for pore aspect ratio spectra.